5-5-2017

Development of the Tagger Microscope and Analysis of Spin Density Matrix Elements in (Photon, Proton) to (Phi, Proton) for the GlueX Experiment

Alexander E. Barnes
University of Connecticut - Storrs, aeb1723@gmail.com

Development of the Tagger Microscope & Analysis of Spin Density Matrix Elements in γp $\rightarrow$ ϕp for the GlueX Experiment

Alexander Edward Barnes, PhD

University of Connecticut, 2017

The quark model has been successful in classifying the spectrum of mesons observed since the 1960s, however, it fails to explain some of the measured bound states. Lattice QCD predictions have shown that an excited gluonic field may contribute to the quantum numbers of the bound state and form hybrid mesons, $q\bar{q}g$, where g is a constituent gluon. It is possible for some hybrids to possess quantum numbers forbidden by the quark model and are known as "smoking gun" hybrids due to their lack of mixing with conventional $q\bar{q}$ states. The GlueX photoproduction experiment at Jefferson Lab in Newport News, VA is designed to study hybrid mesons and to map their spectrum. A 12 GeV electron beam produces 9 GeV linearly polarized photons via coherent bremsstrahlung in a diamond radiator which are incident on a liquid H_2 target. In order to determine the photon energy, the use of a tagging spectrometer which measures the energy of the post-bremsstrahlung electron is required. The tagger microscope is a scintillating fiber detector designed to measure the energy of electrons corresponding to the polarized photons. The main focus of this work is the design and construction of the tagger microscope electronics as well as the calibration of the microscope within the experiment. Additionally, the analysis of the reaction $\gamma p \rightarrow \phi p$, where $\phi(1020) \rightarrow K^+K^-$, is discussed. This analysis provides a high-level calibration for GlueX in regards to understanding the acceptance and sensitivity of the detectors to mesons with strange quark content. By studying the ϕ with linearly polarized photons, information on the production mechanism can be extracted. The measurement of the ϕ spin-density matrix elements are shown and compared with past data which are found to be in agreement.

Development of the Tagger Microscope & Analysis of Spin Density Matrix Elements in $\gamma p \to \phi p$ for the GlueX Experiment

Alexander Edward Barnes

B.S., Juniata College, 2010

M.S., University of Connecticut, 2013

A Dissertation

Submitted in Partial Fulfillment of the

Requirements for the Degree of

Doctor of Philosophy

at the

University of Connecticut

2017

2017

APPROVAL PAGE

Doctor of Philosophy Dissertation

Development of the Tagger Microscope & Analysis of Spin Density Matrix Elements in $\gamma p \to \phi p$ for the GlueX Experiment

Presented by

Alexander Edward Barnes, B.S., M.S.

Major Advisor _____

Richard Jones

Associate Advisor _____

Alex Kovner

Associate Advisor _____

Peter Schweitzer

University of Connecticut

2017

DEDICATION

I would like to dedicate this dissertation, first and foremost, to my parents, Robert and Joyce. Throughout the years, they have been there to encourage and support me in all of my endeavors.

And to my sisters, Hilary and Elaine, who always lent me their ears and who pushed me to achieve my goals.

And to my girlfriend, Marion, who was there for me whenever I needed her.

And to all my friends who helped me remember that there is life outside of work.

ACKNOWLEDGMENTS

Over the years, there have been many people who helped contribute to this work, and I will attempt to briefly list them here. To those not listed, I greatly appreciate the help you gave me.

I would like to acknowledge my research group, starting with my advisor, Dr. Richard Jones, for providing me with such a wide range of opportunities from which to learn and showing me what the field has to offer. My group mates Fridah Mokaya, Brendan Pratt, Igor Senderovich, and Jim McIntyre helped me with everything from hardware to physics analyses by giving me excellent feedback, advice, encouragement, and many fond memories to look back upon. I would like to thank Ann Marie Carroll for all of her hard work in constructing and testing the tagger microscope. Additionally, I would like to thank all of the undergraduates who helped in the lab, specifically Ben Willis, Liana Hotte, and Jon Kulakofsky, who I worked closely with during the construction of the tagger microscope.

Furthermore, I would like to acknowledge the Jefferson Lab staff who helped me grow as a physicist, particularly Paul Mattione, Justin Stevens, Alexandre Deur, Beni Zihlmann, David Lawrence, Elton Smith, Alex Somov, Tom Carstens, and Tim Whitlatch. These people provided guidance and instruction which allowed me to complete the tagger microscope installation and calibrations as well as my physics analysis. I would also like to acknowledge a few of my fellow GlueX graduate students, Mike Staib, Eric Pooser, and Will McGinley, for their help in learning programming, understanding the GlueX software, and other pragmatic discussions.

TABLE OF CONTENTS

CHAPTER PAGE

LIST OF FIGURES

LIST OF TABLES

CHAPTER 1

Introduction

1.1 Introduction

During the 1950's and 1960's, experiments measured the spectrum of light hadrons, e.g. protons, neutrons, pions, which were considered, at that time, to be elementary particles. As the number of observed particles increased, with more being unstable, the interpretation as elementary particles came into question. In order to provide a way to classify these particles, the Eightfold Way, and soon thereafter, the quark model were developed. It was proposed that these hadrons consisted of smaller, elementary particles called quarks and were formed as $q\bar{q}$ or qqq bound states. Elastic scattering experiments measuring the form-factors of the proton supported the idea of quarks, as the results were inconsistent with a proton being a point-like object. After further experimental investigation, the theory of quantum chromodynamics (QCD) was developed and modeled after the successful theory of quantum electrodynamics (QED).

It was found that at in the high momentum limit, the quarks became asymptotically free, i.e. weak binding, while at low momentum, the quarks are believed to be confined to their bound state. Further tests were unable to isolate the constituents of hadrons. At the high momentum limit, the coupling constant becomes small and theoretical calculations could be performed based on perturbation theory. However, this breaks down for lower momenta which causes a problem in interpreting experimental data with the theory. Models based on QCD were developed in order to understand the data in this limit, and in more recent years, numerical calculations became a viable means of expanding our theoretical understanding. This method involves performing QCD calculations on a discretized Euclidean space-time lattice and is known as lattice QCD.

This document presents experimental work in "light-meson spectroscopy" with the GlueX experiment and describes my contributions with the goal of furthering our understanding

of QCD. The following sections provide the theoretical background and basis of the GlueX experiment which is explained in later chapters.

1.2 Theoretical Framework

1.2.1 Quark Model

The quark model, proposed independently by Murray Gell-Mann and George Zweig, has been successfully used to classify the large number of particles discovered from the 1950s onward. The model was based on the Eightfold Way which uses SU(3) flavor symmetry to group particles into nonets. The particles are considered to be spin-$\frac{1}{2}$ fermions which are now known as quarks. These quarks have fractional electric charge, either $+\frac{2}{3}$ or $-\frac{1}{3}$, and an additional charge called color which comes in three varieties: red, green, and blue.

The bound states of quarks form color-neutral objects which restricts the strong force to the nuclear scale. Possible configurations to generate a color-neutral state include quark-anti-quark pairs, called mesons, and three quark states, called baryons. In the case of mesons, the color charges would be the color and its anti-color, such as (red, anti-red). For baryons, the possible color configurations would require one of each of the colors: red, green, blue.

For $q\bar{q}$ systems, the allowed quantum numbers J^{PC} for a bound state follow a specific set of rules. The quark spins may be aligned parallel ($S = 1$) or anti-parallel ($S = 0$) with relative orbital angular momentum (L). The total angular momentum is then $J = L + S$ with parity defined as $P = (-1)^{L+1}$ and charge conjugation $C = (-1)^{L+S}$. This leads to a pseudoscalar meson nonet (π, K, η) of $J^{PC} = 0^{-+}$ for $S = 0$ and $L = 0$, and a vector meson nonet $(\rho, K^*, \omega, \phi)$ of $J^{PC} = 1^{--}$. The combination of $S = 1$ and $L = 1$ yields three nonets: scalar $J^{PC} = 0^{++}$, axial vector $J^{PC} = 1^{++}$, and tensor $J^{PC} = 2^{++}$. These rules also predict that certain combinations are forbidden, such as $J^{PC} = 0^{--}, 0^{+-}, 1^{-+}, 2^{+-}, \ldots$. Because these states were not observed, credence was given to the quark model.

Within a decade of its development, the quark model was superseded by a fundamental gauge theory of strong interactions called quantum chromodynamics (QCD), which was formed and modeled after the successful theory of quantum electrodynamics (QED). It was proposed by QCD that these quarks and color charges formed fermion currents with exchange quanta called gluons. Unlike the photons of QED, gluons are able to interact with each other and form bound states. The theory also included fermion loops which led to the idea of sea quarks. The quark model can then be considered a constituent quark model that uses the valence quarks to model bound hadron systems. Each valence quark would effectively have a larger mass than the elementary particle mass that appears in the Lagrangian. These quarks have been classified into light (up, down, strange) and heavy (charm, top, and bottom) flavors each with a different mass. Mesons composed of light quarks can be grouped into sets of 9 (nonets) with approximately equal masses based on their J^{PC} quantum numbers. The focus of this document will be on the spectroscopy of these light quarks.

1.2.2 Beyond the Quark Model

One consequence of QCD is that quarks are confined and cannot be isolated in order to have color-neutral objects. This implies a force much different than QED. Instead of a force that diminishes as the distance between objects increase, the strong force is constant with distance (Fig. 1.1). In the limit of small distances, the quarks can be considered to be asymptotically free and perturbative calculations can be made for theoretical predictions. However, in the limit of larger distances, the quarks are strongly confined with a coupling constant near unity. This prevents perturbative methods from being successful, and theoretical predictions must rely on either lattice QCD or first-principles QCD.

In addition, the quark model does not include the gluons and, therefore, does not explain quark confinement. If the gluons are included in predicting possible states, one would expect bound states such as ggg, and $q\bar{q}g$, where g represents a gluon. These states are categorized as exotics and are called glueballs and hybrids, respectively, where hybrids are the combination

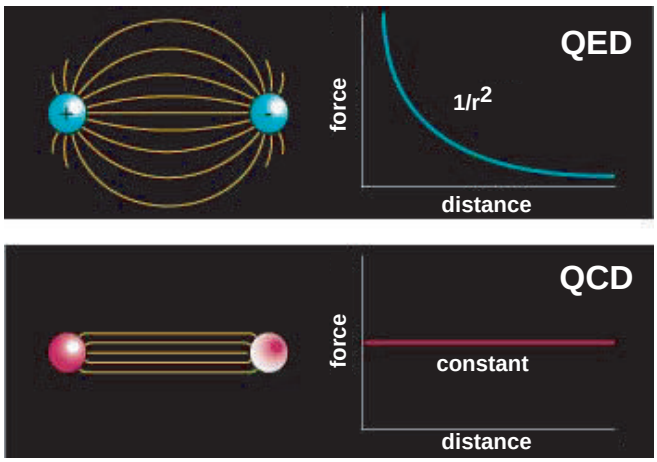

Figure 1.1: (top) The field lines between two electric charges and the corresponding dependence of force on distance between them and (bottom) the field lines between two quarks and the corresponding dependence of force on the distance between them.

of conventional $q\bar{q}$ states with constituent gluons. Additionally, exotics also include states with higher numbers of valence quarks, such as tetraquarks ($qqqq$) and pentaquarks ($qqqqq$). The bound state of a hybrid can be modeled as a flux-tube where the field lines of the gluons create a tube along the axis between the quarks.

Lattice QCD supports this idea of a flux tube between $q\bar{q}$ (Fig. 1.2). The idea was first proposed by Yoichiro Nambu in the 1970's to explain the observed linear Regge trajectories, the linear dependence on m^2 of hadrons on their spin, J. If one assumes massless quarks that are connected by a relativistic string with constant mass (energy) per length with the system rotating about the center, a linear dependence arises. Conventional mesons are formed when the flux tube is in the ground state, and excited states would occur when the flux tube is in a vibrationally excited state. The flux tube would rotate clockwise or counter-clockwise about the string axis to form a pair of degenerate flux tube excitations since the energy should not depend on the direction of rotation. Lattice and flux tube models indicate that the lowest excitation has $J = 1$. Within the flux tube model, this is a linear combination of the clockwise and counter-clockwise states which are eigenstates of parity and charge conjugation and leads to two possible excited flux tubes: $J^{PC} = 1^{-+}$ or $J^{PC} = 1^{+-}$.

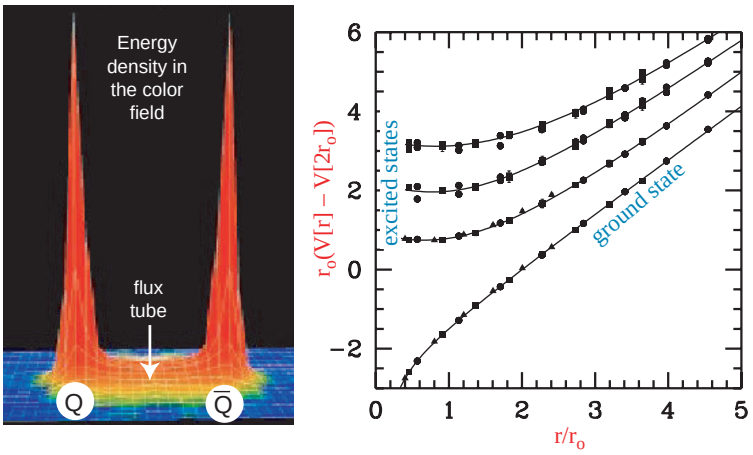

Figure 1.2: (left) A lattice QCD representation of the energy density in the color field between a quark and anti-quark. The density is peaked at the position of the quarks and is confined to a tube between the quarks. This calculation is for heavy quarks in the quenched approximation. (right) The corresponding potential between the quarks where the ground state has a $1/r$ dependence at small distances and is linear for large distances. The excited potential curves are the result when the flux tube is in a vibrationally excited state.

If the $q\bar{q}$ state is $S = 0$, $L = 0$ (or $J^{PC} = 0^{-+}$, a pseudoscalar like π or K), a combination with a $L = 1$ flux tube excitation results in hybrid mesons with either $J^{PC} = 1^{++}$ or $J^{PC} = 1^{--}$, both of which are allowed in the quark model. If $S = 1$, $L = 0$ ($J^{PC} = 1^{--}$, like the vector photon) then the hybrid could have $J^{PC} = [0, 1, 2,]^{+-}$ if the tube has $J^{PC} = 1^{-+}$, or $J^{PC} = [0, 1, 2]^{-+}$ for a tube with $J^{PC} = 1^{+-}$. Out of 6 possibilities, 3 are forbidden by the quark model. These forbidden states will not mix with regular $q\bar{q}$ and will provide a unique "smoking gun" signature for states with gluonic excitations.

1.2.3 Experimental Hints

Since the formulation of the quark model and QCD, there have been hints of gluonic excitations in multiple experiments. One such example comes from the Crystal Barrel experiment at CERN which studied $p\bar{p}$ annihilations. There was evidence of the $f_0(1500)$ which is a leading candidate for a glueball [1] [2]. However, there is no "smoking gun" signature for the 0^{++} glueball, and there are indications that this state is mixed with conventional $q\bar{q}$ states [3]. More broadly, it may be concluded that one or more glueballs have been ob-

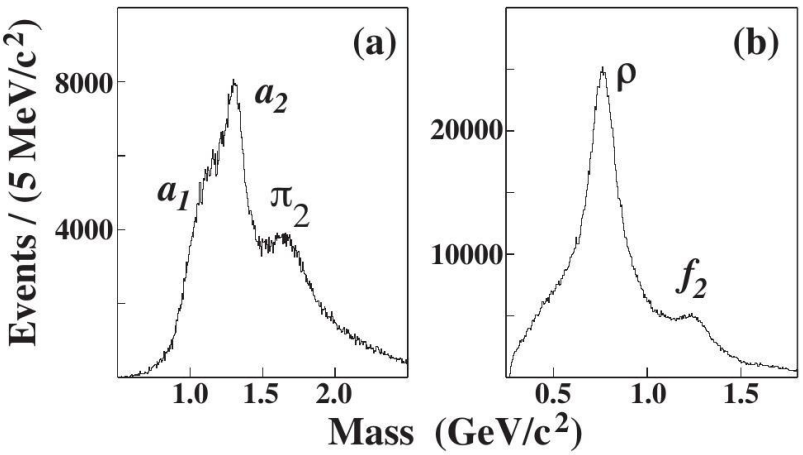

Figure 1.3: Acceptance corrected mass distributions for (a) $\pi^+\pi^-\pi^-$ and (b) $\pi^+\pi^-$ from E852 at Brookhaven.

served, since there are more observed states than can be accounted for in the $q\bar{q}$ model. It is difficult to identify these glueballs states due to their mixing with $q\bar{q}$ in the mass range 1.5 to 2.5 GeV/c^2. The lightest glueball with "smoking gun" quantum numbers is expected to have $J^{PC} = 2^{+-}$ and a mass of 4 GeV/c^2 [4].

Experiment E852 at Brookhaven reported observations of exotic $J^{PC} = 1^{-+}$ states in $\pi^- p$ interactions at 18 GeV/c. One of the states has a mass of $(1593 \pm 8^{+29}_{-47})$ MeV/c^2 and width of $(168 \pm 20^{+150}_{-12})$ MeV/c^2 and decays into $\rho^0\pi^-$ [5]. It was observed in $\pi^- p \to \pi^+\pi^-\pi^- p$ at a beam momentum of 18 GeV/c and the mass distributions of $\pi^+\pi^-\pi^-$ and $\pi^+\pi^-$ can be seen in Fig. 1.3. A partial wave analysis (PWA) was performed on the data and assumed an *isobar* model in which a parent decayed into a $\pi\pi$ state with an unpaired π followed by the decay of the $\pi\pi$ state. Fig. 1.4 shows the decomposition into the various waves. This shows the $\pi(1800)$ in the 0^{-+} wave, the $a_1(1260)$ in the 1^{++} wave, the $\pi_2(1670)$ in the 2^{-+} wave, and the $a_2(1320)$ in the 2^{++} wave. Fig. 1.5 shows evidence for the exotic $\rho\pi$, where if an isovector $\rho\pi$ resonates in an $L = 1$ wave, it would have $J^{PC} = 1^{-+}$. This figure also shows the effect of wave leakage from the non-exotic partial waves. A coupled fit to the wave intensities and phase difference between the 1^{-+} and 2^{-+} waves are shown in Fig. 1.6 which the authors use to argue that the 1^{-+} wave goes through a resonance at 1.6 GeV/c^2.

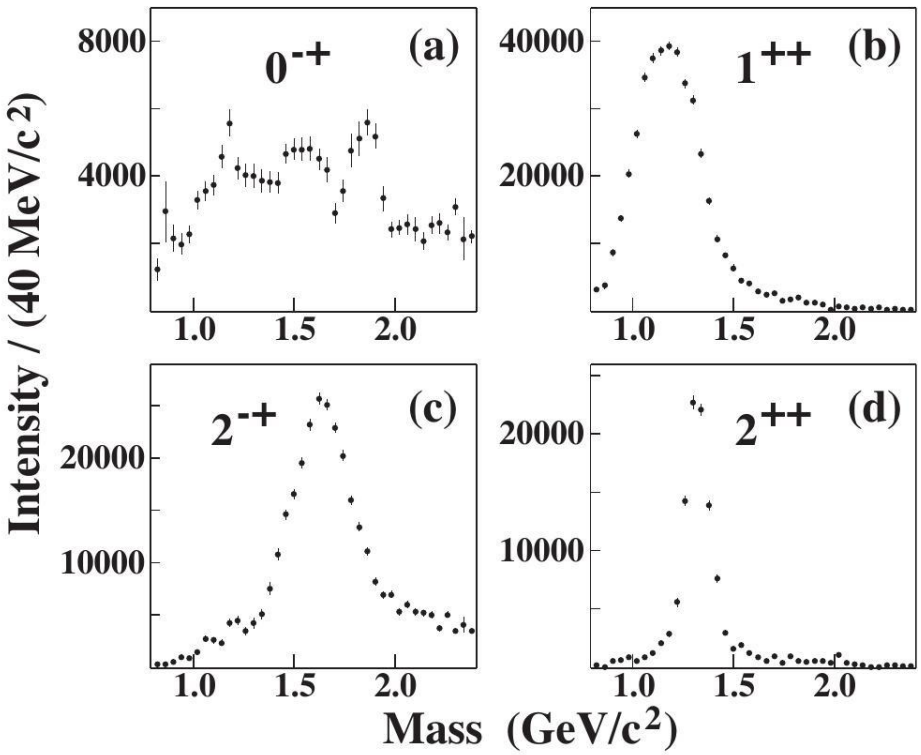

Figure 1.4: E852 intensities for PWA waves (a) 0^{-+}, (b) 1^{++}, (c) 2^{-++} and (d) 2^{++}.

Exotic states have been reported in other experiments as well. The GAMS collaboration claimed an exotic meson decaying into $\eta\pi^0$ [6] but a later analysis by the group [7] led to ambiguous results. Both VES and KEK showed evidence of exotics in $\eta\pi$ [8] [9] but leakage from the dominant D wave (non-exotic) could not be excluded.

1.2.4 Photoproduction

As mentioned above, exotic "smoking gun" quantum numbers provide an unambiguous signal for hybrid mesons. An effective way to produce such states is through the use of a photon, as compared to π or K, as a probe. In the case of a photon, it is a virtual $q\bar{q}$ with aligned spins (S = 1), whereas with π or K, the meson is a $q\bar{q}$ with anti-aligned spins (S = 0). For both, the relative orbital angular momentum is zero (L = 0) and the flux tube is in its ground state. Figure 1.7 displays the difference between a γ and π probe. If the scattering results

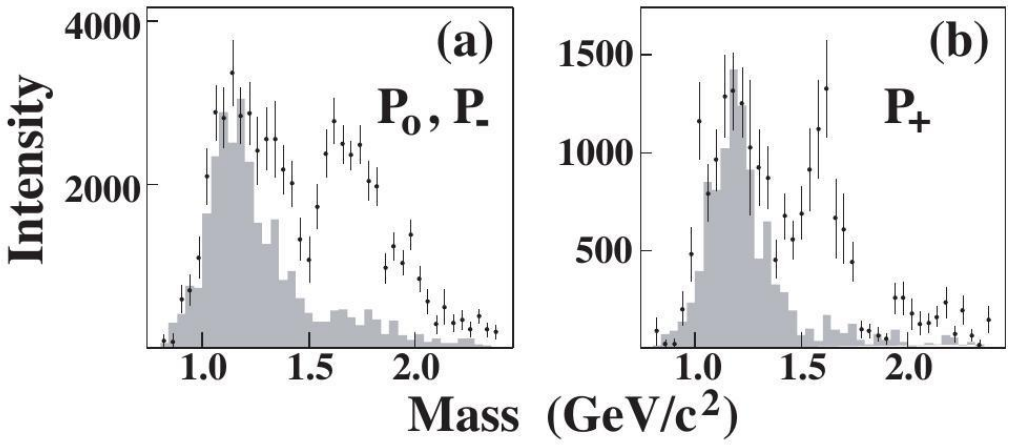

Figure 1.5: E852 intensities for exotic waves 1^{-+} in $\rho\pi$. The shaded distributions are estimates of leakage from non-exotic waves.

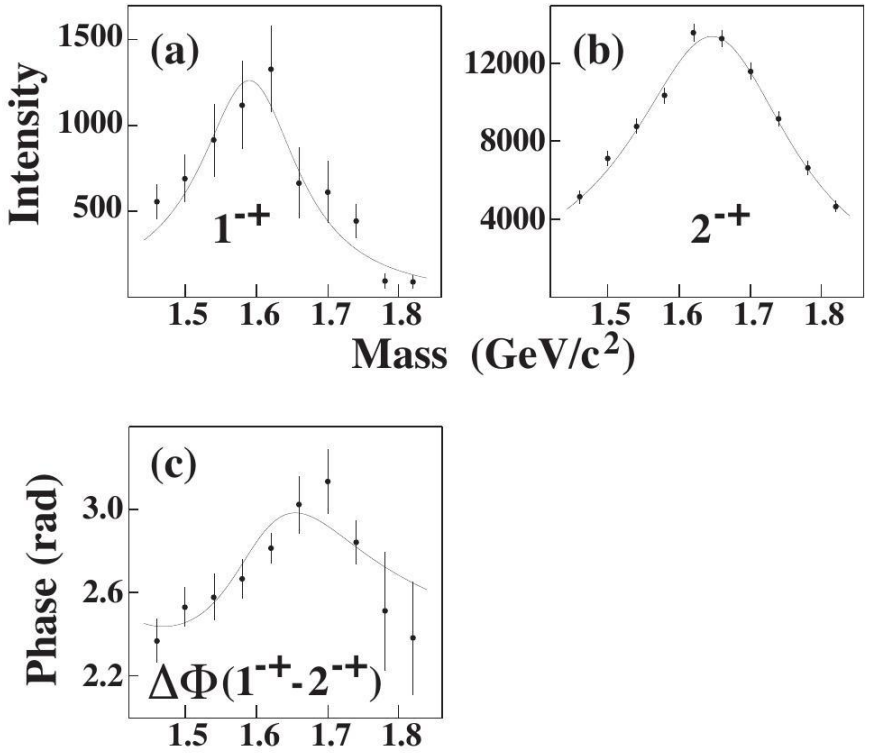

Figure 1.6: E852 coupled mass-dependent Breit-Wigner fit of (a) 1^{-+} and (b) 2^{-+} waves as well as the (c) phase difference.

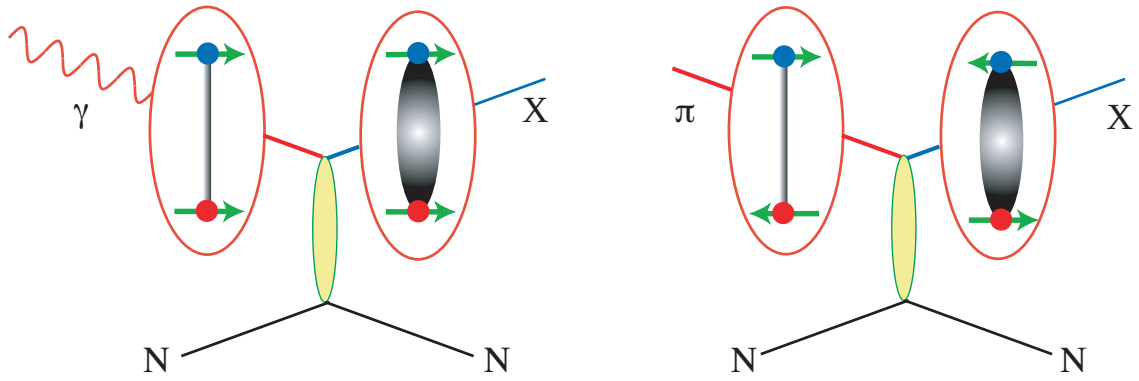

Figure 1.7: (left) The incoming quarks have $L = 0$ and $S = 1$. When the flux tube is excited, exotic hybrid mesons are possible. (right) The incoming quarks have $L = 0$ and $S = 0$. The resulting excited flux tube has non-exotic quantum numbers.

in an excited flux tube, it is expected that "smoking gun" hybrid mesons will be suppressed in π produced interactions and enhanced in photoproduction [10].

1.2.5 Polarization

Polarization is very important when looking for exotics as the states of linear polarization are eigenstates of parity. When using partial wave analysis (PWA) to search for exotics, initial states with good parity will maximize the information that can be obtained from the decay angular distributions. In particular, linear polarization is useful in providing information on decays in lieu of statistics. It is also critical in isolating production mechanisms and can be used as an exotics filter if the production mechanism is known.

For example, consider the photoproduction of ρ into $\pi\pi$, where the ρ has the same helicity as the incident photon. The $\pi\pi$ wave function, in the ρ rest frame, is

$$Y_1^m(\theta, \phi) \propto sin\theta \cdot e^{im\phi} \tag{1.1}$$

The square of this amplitude, for circularly polarized photons (either $m = 1$ or $m = -1$), carries no ϕ information while plane-polarized photons have a $\cos^2\phi$ dependence and out-of-plane a $\sin^2\phi$ dependence.

The usefulness of linear polarization in determining the production mechanism can be seen by looking at an example. Consider a produced vector particle ($J^P = 1^-$) from the exchange of a scalar ($J^P = 0^+$ for natural parity exchange) or a pseudoscalar ($J^P = 0^-$ for unnatural parity exchange). In the center of mass frame of the vector particle, the momentum vectors of the photon and exchange particle are collinear. In the case of circularly polarized photons, the m of the vector is the same as that of the photon. Parity conservation requires $L = 0, 2$ for natural parity exchange and $L = 1$ for unnatural parity exchange. With $m = +1$, the total amplitude is $A_N + A_U$, and $A_N - A_U$ for $m = -1$. However, linearly polarized photons allow fo the extraction of A_N for photons polarized in the x-direction, and A_U for photons polarized in the y-direction.

Similarly, linear polarization can be used to filter out exotics supposing one can determine the naturality of the exchange particle by selecting data within a range of $|t|$. Depending on the desired naturality, selection of in-plane or out-of-plane polarization will select the naturality of the produced particle and filter out the exotic wave.

1.2.6 Experimental Requirements

From the above arguments, an experiment whose purpose is to observe exotic mesons should make use of a photon beam with linear polarization. The GlueX experiment has been developed in this way and will be explained in the following chapter.

CHAPTER 2

The GlueX Experiment

2.1 GlueX Overview

A new photoproduction experiment, called GlueX, at the Thomas Jefferson Laboratory in Newport News, Virginia has been constructed. The goal of GlueX is to map the spectrum of mesons with exotic quantum numbers in order to have a quantitative understanding of confinement in quantum chromodynamics (QCD) [11]. The Continuous Electron Beam Accelerator Facility (CEBAF) accelerator, as seen in Fig. 2.1, has been upgraded from a 6 GeV to a 12 GeV continuous wave electron beam which provides the existing experimental Halls A, B, and C with a maximum beam energy of 11 GeV and delivers 12 GeV electrons to Hall D which houses the GlueX experiment.

In Hall D, the 12 GeV electrons are incident on a 20 μm thin diamond wafer where they undergo coherent bremsstrahlung and produce linearly polarized photons. The paths of the electrons are curved by a dipole magnet and steered into one of two tagging detector arrays which will be discussed in more detail in later sections. Electrons which do not lose a significant fraction of their energy in passing through the radiator are directed into a beam dump. The photons travel 75 m downstream to a 3.4 mm diameter hole, called the collimator, with most of the intensity within m/E radians of the incident electron direction, where m is the rest mass of the electron and E is the energy of the coherent bremsstrahlung electron. This cut on the emission angle is useful because coherent and incoherent photons have different angular distributions. Coherent photons have maximum energy at $\theta = 0^\circ$ with energy decreasing as the angle increases. It is this relationship that causes the sharp edges in the coherent spectrum. Incoherent bremsstrahlung photons essentially do not have an energy-angle correlation and thus collimating photons beyond some angle $\theta_{max} < m/E$ attenuates the incoherent spectrum at all energies. This increases the fraction of linearly polarized photons hitting the target. Once through the collimator, the photon beam is

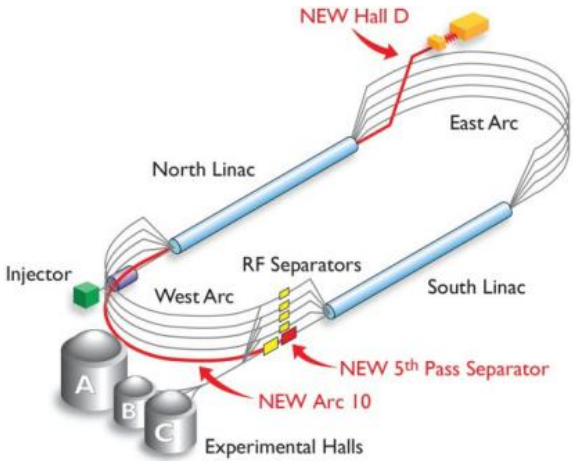

Figure 2.1: CEBAF overview. Red labels indicate the 12 GeV upgrades.

incident on a liquid hydrogen target inside of a solenoid magnet. The GlueX detector (Fig 2.2 and 2.3) is designed for high-statistics spectroscopy and has nearly 4π coverage to allow for partial wave analysis (PWA). The particles created by the collision will be measured by various detectors which will be explained in this chapter.

The first commissioning run took place in the fall of 2014 and the first physics run in the spring of 2017. GlueX has been approved by the Jefferson Lab Program Advisory Committee (PAC) for 200 days of physics running at an average intensity of 5 x 10^7 γ/s on target. This data set will exceed the current photoproduction data collected by all former experiments in this energy region by several orders of magnitude [12].

2.2 Photon Beamline

The 12 GeV electron beam from CEBAF can provide $(0.005 - 5.0\ \mu A)$ for Hall D, with the low current used in special flux measurements and higher currents in standard running. An illustration of the Hall D beamline can be seen in Fig. 2.4. A photon beam is produced via coherent bremsstrahlung when the electron beam is incident on a diamond crystal. The energy range of the produced photons that are tagged in the photon tagger is from $3.0 \leq E_\gamma \leq 11.8$ GeV. The diamond radiator was oriented to produce a peak in the coherent

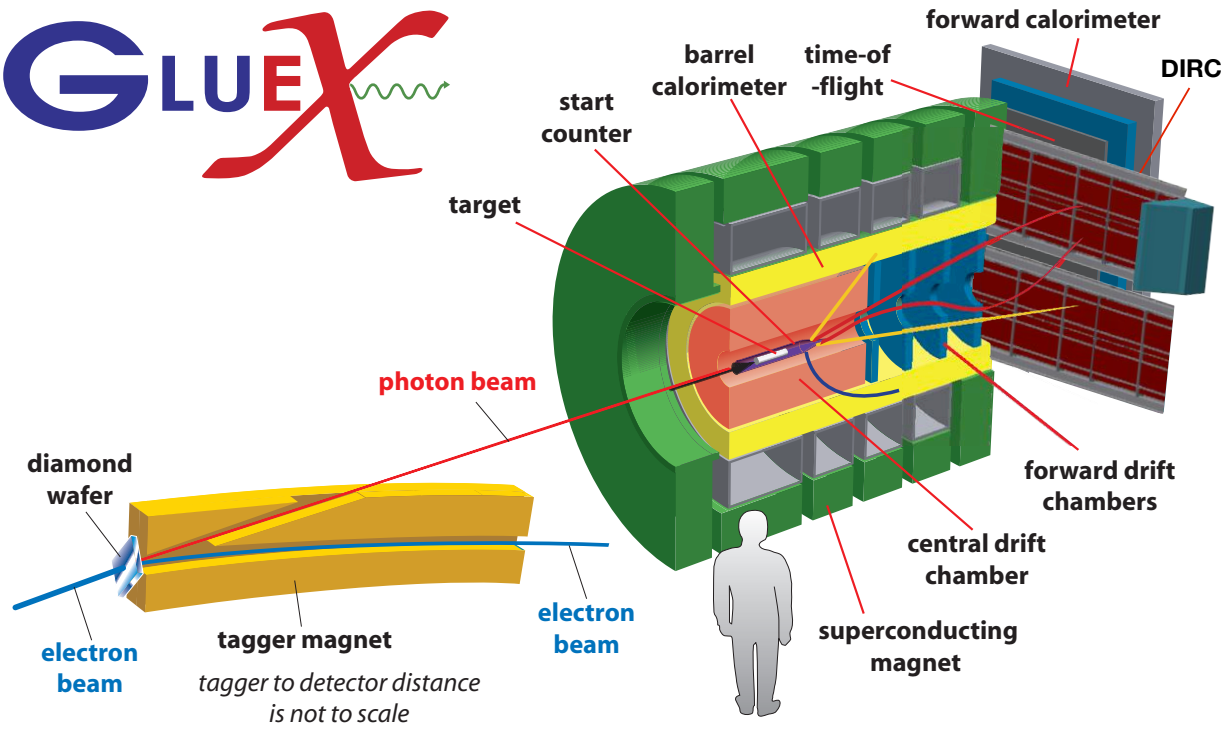

Figure 2.2: A cut-away view of the GlueX experiment and beamline.

bremsstrahlung spectrum in the energy range $8.4 \leq E_{coherent} \leq 9.0$ GeV with a peak linear polarization of 40%. The photon energy (Fig. 2.5) is not measured directly but rather inferred through the measurement of the momentum of the post-bremsstrahlung electrons. This is called "tagging" and is performed by the tagging spectrometer.

2.2.1 Diamond Radiator

The polarized photon beam is produced through bremsstrahlung off an electron in a mono-crystalline diamond radiator. An ordered crystal lattice recoils coherently from the incident electron when oriented correctly in a process called coherent bremsstrahlung. This produces an enhancement in the photon spectrum at specific energies corresponding to the reciprocal lattice vectors of the crystal and can be seen in Fig 2.5. The secondary peaks in the energy spectrum are due to integral multiples of the fundamental reciprocal lattice vector and are always present. In addition to the coherent photon spectrum, there is always an incoherent

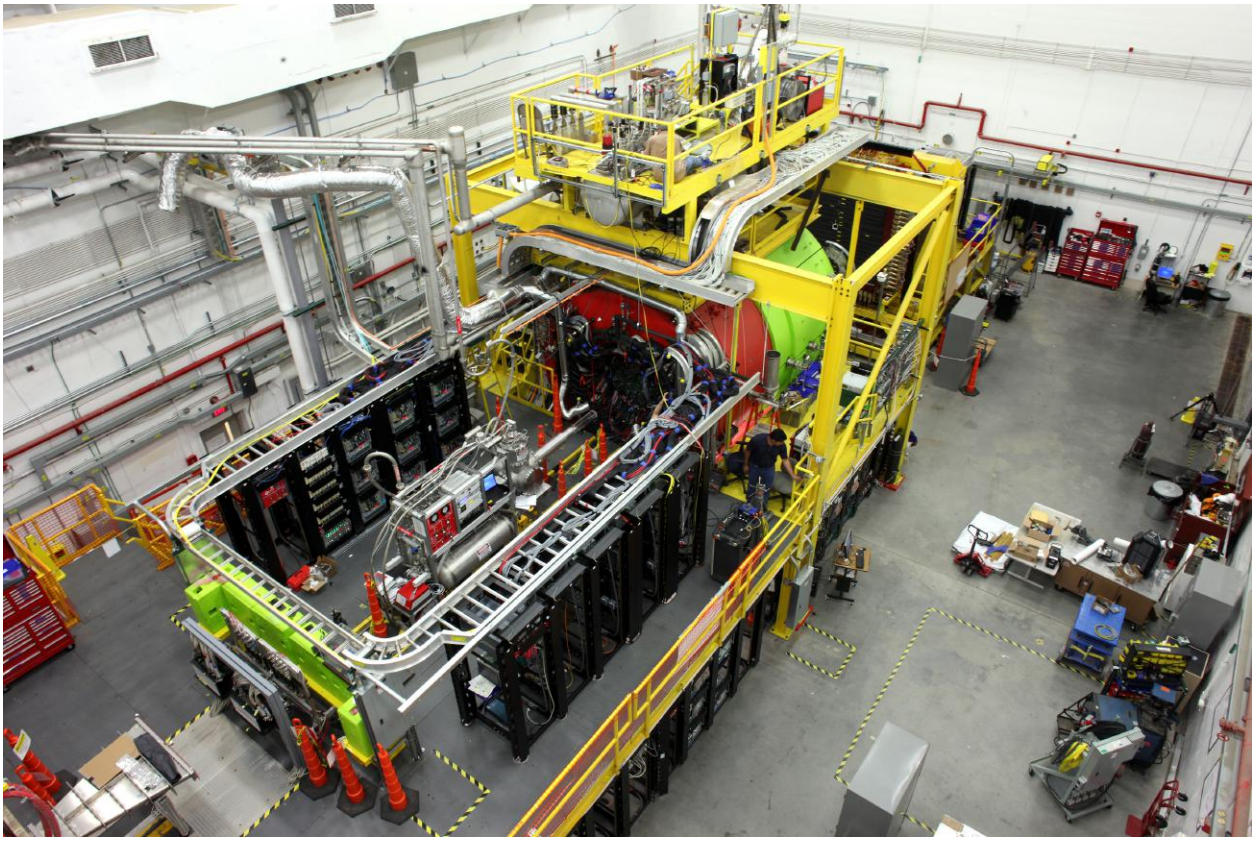

Figure 2.3: The GlueX spectrometer in Hall D

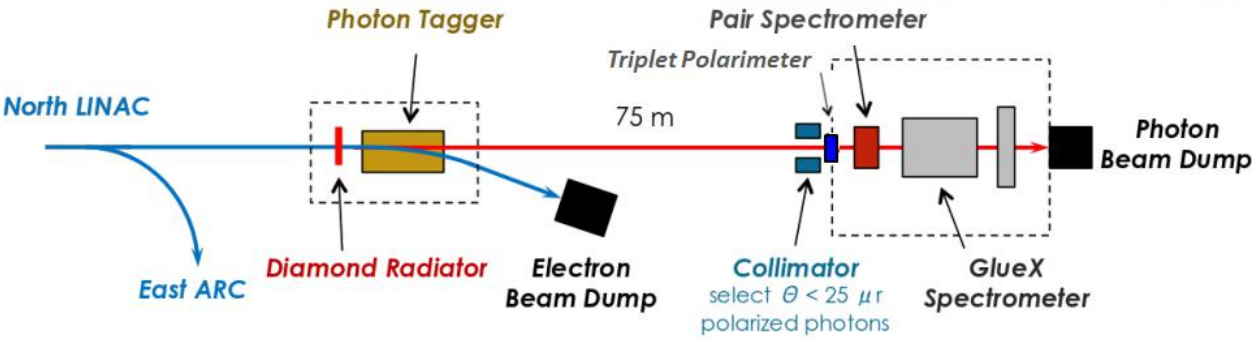

Figure 2.4: Overhead view of GlueX

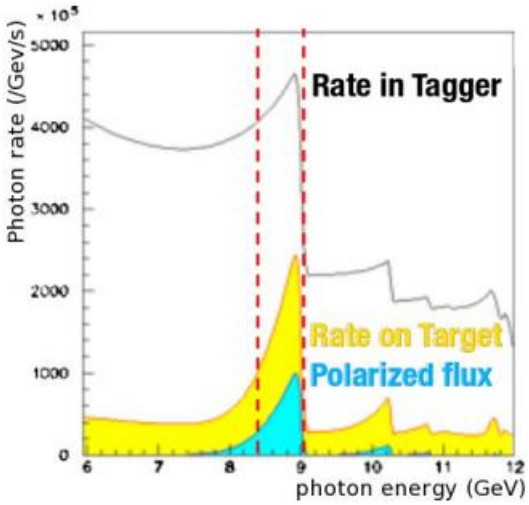

Figure 2.5: Photon rates and energy spectrum from simulation. The black curve shows the photon rate seen by the tagger, the yellow curve by the target, and the teal curve the polarized flux seen by the target.

background which follows the typical $1/E$ distribution. The peaks due to the coherent part can be seen as enhancements above the incoherent background.

The location of the coherent peak is tuned by rotating the lattice planes of the crystal. To do this experimentally, the diamond is mounted on a goniometer, which can freely adjust the orientation of the radiator. The direction of linear polarization can also be changed through crystal rotations. During initial GlueX running, the polarization directions were chosen to be parallel and perpendicular to the experimental floor. The coherent peak can, in principal, be brought to the end point energy; however, at the limit of total energy transfer from the electron, the momentum transfer vector is in the same direction as the incident electron. The scattering plane is then no longer well-defined and the photon becomes unpolarized. This creates a trade-off between photon energy and polarization. GlueX has decided that a photon of 9 GeV with 40% polarization is the best compromise.

The enhancement and degree of polarization of the coherent bremsstrahlung spectrum is directly related to the quality of the radiator. An ideal diamond radiator would have crystal planes that were completely parallel to one another and would create an extremely well-defined coherent enhancement with a maximum degree of linear polarization. Multiple

scattering of the electron through the planes of the crystal limit a radiator to a thickness of approximately 20 μm. Aside from multiple scattering, crystal lattice deformations caused by foreign atomic species, nitrogen vacancies, and mechanical stresses imparted to the crystal during the thinning process negatively affect the photon beam quality. Transmission mode X-ray diffraction was used to quantify the quality of diamond radiators before they were installed in the GlueX electron beam. GlueX requires the diamond to have a whole-crystal rocking curve of 20 μr r.m.s., where the rocking curve is a plot of Bragg-scattering intensity *vs* angle between incident X-ray beam and the normal to the crystal planes. It is required that the diamond have a rocking curve width at the same order as the divergence of the electron beam at the radiator. However, such a thin diamond is likely to warp and distort in shape thus increasing the rocking curve of the crystal. To prevent this, a laser ablation technique can be used to mill out an inner window where the active area is thick while a frame, which lies outside the reaches of the electron beam envelope, remains much thicker for support and stiffness.

Initial studies of UV laser ablation as a possible technique for producing thin large-area diamond films were carried out by a group at Brookhaven [13]. This capability was duplicated and further developed at UConn by fellow lab mate, Brendan Pratt. It involves using a high-power UV laser to mill diamond. A laser with a wavelength above the band gap of diamond (213 nm) deposits all of its energy within the first few nanometers of the diamond surface. This material responds by ejecting a hot plasma of carbon normal to the diamond surface, leaving an elliptical crate on the order of 200 nm deep. The diamond is rastered across the focal spot of the laser, differentially removing material in geometries set by the user.

The initial diamonds are purchased as 7.2 mm x 7.2 mm x 0.25 mm slabs before being thinned down. Using an excimer laser with an operating wavelength of 193 nm, the inner window of 5 mm x 5 mm is ablated. For comparison, an alternate, industrial approach was

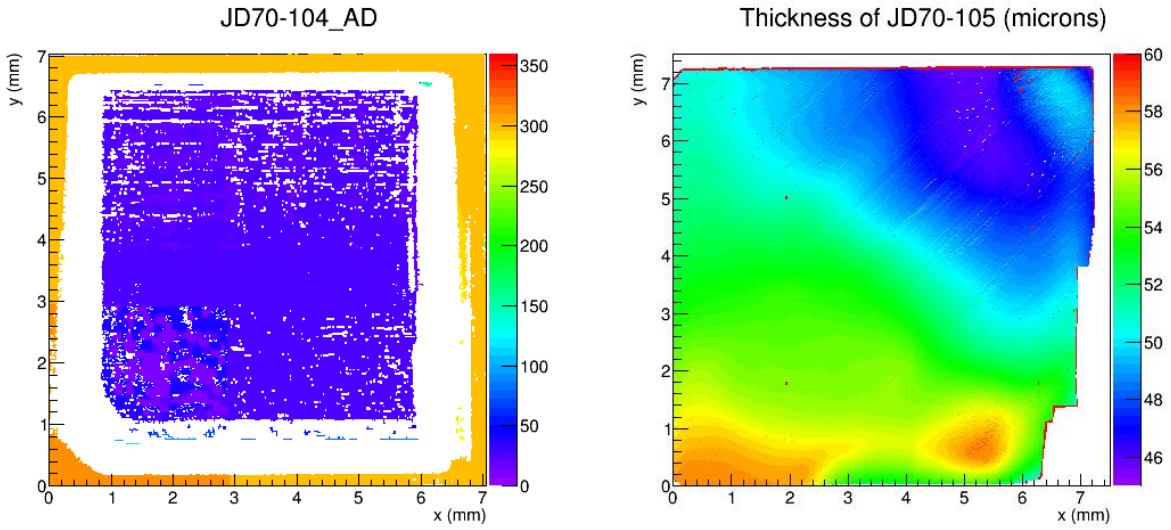

Figure 2.6: Thinned diamonds for GlueX. (left) A Zygo image of a laser ablated diamond. The inner region has a thickness of about 20 μm with a frame thickness of 300 μm. (right) A Zygo image of an uniformly, industrially thinned diamond of about 50 μm thickness. The breakage along the right edge occurred during the final stages of polishing.

used to uniformly thin the entire diamond using an etching technique followed by standard polishing. These can be seen in Fig. 2.6.

The thinned diamonds were taken to Cornell's CHESS (Cornell High Energy Synchrotron Source) facility for X-ray measurements. X-ray diffraction techniques were used to measure the quality of a radiator's crystal planes and the planarity of the crystal. A monochromatic 15 keV X-ray source was incident on the radiator which was held between two sheets of mylar (to prevent mounting stress) and rotated in θ until the Bragg condition was met over the entire area of the crystal. A rocking curve measurement was then taken by stepping in θ (3.5 μr step size) over a range so that the maximum Bragg peak was at the middle of the scan. After each step, a CCD camera recorded the intensity of the Bragg reflection. Each pixel was fit to a Gaussian distribution and the mean and sigma of these fits were mapped to a 2D-histogram, showing the strain and deformation on the physical location of the sample. The whole-crystal rocking curve is the sum of every pixel's intensity as a function of Bragg angle. This histogram was then fit to a Gaussian distribution and the sigma was taken as the whole-crystal rocking curve width for that diamond, which serves as one figure of merit

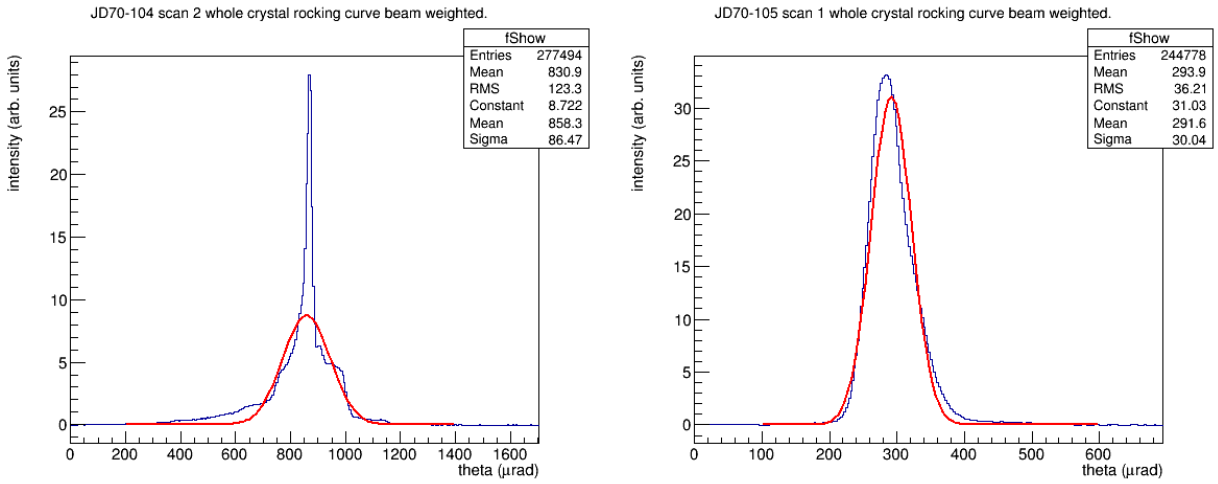

Figure 2.7: (left) Rocking curve measurement of JD70-104, 20 μm diamond. The narrow spike in the middle comes from the central region of the diamond, where the diamond meets the specifications for GlueX. (right) Rocking curve measurement of JD70-105, 50 μm thick. This has a more uniform rocking curve but has a wider spread and is not ideal for GlueX.

for the crystal. Example results can be seen in Fig. 2.7. The UConn group has produced multiple thinned diamonds with one meeting the thickness, area, and rocking curve FWHM specifications along one axis.

While not directly responsible for the diamonds, I contributed to the diamond work conducted at UConn. Most of my help was at CHESS where I mounted, oriented, and measured the diamond crystals. I also assisted with the installation of the diamonds in the GlueX goniometer.

2.2.2 Tagging Spectrometer

The paths of the post-bremsstrahlung electrons are bent by a dipole magnet via the Lorentz force. Any electrons which radiated a high-energy photon are steered into the tagging spectrometer, otherwise they go into the beam dump. The magnetic field separates the electrons based on their momentum which determines their radii of curvature. The tagging detector arrays are placed with the counters along the focal plane of the magnet, and by equating each tagging counter with an energy, photons can be *tagged* through energy conservation.

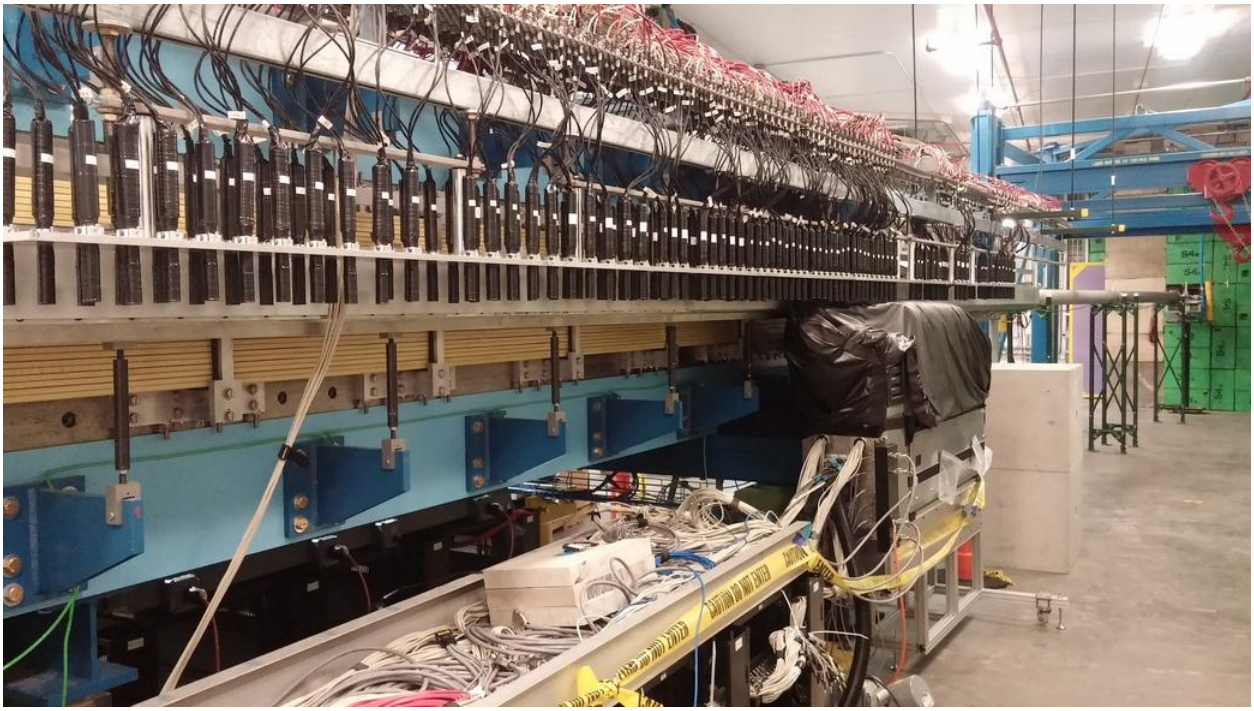

Figure 2.8: The post-bremsstrahlung electrons travel through the dipole tagger magnet (in blue) and are directed into the tagging detector arrays. The TAGM is located in the coherent peak region (near the center of the picture) and is covered by a black shroud. The TAGH is a fixed set of photomultiplier tubes and surrounds the TAGM to measure the incoherent electrons.

There are two tagging detector arrays: the tagger microscope (TAGM) and tagger hodoscope (TAGH). The TAGM is placed in the coherent peak region and is movable so that it can be re-positioned if the coherent peak is changed. The TAGH is a fixed array with removable counters to accommodate the microscope and detects the photons outside of the coherent peak region. The layout of the tagging spectrometer can be seen in Fig. 2.8.

The TAGM consists of 102 columns of 5 scintillating fibers which are 2 cm long and have an area of 2 x 2 mm^2 (Fig. 2.9). These are fused to 1 m light guides which carry the scintillation signal to 510 silicon photomultipliers (SiPMs), also known as multi-pixel photon counters (MPPCs), which are read out by custom electronics boards. The TAGM is placed in the focal plane of the post-bremsstrahlung electrons in the energy range of the coherent peak. When an electron hits a fiber, photons are created via the scintillation process. Some of these photons travel down the length of the light guides and are detected by the SiPMs.

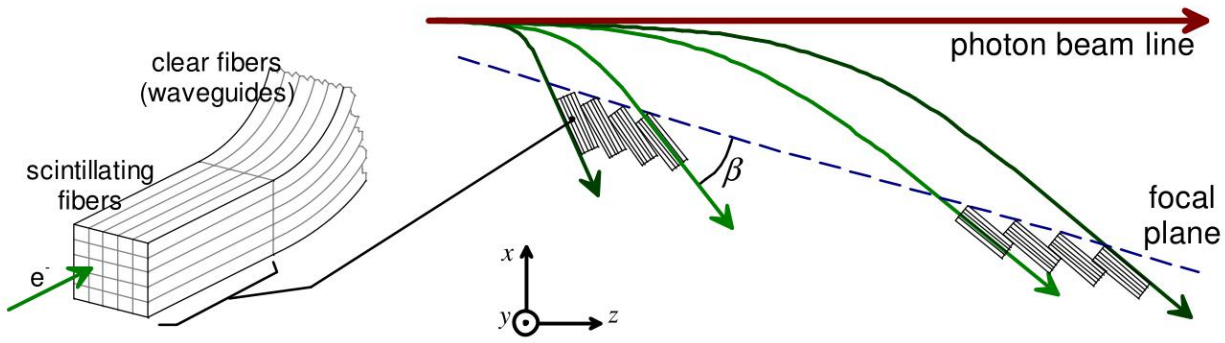

Figure 2.9: The conceptual design of the TAGM. (left) A close view of a fiber bundle showing an electron entering normal to the scintillator surface and carrying the signal through to clear fiber light guides. (right) An overhead schematic of the electron path. The green electron paths are bent by the tagger magnet towards the TAGM where higher energy electrons are on the right. In order to have the electron path normal to the scintillator surface, an angle β is used to adjust the alignment of each mounted fiber bundle.

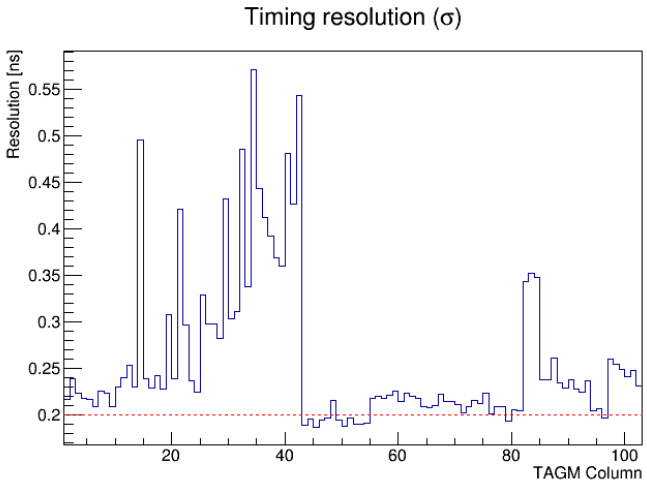

Figure 2.10: The tagger microscope timing resolution during the spring 2017 run. Columns 1-42 correspond to the original set of fibers which have a noticeable loss of resolution due to low photon yield. The red dashed line indicates the design resolution which requires the TAGM to be able to resolve beam bunches that occur every 4 ns.

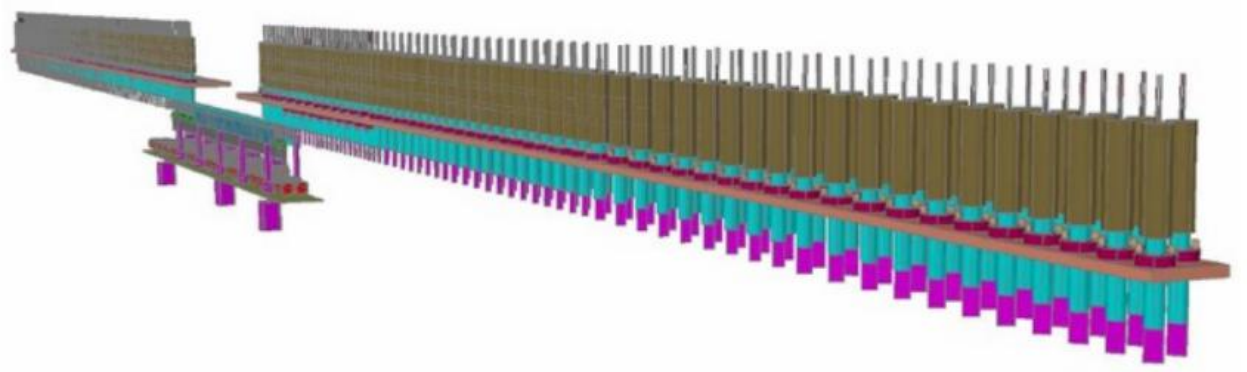

Figure 2.11: A CAD drawing of the tagger hodoscope with a gap in the middle to leave room for the microscope.

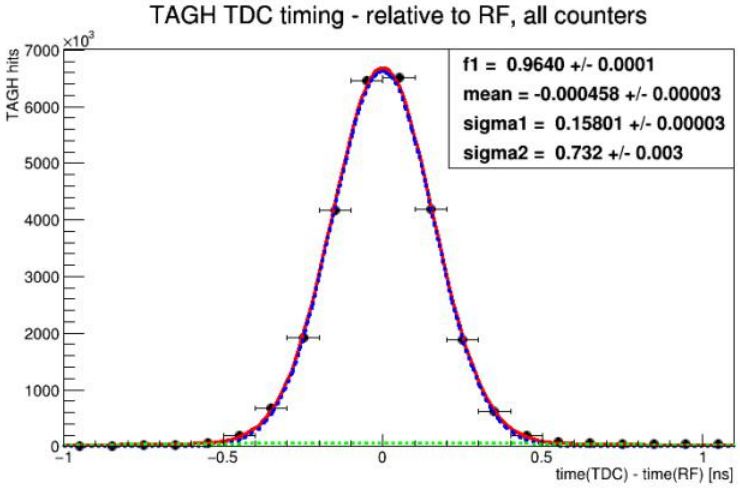

Figure 2.12: A histogram of the TAGH timing distribution with the bunch clock from the accelerator (RF) as a time reference. The result of the double Gaussian fit shows a timing resolution $\sigma = 167$ ps on average for all counters.

Due to the geometry of the fibers, the maximum efficiency of the TAGM is 78%. The design timing resolution is 200 ps and Fig. 2.10 shows the measured resolution. The TAGM electronics, testing, and calibrations will be discussed in greater detail in Sections 3.2, 3.4, and 4, respectively, as this was a major component of my research.

The TAGH is constructed of 218 scintillators coupled to PMTs and continuously samples electrons corresponding to photons in the energy range 9.1 - 11.78 GeV (Fig. 2.11). The calibrated timing resolution can be seen in Fig. 2.12.

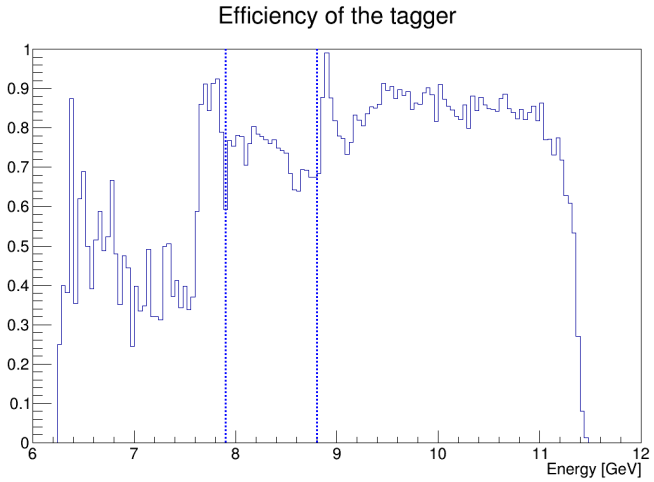

Figure 2.13: Efficiency of the tagging detector arrays for a particular run. Inside the blue vertical lines is the TAGM, and outside is the TAGH. The TAGM has a maximum design efficiency of 78% arising from the geometry of the fibers.

The efficiency of the tagging spectrometer can be seen in Fig. 2.13. For these detectors, the important quantity is the ratio of events seen by both the tagger and the pair spectrometer (explained below) to the number of events measured by the pair spectrometer. Because the pair spectrometer is after the collimator, this ratio indicates the fraction of beam photons reaching the experimental target whose energies are tagged by the tagger. In the figure, the blue lines represent the boundary between the TAGM and the TAGH. At energies above about 7.5 GeV, the TAGH is expected to have high efficiency whereas below 7.5 GeV, the efficiency is halved due to a reduced sampling. There are gaps between counters in the TAGH array in the low energy region but not in the high energy region. For the run used to generate Fig. 2.13, the TAGM had a partial upgrade which can be seen as an efficiency of approximately 70% near 9 GeV and an efficiency of 75% at lower energies.

During the commissioning runs, the tagging spectrometer (tagger) has been successful in measuring the photon beam energy and has been well calibrated. The TAGM calibrations will be discussed in 4.

2.2.3 Active Collimator

Once the photons are created, they travel 75 m downstream to a lead block collimator. There are two openings in this block: 3.4 mm and 5.0 mm. The purpose of the collimator is to prevent incoherent photons from entering the hall. The angular spread of coherent bremsstrahlung photons is smaller than the incoherent photons and can thus be cut out by this hole.

Mounted directly in front of this hole is the active collimator (AC). This device consists of 8 tungsten wedges corresponding to an inner and outer x and y wedge, as seen in Fig. 2.14. When the beam strikes the tungsten, it produces an electronic signal in all of the wedges. A simple difference over the sum between opposite wedge's signals (*eg.* inner +x and inner -x) can be made to determine the position of the beam, so long as the beam is within the circle of wedges.

This device is used to help the accelerator steer the beam into Hall D. When the beam is initially tuned to Hall D, the beam spot is placed near a pre-determined location. Because the active collimator is mounted to an x- and y-motor, the AC can then be scanned. The beam is left untouched while the AC is incrementally moved in either the x- or y-direction. To determine the optimal location for the beam, the intensity of the beam is measured within the hall at each AC position. Wherever the intensity was largest in both x- and y-directions is the new location for the accelerator to steer the beam.

Additionally, a method is being developed which will quickly raster the beam across the face of the active collimator in order to provide data for calibrating the signals from the wedges. This will be performed at the request of the run coordinator and will take less than a minute.

I installed this device in the Hall D collimator cave and am the local detector expert. Before each run, I make sure that the signals are working properly and that the baselines of the electronics are zeroed out. In addition, if there is ever a problem, like a missing signal, I help diagnose and fix the problem.

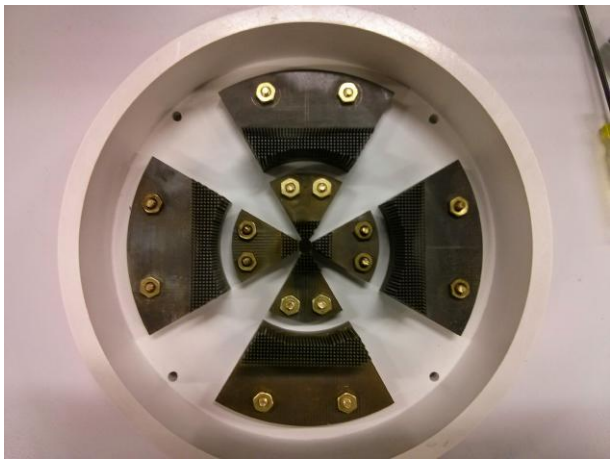

(a) Active collimator wedges

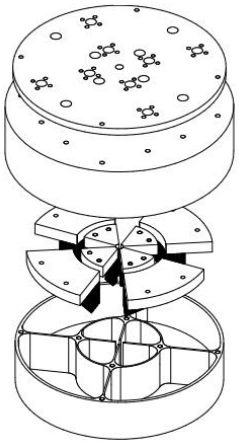

(b) CAD drawing of active collimator

Figure 2.14: Active collimator. (left) The inside of the active collimator with all 8 tungsten wedges visible. (right) After installation, the active collimator sits in front of the collimator with the beam coming from the right.

2.2.4 Pair Spectrometer

The flux of the collimated photon beam is measured by the pair spectrometer (PS) [14], which is located between the collimator and GlueX spectrometer, as seen in Fig. 2.4. The PS consists of a thin foil converter which creates e^+e^- pairs through pair production, a dipole magnet to separate their paths, and a hodoscope to detect the e^+ and e^- and extract timing and energy information. A schematic of the PS can be seen in Fig. 2.15.

The PS hodoscope is divided into two components: the fine and coarse counters. The former consists of 145 rectangular scintillator tiles for each arm which transfer the light pulses through wave-length shifting fibers onto Silicon Photomultipliers (SiPMs). The PSC is made of 16 scintillating counter PMTs, 8 per arm, and is used to measure the time of the electron or positron and to help reduce the background originating from interactions of the e^+/e^- in the magnet. Nominally, the PS is set up to detect photons in the range $6.0 \leq E_\gamma \leq 12.5$ GeV with a resolution of 30 MeV. There are 3 converters of different thicknesses installed which can be inserted remotely depending on the photon flux.

During the spring 2016 commissioning run, the PS had a detection efficiency of $> 95\%$ with a background coming from accidental coincidences between the right and left arms on

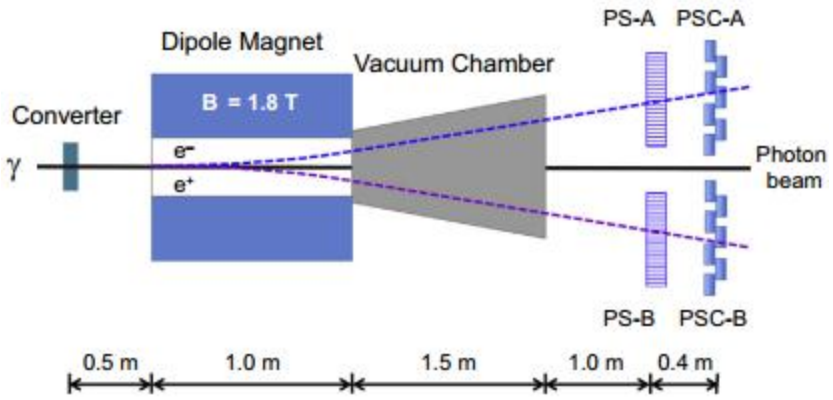

Figure 2.15: An overhead view of the pair spectrometer. The collimated photon beam interacts with the foil to produce an e^+e^- pair that is then separated by a dipole magnet and directed into the fine (PS) and coarse (PSC) counters.

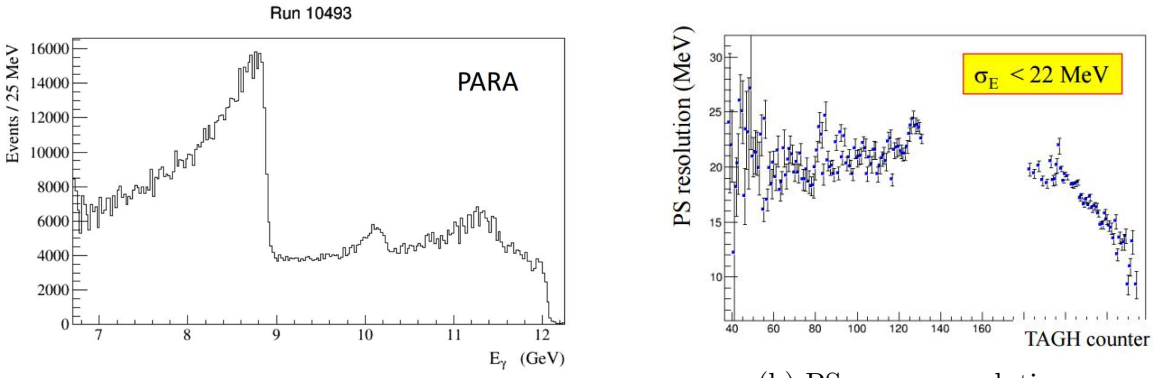

(a) PS energy spectrum

(b) PS energy resolution

Figure 2.16: (a) The photon energy spectrum measured by the pair spectrometer. The coherent edge can be seen at 9 GeV. (b) The PS energy resolution is shown as a function of corresponding TAGH counter number. The missing section corresponds to the TAGM.

the level of 1-1.5%. The energy spectrum and resolution can be seen in Fig. 2.16. The timing resolution was found to be < 150 ps with a design resolution of 250 ps.

2.2.5 Triplet Polarimeter

In order to measure the photon polarization, a triplet polarimeter (TPOL) has been installed between the collimator and the PS, as seen in Fig. 2.4. The TPOL uses triplet photoproduction, $\gamma e^- \rightarrow e^-e^+e^-$, by having the photon incident on a beryllium foil where it interacts with the electron's electric field to produce an e^+e^- pair, which is detected in

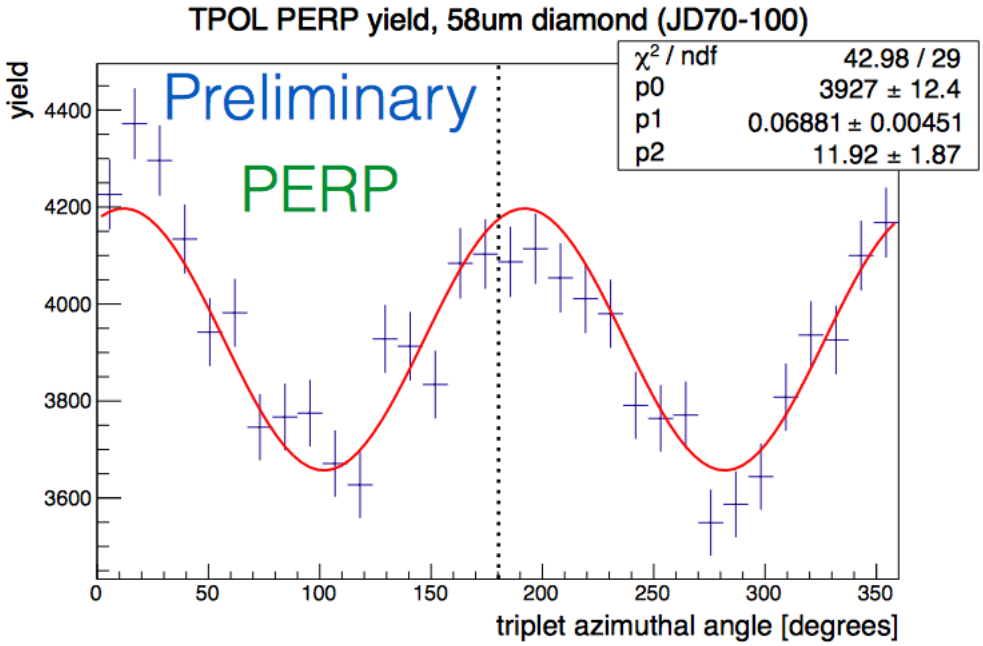

Figure 2.17: TPOL ϕ distribution fit with $A[1+Bcos(2\phi-2\phi_0)]$ with a polarization of 35.6 $\pm$ 2.3 %.

the PS, and a recoil e^-, detected by the TPOL. The e^+e^- pair is directed in the forward direction along the beam axis. The angular distribution of the recoil e^- provides information about the beam polarization. For linearly polarized photons, $\sigma = \sigma_0[1+P\Sigma cos(2\phi)]$, where σ_0 is the unpolarized cross section, P is the photon polarization, Σ is the analyzing power, and ϕ is the azimuthal angle of the recoil e^-. A fit of the ϕ distribution using the function $A[1+Bcos(2\phi-2\phi_0)]$ was used on commissioning data, where the polarization is determined by B/Σ. Parameter ϕ_0 corresponds to the offset between the detector and the polarization plane and is ideally 0. This can be seen in Fig. 2.17.

The TPOL [15] uses an S3, double-sided silicon strip detector with 32 azimuthal sectors on the ohmic side and 24 concentric rings on the junction side, as seen in Fig. 2.18. This results in 768 resolvable angular regions which measures the azimuthal distribution with high precision [16]. There are two foils used by the TPOL, 75 and 750 μm thick.

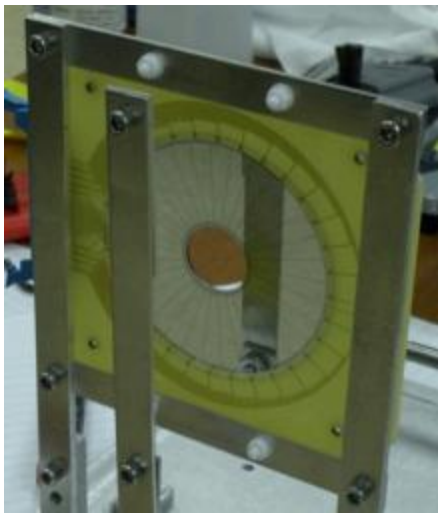

Figure 2.18: View of the sector side of the TPOL. The outer diameter is 70 mm and inner is 22 mm.

2.3 GlueX Spectrometer

A schematic top view of the GlueX detector is show in Fig. 2.19. The photon beam collides with the liquid hydrogen target which is surrounded by the start counter (SC). The central drift chamber (CDC) tracks charged particles that emerge from the target at polar angles above 10 degrees, and the forward drift chamber (FDC) tracks the forward-going charged particles. Around the CDC and FDC is the barrel calorimeter (BCAL) which measures the energy of particles which emerge from the target with polar angles above 10 degrees, and the forward calorimeter (FCAL) measures the energy of forward going particles. In front of the FCAL is the time-of-flight detector (TOF) which measures the timing of the forward particles which helps in particle identification (PID). A solenoid magnet surrounds all but the FCAL and TOF which allows particles to have their charge and momentum measured. The solenoid consists of 4 coils that run at a nominal current of 1350 A with a field of 2.08 T. This high field is important for analyzing charged particle momenta and to suppress the low energy electromagnetic background generated by photons near the beam axis. The target is 30 cm in length with an upstream inner diameter of 2.42 cm and a downstream diameter of 1.56 cm.

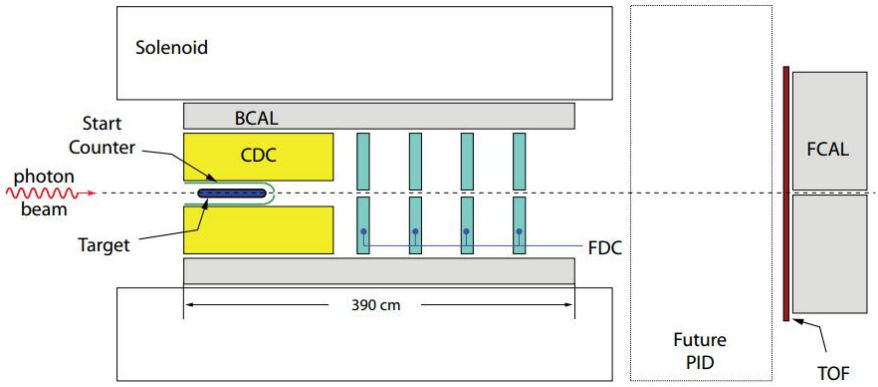

Figure 2.19: GlueX spectrometer schematic (top view) [17].

2.3.1 Start Counter

The SC envelopes the target and is the first detector to measure the outgoing particles which is why its called the start counter. Its purpose, in coincidence with the tagger, is to identify the electron beam bucket associated with the detected particles at rates up to 10^8 γ/s. It provides $\sim$90% of 4π coverage with 30 scintillator paddles. These paddles have pointed ends that bend inward the beam at the downstream end, as seen in Fig. 2.20. Each paddle is read out by 4 SiPMs whose signals are summed before being digitized by the data acquisition system. SiPMs were chosen since they are not affected by the high magnetic field. The timing performance of the SC is seen in Fig. 2.22 which shows better resolution than the design goal for each sector.

2.3.2 Tracking

Tracking in GlueX is performed by two drift chambers, the central drift chamber (CDC) [18] and forward drift chamber (FDC) [19]. These detectors work by having sense wires at a high voltage relative to a nearby reference electrode while filled with a gas mixture. Each wire layer is strung at a different angle to pin-point the location of a track. Ionization left behind by charged particles drifts toward a wire and it is this drift time which provides the spatial resolution.

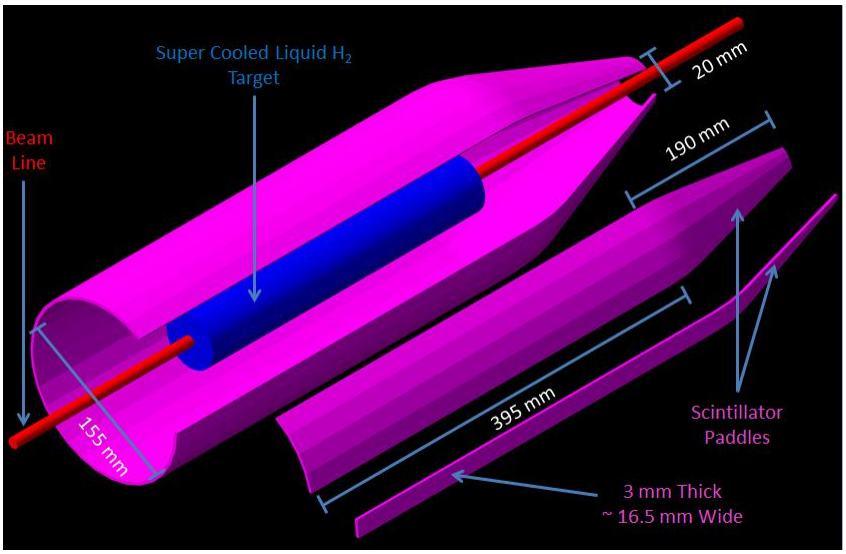

Figure 2.20: Start Counter CAD drawing surrounding the liquid hydrogen target.

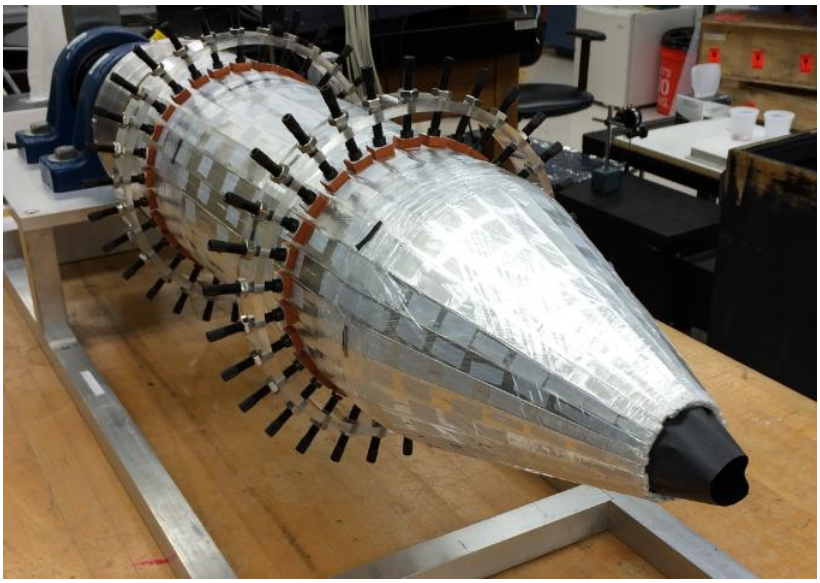

Figure 2.21: The start counter assembly before an additional layer of material was added for light tightness.

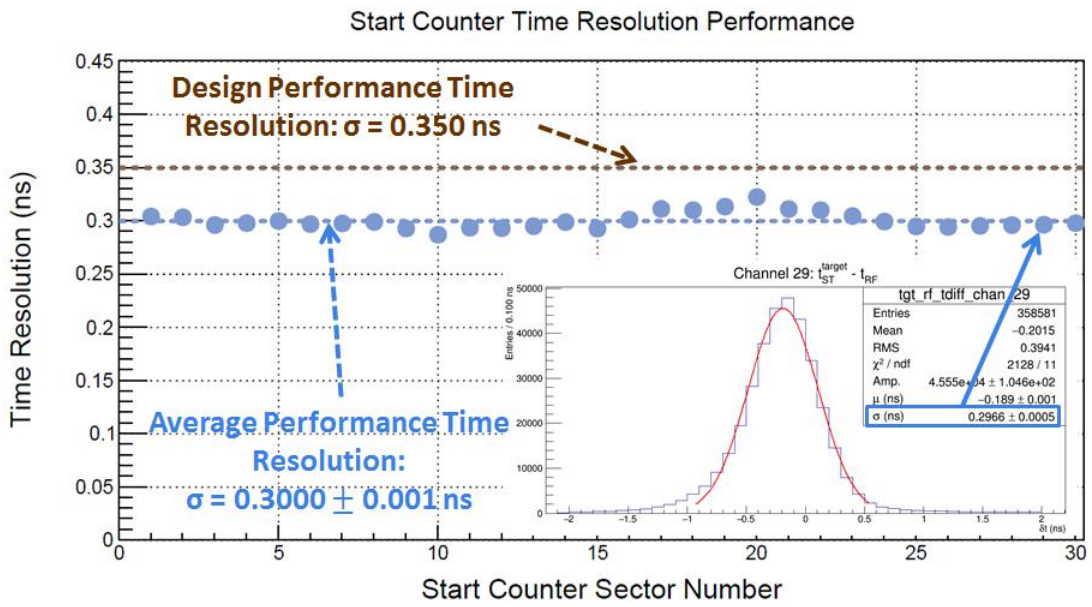

Figure 2.22: After calibrations, the start counter timing resolution has exceeded the design goal of 350 ps for all sectors.

The CDC surrounds the SC and is a cylindrical drift chamber, seen in Fig. 2.23, and detects particles with $\theta > 10°$, where the incident beam direction is the z-axis and θ is the polar angle. It consists of straw tube layers that are strung in 12 axial and 16 stereo ($\pm$ 6°) configurations, as seen in Fig. 2.24. The straw tubes contain an anode wire of diameter 20 μm with the inner wall as the cathode to ensure a uniform electric field. The CDC is filled with a mixture of argon and CO_2 gas. It measures both r and ϕ for charged tracks with a resolution of 200 μm as well as timing and dE/dx, as seen in Fig. 2.25.

Downstream of the CDC is the FDC which detects forward going charged particles up to $\theta \simeq 20°$. It consists of 24 planar drift chambers (cells) with cathode strip and wire readouts grouped into 4 packages of 6 cells (see Fig. 2.26). A cell consists of 1 layer of U cathode strips, 1 layer of sense and field wires, and 1 layer of V cathode strips, arranged such that the U and V layers are skewed, as seen in Fig. 2.27. Each cell in a package is rotated 60° relative to the proceeding cell and contains a mixture of argon and CO_2 gas. The FDC is able to provide tracking as well as dE/dx information for forward-going charged particles with a spatial resolution of 250 μm, as seen in Fig. 2.28).

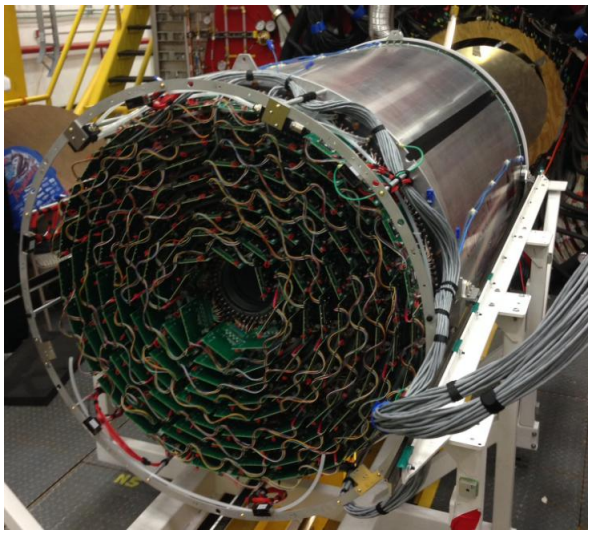

Figure 2.23: The fully assembled CDC before installation into the solenoid magnet.

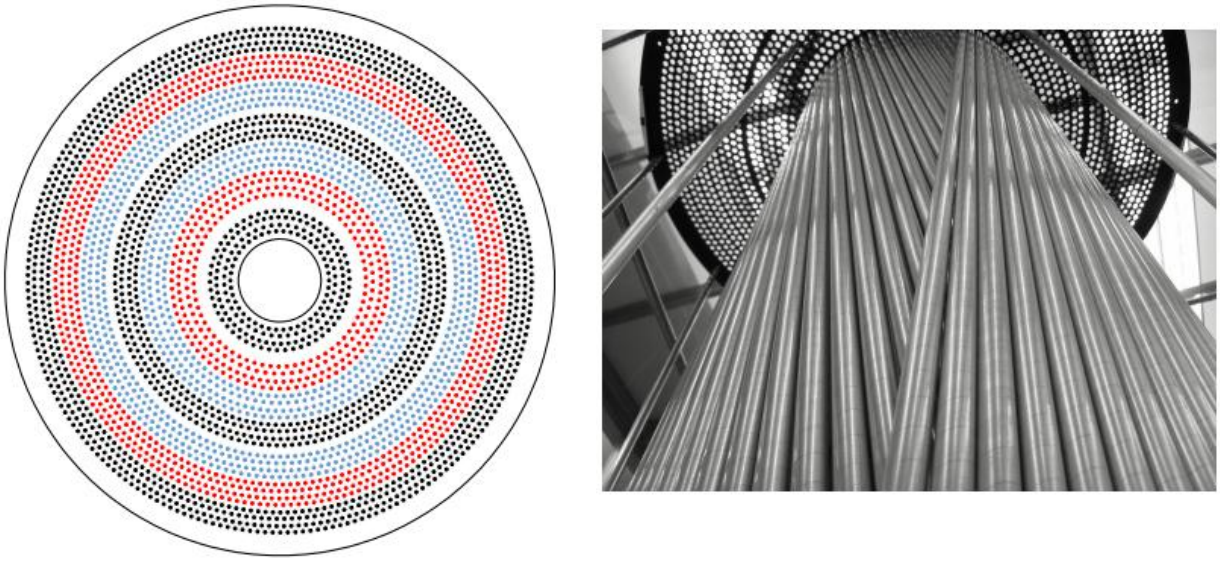

Figure 2.24: CDC design. (left) CDC straw tube configuration from the upstream end. Axial straws are black, $+6°$ are red, and $-6°$ are blue. (right) A view of the stereo straw tubes in layers 8 and 9 [20]

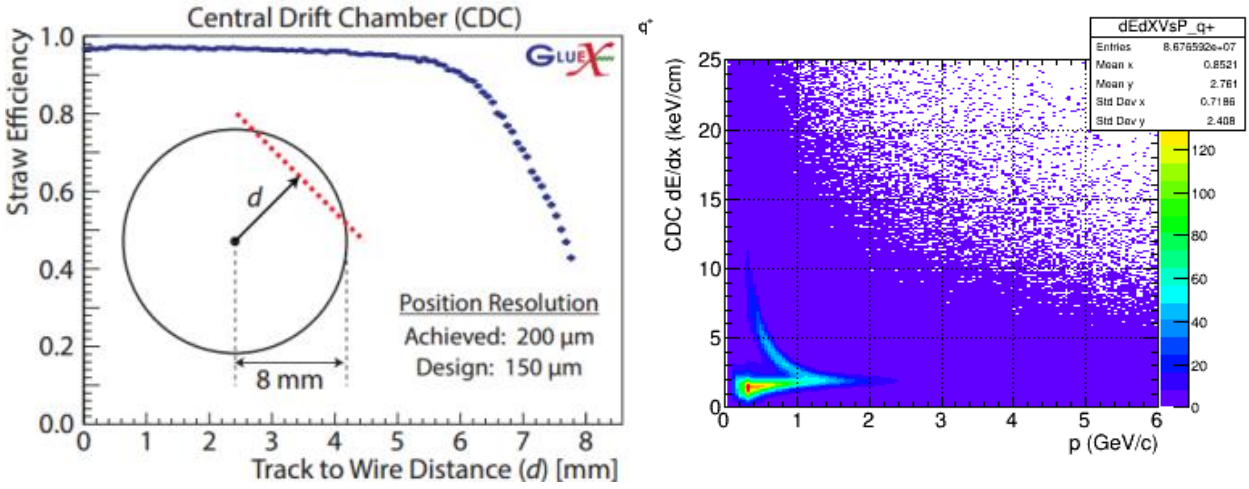

Figure 2.25: CDC Performance. (left) Straw tube efficiency as a function of track distance from the wire. (right) CDC dE/dx as a function of momentum for positively charged tracks. The curved band represents protons while the horizontal band is π, K, etc.

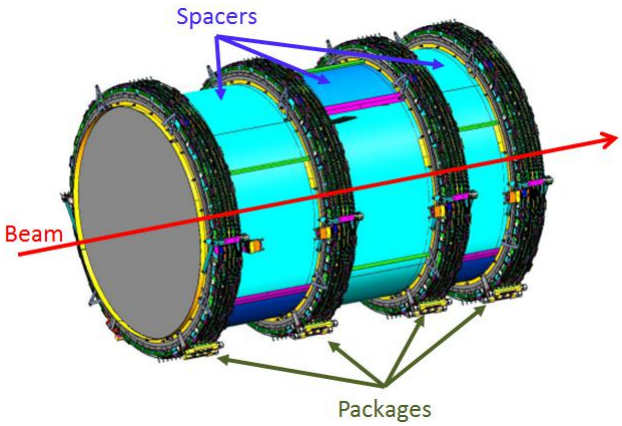

Figure 2.26: FDC 3D representation showing the 4 packages.

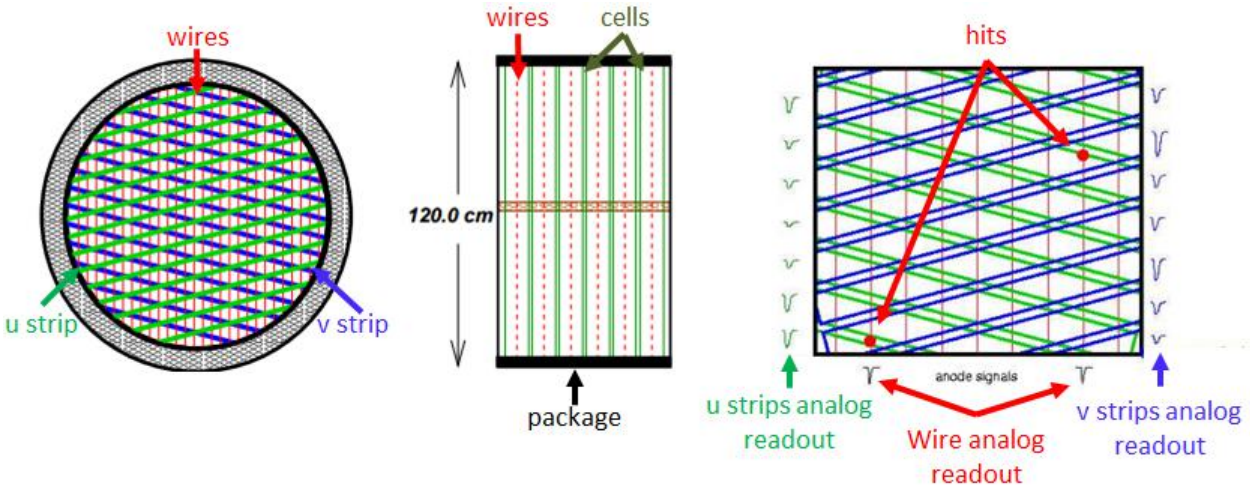

Figure 2.27: FDC cell wiring. The U and V cathode strips are angled at +75° and −75° from the wire.

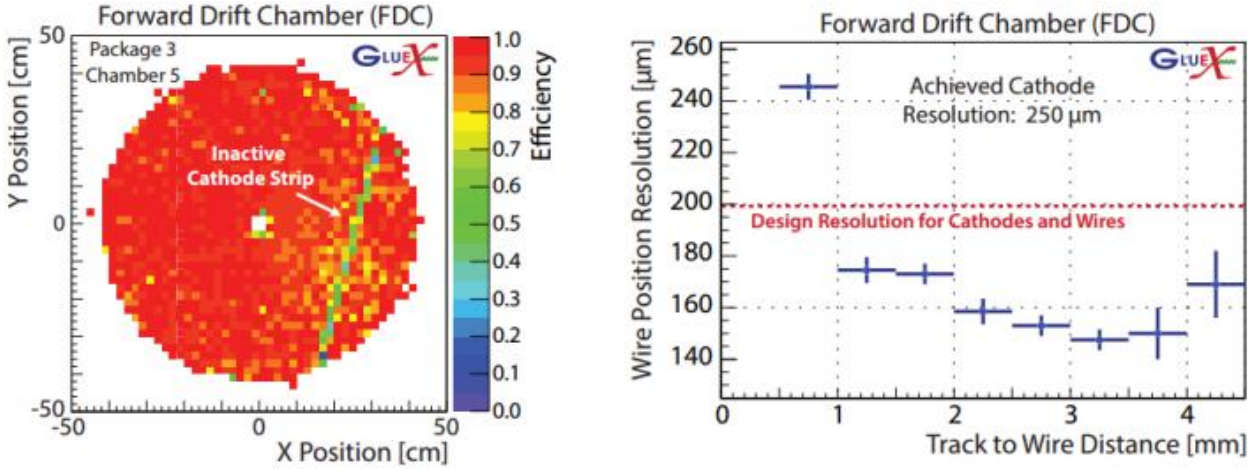

Figure 2.28: FDC performance. (left) Efficiency map of package 3, cell 5. (right) Wire resolution as a function of track distance from the wire.

2.3.3 Calorimeters

The calorimeters in GlueX are the barrel calorimeter (BCAL) [21] and forward calorimeter (FCAL) [22]. Particles interacting with these detectors create electromagnetic showers which are used to reconstruct π^0's and η's produced by the reaction's decay products [12]. These detectors measure the energy of these showers. In addition, the BCAL and FCAL are segmented for particle tracking.

The BCAL measures the energy of particles within the solenoid, $11^\circ \leq \theta \leq 126^\circ$, using scintillating fibers running axially along the entire detector (Fig. 2.29). It is composed of azimuthal sectors which contain alternating layers of lead and scintillating fiber (Fig. 2.30). Particles interacting in the lead will produce showers which cause the fibers to scintillate and are read out by SiPMs. The energy resolution is $\sigma_E/E = 5.4\%\sqrt{E} \oplus 2.3\%$, with a time difference resolution of $\sigma_{\Delta T/2} = 70$ ps$/\sqrt{E}$, and a z-position resolution $\sigma_z = 1.1$ cm$/\sqrt{E}$ [23]. The BCAL reconstruction of π^0's from the spring 2016 run can be seen in Fig. 2.31.

Forward-going particles, $\theta < 11^\circ$, are measured by the FCAL which has a planar geometry orthogonal to the beam axis (Fig. 2.32). It is composed of F8-00 lead glass blocks that have been used in previous experiments with new photo-tubes and bases. The energy resolution σ_E/E is $5.6\%/\sqrt{E} \oplus 3.5\%$, with a timing resolution of $\sigma_t = 0.4$ ns, and a position resolution of 6.4 mm$/\sqrt{E}$ [24]. The performance of the FCAL in reconstructing π^0's can be seen in Fig. 2.33.

2.3.4 Particle Identification Detectors

The time-of-flight (TOF) [25] detector is designed to provide particle identification (PID) in the low momentum range through the measurement of the particle velocities. It has two planes of scintillator paddles, one horizontal and one vertical, each 6 cm wide and 2.54 cm thick (see Fig. 2.34). The TOF design allows for the acceptance of charged tracks with $1^\circ \leq \theta \leq 11^\circ$ and its performance can be seen in Fig. 2.35.

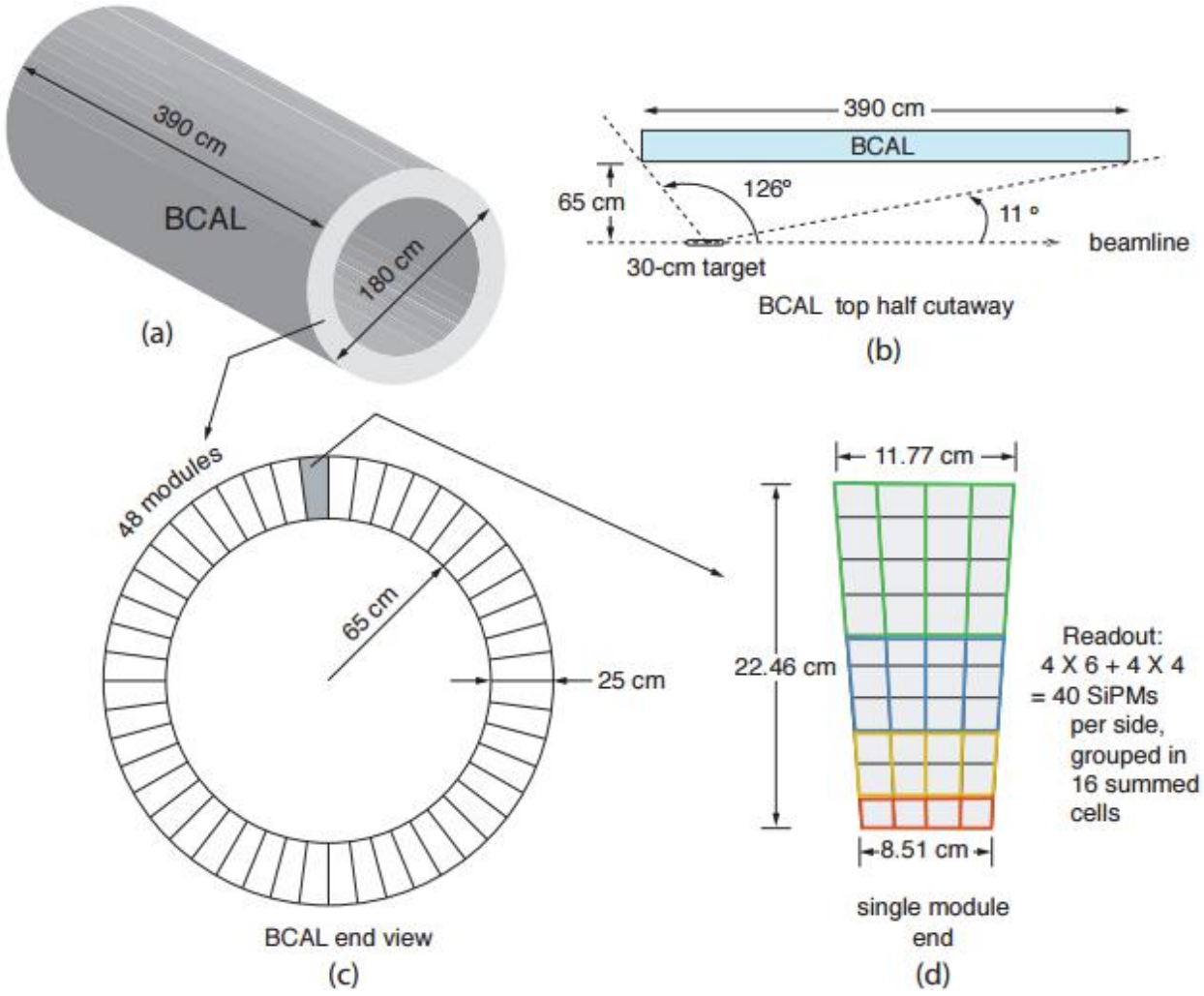

Figure 2.29: BCAL overview. (a) isometric view of the BCAL, (b) side view of the BCAL with polar angle acceptance, (c) end view showing azimuthal segmentation (d) readout module and light guide geometry.

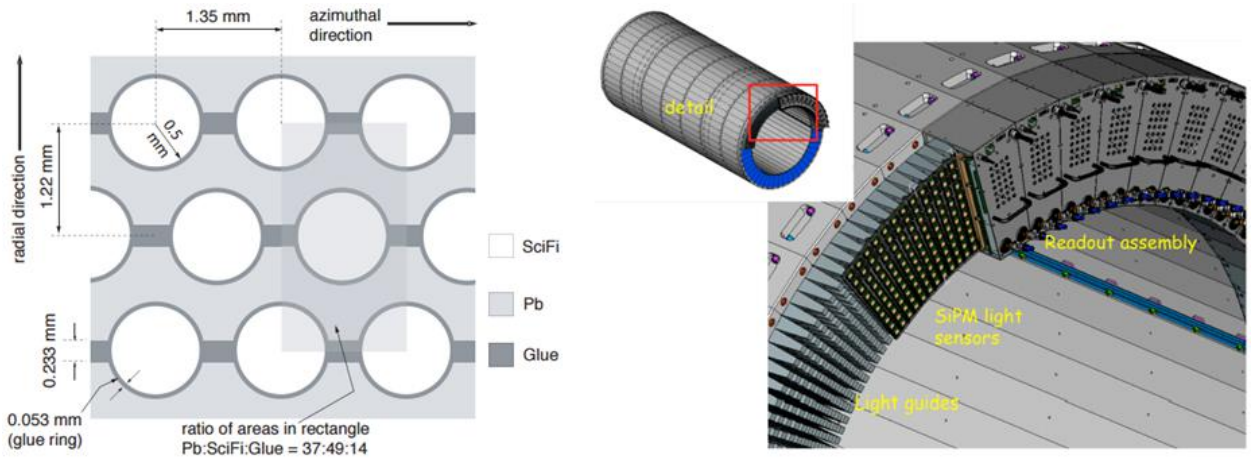

Figure 2.30: (left) lead and scintillator layer matrix (right) CAD drawing of the BCAL readout system

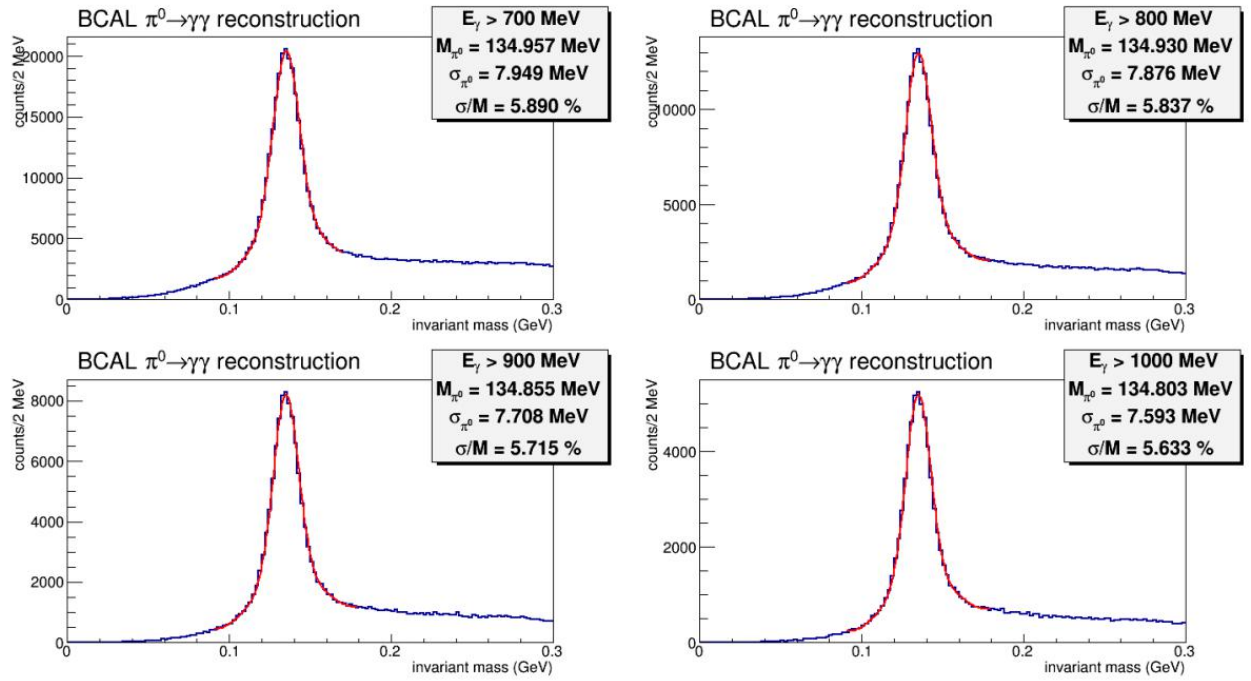

Figure 2.31: BCAL π^0 reconstruction from the spring 2016 run period. The mass resolution of the π^0 improves with increasing shower energy, as expected [23].

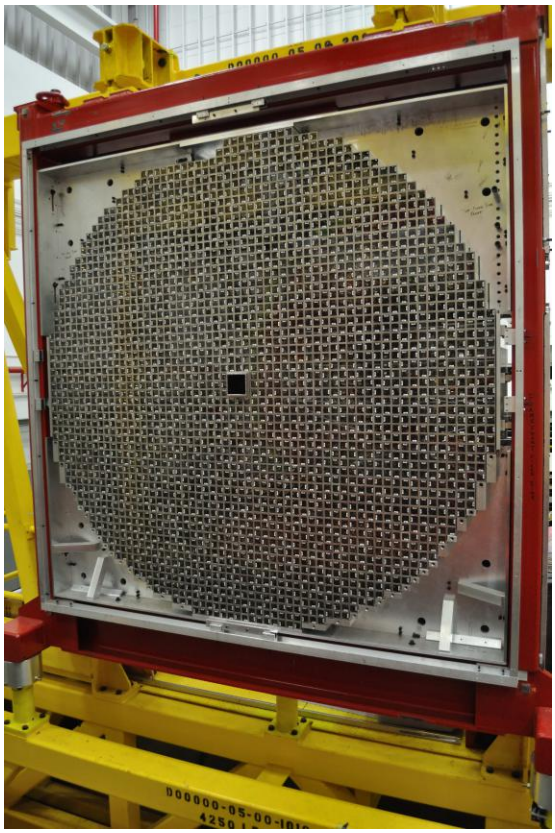

Figure 2.32: Fully assembled FCAL without dark room enclosure.

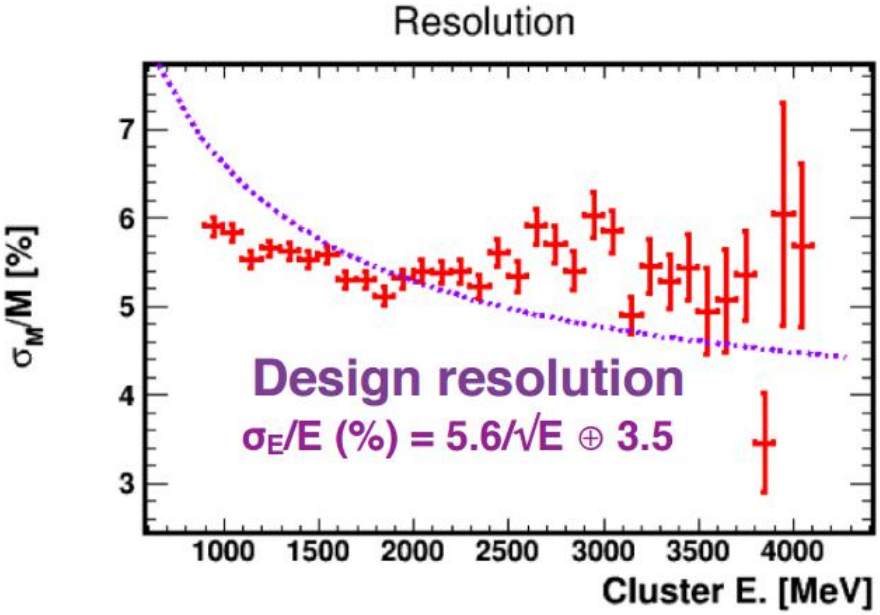

Figure 2.33: FCAL performance

Figure 2.34: The TOF is located downstream of the solenoid magnet and consists of horizontal and vertical scintillator paddles.

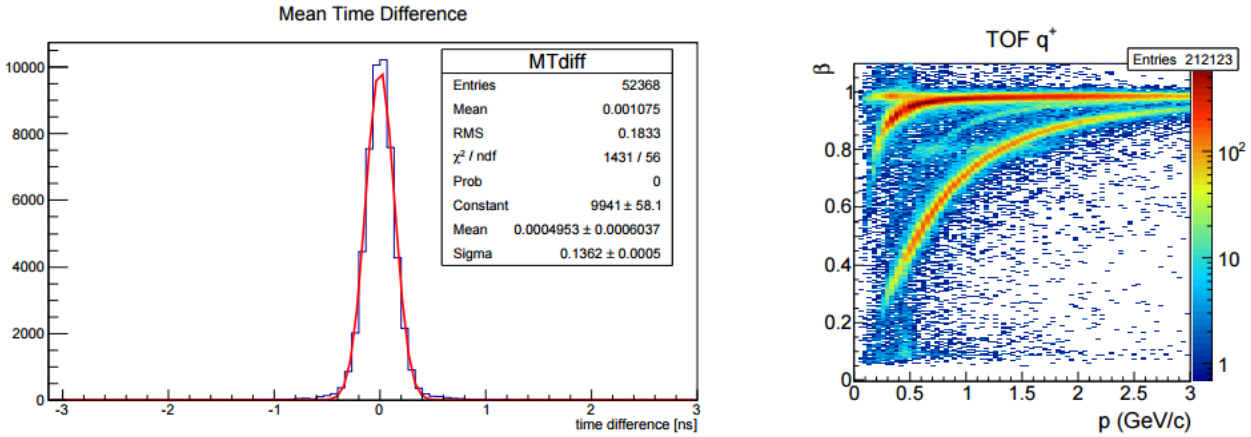

Figure 2.35: (left) The time difference between the TOF paddles for matched charged tracks. The sigma of 136 ps corresponds to a time resolution of 96 ps for each layer. (right) β as a function of momentum is histogrammed for positively charged tracks in the TOF. e's, π's, K's, and p's (top to bottom) each have their own band. The horizontal line at $\beta = 0.8$ comes from an RF bunch mismatch.

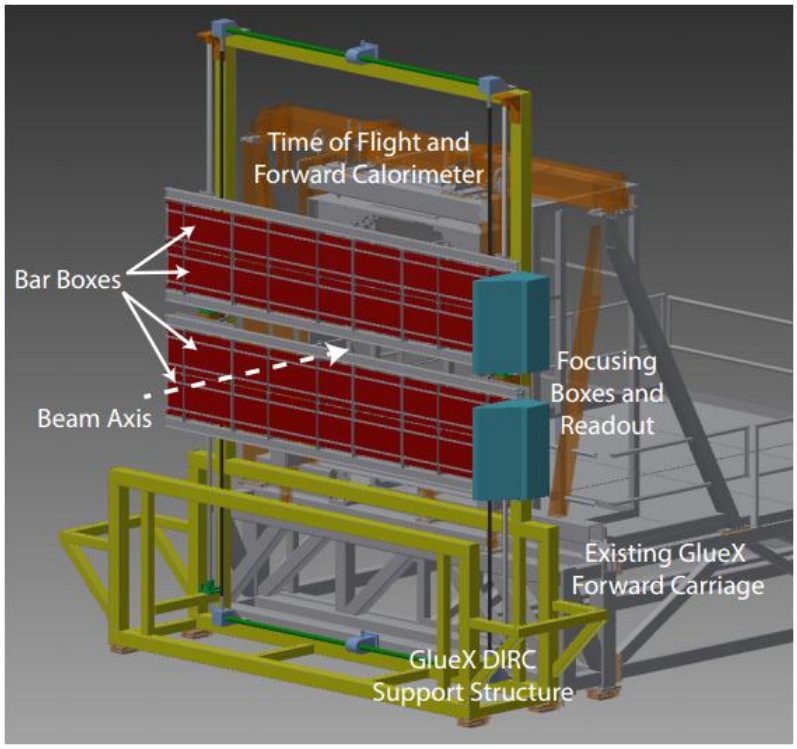

Figure 2.36: The DIRC will be placed directly upstream of the TOF and FCAL. The 2 BaBar boxes will be mounted horizontally and will provide π/K separation up to 4 GeV.

A future detector called the FDIRC (forward detection of internally reflected Cherenkov) [26] will enhance the identifications of kaons up to a momentum of 4 GeV as well as reduce experimental background from misidentified particles (Fig. 2.36). This will increase GlueX's ability to study hybrid mesons with kaon final states. The FDIRC will be constructed using the decommissioned synthetic fused silica bars from the BaBar DIRC detector. It is expected to be installed in 2018.

CHAPTER 3

Tagger Microscope Design and Construction

3.1 Introduction

The primary focus of the author's contribution to the GlueX project was on the Tagger Microscope (TAGM) which was reviewed generally in the previous chapter. A detailed description of the design and construction of the detector is outlined in the following section. As a reminder, the TAGM is part of a larger tagging spectrometer which measures the energy and arrival time of post-bremsstrahlung electrons. The fixed-array tagger hodoscope (TAGH) measures the electrons outside of the primary coherent peak and is useful in aligning the diamond radiator. Both use energy conservation and precision timing to *tag* the energy of individual photons incident on the target within the selected energy range. Within the coherent peak, the TAGM provides high efficiency tagging with good energy and time resolution.

The experimental requirements of the TAGM are as follows:

1. 200 ps timing resolution.
2. At least 95% counting efficiency in each channel.
3. $\leq 0.1\%$ r.m.s. energy resolution. [27]
4. Tagging efficiency of at least 70%.
5. Operate with the above efficiency and resolution at rates up to 500 MHz/GeV.

Standard photo-multiplier tubes are not ideal candidates for photon counting in the coherent peak region due to the necessary high voltages, their relatively large size, and their inability to handle large rates. The high rate and efficiency requirements are better met by using a scintillating counter detector with silicon photo-multipliers (SiPM). The compact size of SiPMs meets the required energy resolution listed above. The technical requirements will be discussed in the next sections.

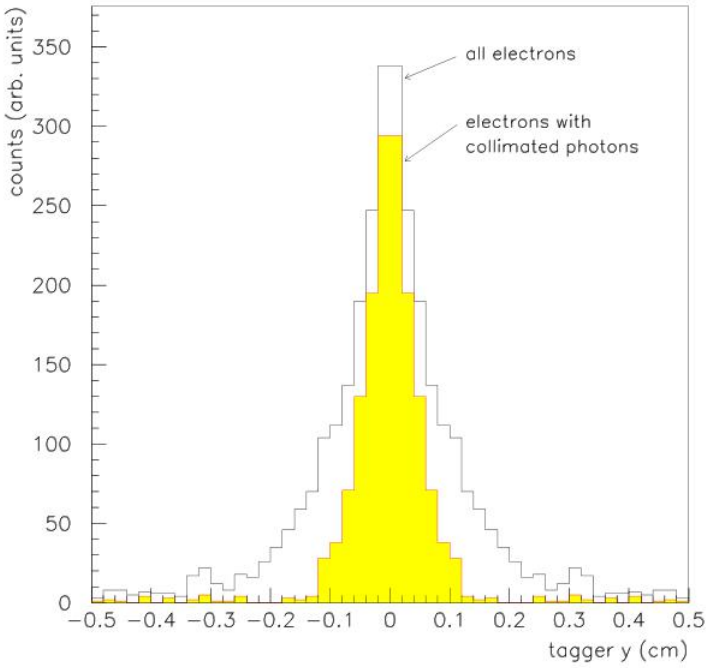

Figure 3.1: y-axis projection of electron beam on TAGM counters

Due to conservation of momentum, a bremsstrahlung photon which deviates from the beam axis before the magnet must correspond to the electron's deviation in the tagger. Any photon emitted at some angle above the zx-plane[1] has its corresponding electron below the spectrometer mid-plane upon entering the magnet. Tagging efficiency lost to photon collimation can be recovered by taking advantage of this feature by instrumenting the focal plane with a two-dimensional counter array. By aligning the stripe of the dispersed electrons along the central row, readout from all other rows can be turned off. Figure 3.1 shows the projection of electron flux on the y-axis, produced by simulating the particle beam with tagger and quadrupole magnet optics. The highlighted section indicates photons which pass through the collimator. Using a single row for readout equates to clipping the tails of this distribution which minimizes the tagging of photons that can never reach the GlueX target. From the figure, a counter width of 2 mm would suffice.

[1]The accelerator's coordinate system is such that the beam direction is the z-axis with the y-axis in the vertical direction

The above argument encourages the feature of being able to selectively turn on or off a given channel in the microscope. However, this does not mean that each channel must have its own dedicated readout which would be turned off most of the time. This would be wasteful and would require many additional cables. Instead, each channel in a column, corresponding to an energy bin, can be summed into a single readout channel. Turned off channels do not contribute signal pulses to this sum. It is also useful to have some set of individual-fiber signals being digitized in order to measure the vertical beam intensity distribution and help optimize the tagger and quadrupole optics. In addition to the summed readouts, occasional columns are instrumented with individual readout capabilities.

With the vertical dimension understood, the horizontal width of the counters needs to be determined. Considering the photon energy, desired energy resolution, and counting rate, it can be seen that a 9 GeV beam with 0.1% resolution (9 MeV), equates to a counter width of 30 MeV and a resulting rate of about 14 MHz per channel at the peak. Operating at this rate would lead to a high occurrence of pulse overlap, and consequently, lower the counter efficiency. If, instead, a 2 mm (8 MeV) width counter is used, the rate comes down to 3.6 MHz, which is acceptable. This leads to a design of 2 mm x 2 mm counters. An obvious choice for fast counters of these dimensions are square scintillating fibers, which can be purchased commercially and include necessary cladding to minimize light loss and optical cross-talk between channels. Square scintillating fibers from Saint-Gobain, BCF-20, were chosen as they meet the design specifications and provide better stacking efficiency than round fibers.

Figure 3.2 shows a diagram of the scintillating fibers along the focal plane of the electrons. The red stripe indicates the ideal alignment of the electrons, and the blue columns represent those which have individual readouts instrumented. There are 102 total columns and a total of 510 fibers where bundles are grouped in 6 columns of 5 rows for a total of 30 fibers per bundle.

[2]When the TAGM was first installed, only the first 100 columns were instrumented for readout due to cable restrictions. As of the fall 2016 run, all 102 columns are read out

Figure 3.2: A diagram of the TAGM scintillating fibers along the focal plane. The red stripe indicates the row with the aligned electrons and the blue columns represent columns with individual readout. There are 5 rows of 102 columns for a total of 510 fibers[2]. Electron energy increases from left to right.

The length of the scintillator was determined through an optimization of light yield and cross-talk between the counters due to electron multiple-scattering. It was determined that a 2 cm long scintillator would be used where the end is fused to a light guide which propagates the signal to a photo-sensor. A sensor positioned at the end of the scintillator would be difficult to mount and would expose it to the electron beam. To avoid the electron plane, each bundle is mounted on a separate metal block called the "S-bend" due to its shape, as seen in Figure 3.3. Simulations also showed significant levels of neutron radiation which suggested a design with the sensors protected in a shielded enclosure. A conceptual diagram can be seen in Figure 2.9.

For the photo-sensor, a solid-state device called a silicon photomultiplier (SiPM) was chosen. The reasons for this choice were driven by several factors:

1. Low cost per channel (no high voltage power supply required).
2. Operation inside a magnetic field (stray field from the tagger magnet).
3. Fast readout, capable of meeting the design timing resolution.
4. Gain of order 10^6, consistent with small scintillation flash readout.
5. Compact size with a small active area to match the fiber cross-section.

It is these characteristics that make SiPMs more attractive than traditional photo-multiplier tubes (PMTs) [28]. The device chosen, a Hamamatsu S10931-050P, contains a 3 x 3 mm active area containing 3600 pixels. Each SiPM is reverse-biased to a few volts over breakdown threshold and operates in Geiger mode, which produces an avalanche of electrons when a photon is incident on a pixel. All pixels that absorb a photon contribute

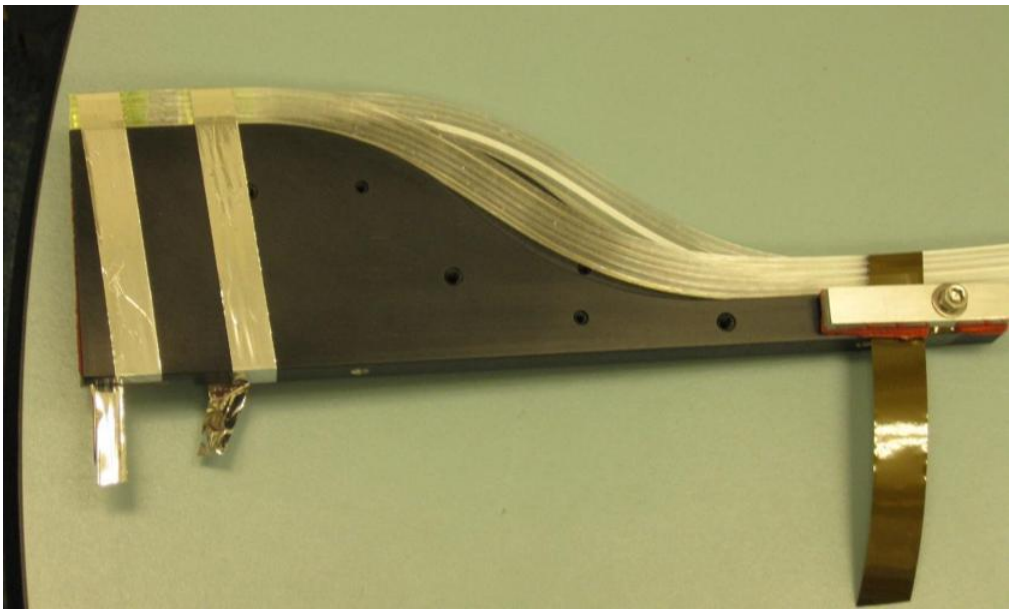

Figure 3.3: The black metal mount follows the s-bend in the fibers, which guides them underneath the horizontal electron plane.

an equal amount of charge to the pulse which creates a high dynamic range. These SiPMs have a photon detection efficiency greater than 40% at 492 nm, the peak wavelength from the scintillator.

The scintillator has a decay time of 2.7 ns which can be interpreted as an exponential probability density distribution for the emission of a single photon. The uncertainly on the leading-edge timing of pulses with an average of N detectable photons is roughly 2.7 ns/$\sqrt{N}$. In order to meet the 200 ps requirement, at least 180 photons must be detected on average. Looking at the scintillator, the values of 8000 γ/MeV and 2 MeV/cm energy deposition in a 2 cm scintillator by an electron results in 32,000 γ/scintillation. The fiber capture cone is estimated to be 5.6% (conservative and simplified assumption of round fibers) and, combined with worst-case attenuation at fiber junctions and coupling to the SiPM, the estimated delivery fraction is 4.5%. The photon detection efficiency (PDE) for green light (492 nm) is about 20%[3] for the Hamamatsu devices. When combining the capture and

[3]Hamamatsu quotes a larger PDE which includes a big after-pulsing yield that does not contribute to the statistics at the leading edge.

detection efficiencies and including saturation effects, the number of pixels fired is over 550[4]. This is well within specifications.

Electrons traveling through the tagger magnet are curved towards the TAGM which is positioned with the scintillating fibers on the focal plane. Within this enclosure are circuit boards with mounted SiPMs. To reduce background light, these are kept in a light-tight compartment. The signal must be transmitted to the digitizing electronics in order to be read out by the experiment's data acquisition system (DAQ). The output signals from the TAGM are split between a flash analog to digital converter (fADC) and a leading edge discriminator (LED) which feeds into a time to digital converter (TDC).

The following sections cover the electronics required to operate the TAGM. I entered the group when the first prototype had been made and it did not meet our desired performance. My task was to understand why and to fix the problems. The next section describes each board's purpose as well as explain the improvements made.

3.2 Electronics

The final design for the microscope electronics involves three separate circuit boards: the preamplifier to increase the signal from the SiPMs, the control board to provide the proper voltages and for monitoring, and a backplane to interface between the preamplifier and control boards. Each preamplifier contains 15 SiPMs, corresponding to 3 columns. The fully instrumented detector required 34 preamplifiers, 17 control boards, and 6 backplanes to operate but additional boards were made for spares. Each of these elements will be discussed in this section.

[4]Saturation of a SiPM occurs at higher incident photon counts, where some photons hit already activated pixels. The average number of pixels fire, N_{fire}, as a function of incident photon number, N_γ, is $N_{pix}[1 - exp(-\eta N_\gamma / N_{pix})]$, where N_{pix} is the number of pixels in the device, 3600 in this case.

Table 3.1: Jefferson Lab's flash ADC module (fADC250) specifications

Quantity	Value
Input impedance	50Ω
Polarity	negative
Input range	0.5 V, 1 V, or 2 V
Sampling rate	250 MSPS
Resolution	12-bit

Table 3.2: Design performance requirements for the preamplifier electronics.

Specification	Performance Requirement
200 ps	fast-rising edge sufficient width for timewalk corrections
95% efficiency	$t_{fall} \leq 20$ ns
diagnostic mode	high gain mode to resolve single photons measure detection efficiency and gain of SiPMs
channel-to-channel consistency	$\leq 15\%$ gain variation as function of transistor β
fADC range	pulse amplitudes consistent with -0.5 V, -1.0 V, -2.0 V modes
50Ω output impedance	impedance matching on long traces in output

3.2.1 Preamplifier

SiPMs can be considered weak current sources that require a trans-impedance amplifier to increase the signal into something usable by the digitizing readout electronics. The TAGM is designed to work with a leading edge discriminator and a flash analog-to-digital converter (fADC) (3.1) created by JLab with the original signal from the front-end split in a passive splitter and fed to both. The discriminator sends its output signal into a time-to-digital converter (TDC) which digitizes the arrival time of the pulse. The fADC is used to verify the signal quality. Ultimately, it is the timing and channel number which provide the important information for the experiment (time and energy).

The performance requirements for the preamplifier can be seen in table 3.2. While developing a circuit design for the preamplifier, a simulation was created using Matlab. This was based on a system of linear equations of the passive components (basic voltage and current rules) as well as a linearizion of transistor equations from the Gummel-Poon

model [29]. The program first solves for the quiescent points of the transistors and then performs a linear expansion of the transistor response around these points. After this, the circuit's response is calculated for each input frequency for each net. A modeled input signal is simulated by using the components of its Fourier series.

As mentioned previously, the board must be capable of providing readout from both the individual SiPMs as well as the sum of 5 from a given column. This requires a two-stage amplifier. The first stage amplifies each SiPM and drives the individual channel signal output. In addition, this signal is sent into the second stage which sums the signals in the column to provide one summed output signal for the energy bin. For the final detector, only select columns were cabled for individual readout. The primary signals used for tagging come from the summed outputs.

The gain of the amplifier was constrained to produce output signals within the operating range of the fADC, with pulse heights that make maximum use of its dynamic range. To understand the device better, a high-gain mode was incorporated into the design to allow for the measurement of the photoelectron peaks of the SiPM. This is needed in order to understand how many photons are hitting the SiPM in order to understand the timing resolution. When a photon interacts with the SiPM, it causes one of the pixels to fire. One way to understand how many pixels are triggered is to look at the single pixel peak distribution when operating in high-gain mode. In Fig. 3.4, a spectrum of peaks can be seen where the first peak at 45 adc is the size of a single pixel's signal, the second peak is the signal size of two pixels, and so on. The space between peaks should be uniform, and here it can be seen to be 45 adc for these settings. This is used to convert the production signal into the number of pixels fired.

Based on these requirements and general rules of RF circuit design, the following guidelines were created:

1. Input and output must be AC coupled.

2. The 250 MHz sampling rate offers a Nyquist frequency upper bound of 125 MHz.

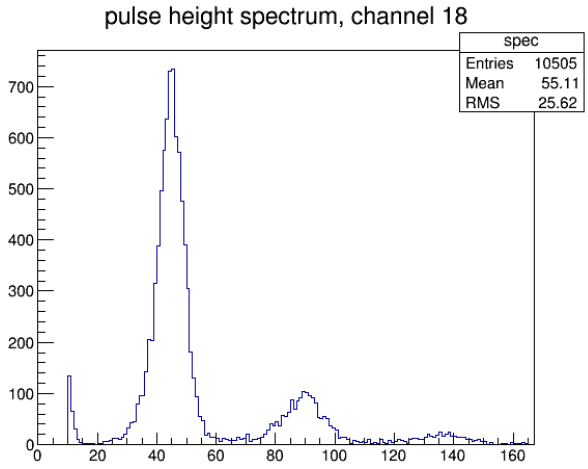

Figure 3.4: Dark pulse height spectrum for a SiPM with the preamplifier operating in high-gain mode. The yield can be seen on the y-axis while the number of ADC counts (the pulse height) can be seen on the x-axis. The primary peak at 45 comes from single-pixel events, at 90 from a 2-pixel events, and so on.

3. Optimized high-frequency response (within above bounds) to achieve a narrow pulse (fast rise time/low dead time).

4. Tuned lower bound of frequency band to minimize swing after the peak to minimize baseline shifts.

5. Minimal coupling of noise: low response in common noise bands and good isolation to avoid feedback and cross-talk.

6. Stability: signal-path inductance minimized to avoid resonances.

A major focus of the design was spent on achieving a fast rise time. The amplifier and summing circuit inputs, which can be modeled as current injectors, needed to be low impedance to prevent large RC integration times. This was solved by connecting these inputs to the emitters of the input stage transistors. Simulations with a 2 mA quiescent collector current showed a 13.5 Ω and 27.3 Ω input impedance for the amplifier and summing circuit, respectively [27].

A schematic of the final production preamplifier can be see in Figs. 3.5 and 3.6. The FET switch in the summing circuit effectively controls the resistance on the transistor Q_4

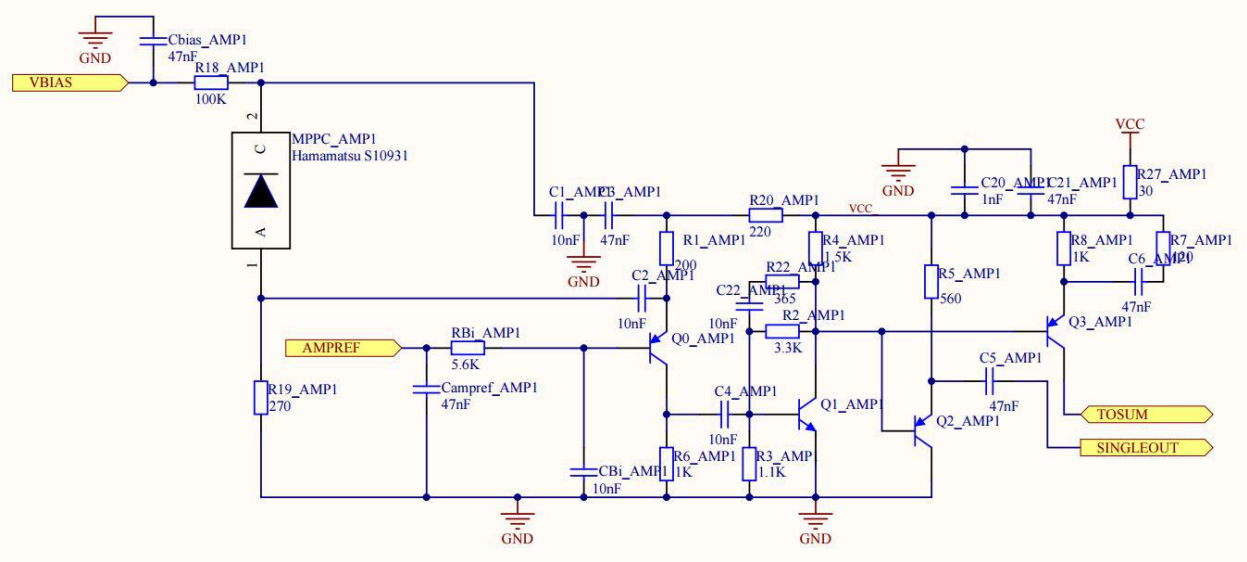

Figure 3.5: Amplifier schematic with the various nets labeled. The signal is generated by the SiPM and is amplified until it either goes to the individual readout or to the summing circuit.

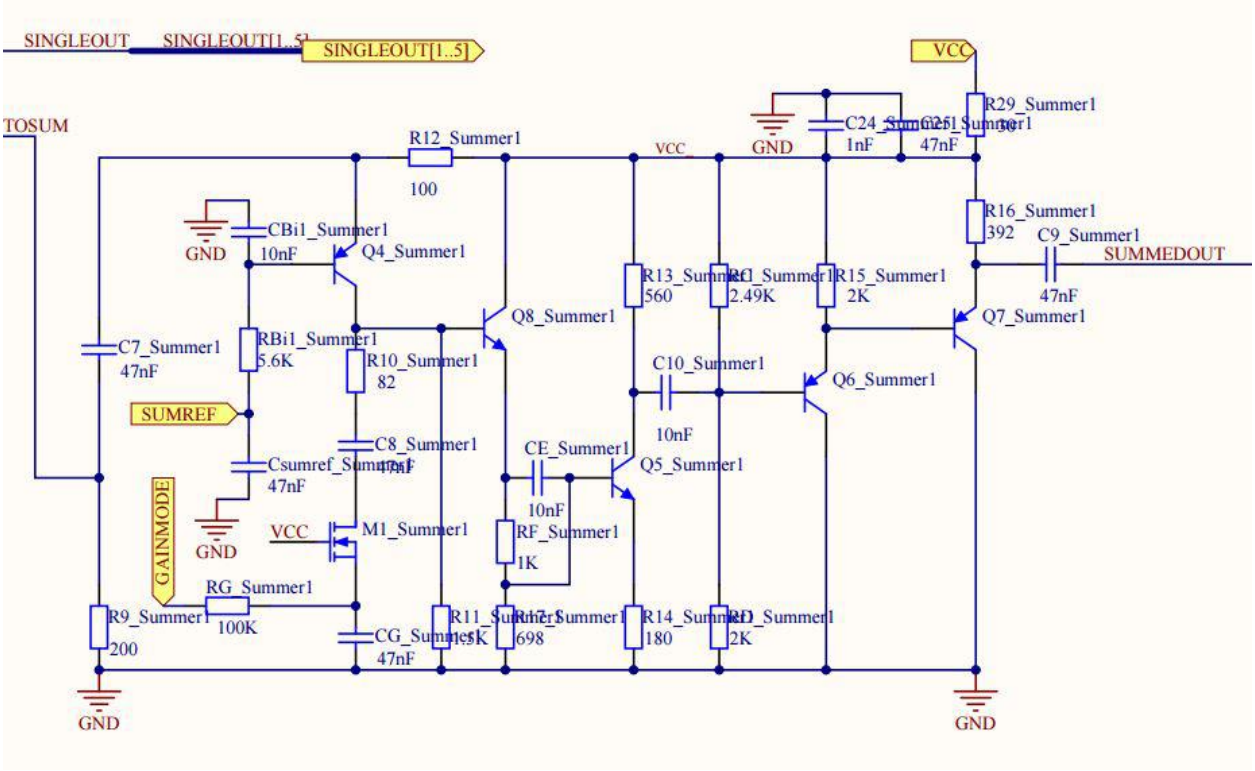

Figure 3.6: Summer schematic with the various nets labeled. The signals come from the 5 amplifier circuits and are combined here. The FET (labled M1) switches the summing circuit between high and low gain modes.

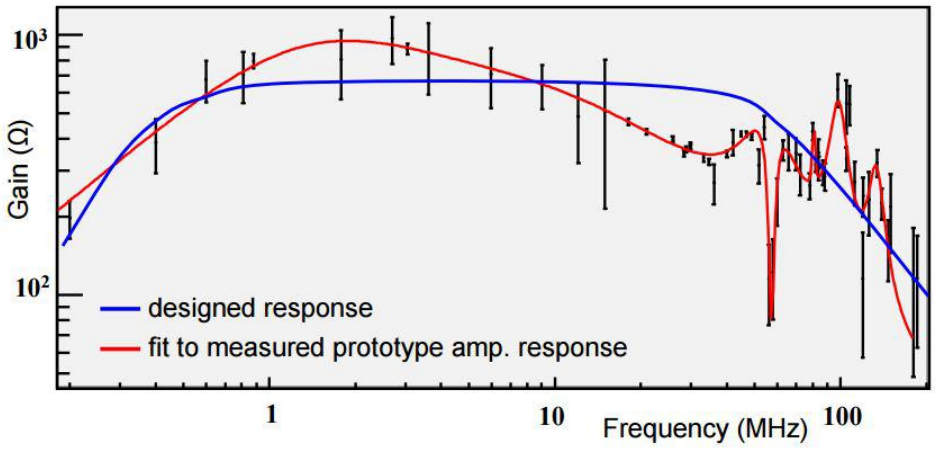

Figure 3.7: Initial preamplifier frequency response

collector which is roughly proportional to the gain of this stage. By "toggling" this switch, the summing circuit can change between two gain modes where "high" gain is used to see the single pixel peaks of the SiPMs. This creates a roughly 15x additional factor of amplification.

Fig. 3.7 shows the frequency response of the first prototype of the preamplifier in low-gain (operation) mode. A small sinusoidal current was injected directly into the input stage of the amplifier for these measurements. As seen in the figure, a significant deviation was observed from the designed response. There is a broad enhancement centered around 2 MHz and several resonances near 100 MHz.

I entered the group after this measurement was taken and was tasked with understanding why the preamplifier behaved in this way. Further iterations of the board solved these problems. The traces on the board were adjusted to avoid parasitic inductance, which, when modeled, showed resonances compatible with those measured. The higher gain at low frequency was a result of using a lower capacitor value than was optimal, resulting in higher impedance at lower frequencies.

In addition to improving the frequency response, I also provided many updates to the schematic and PCB layouts. Some components were deemed incompatible or were no longer available which required new parts to be reviewed and new footprints to be made for the

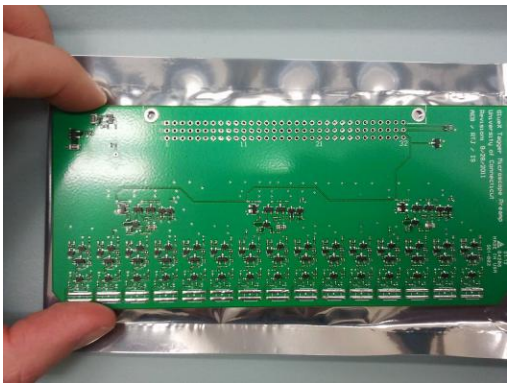

(a) Preamplifier version 2 before SiPMs

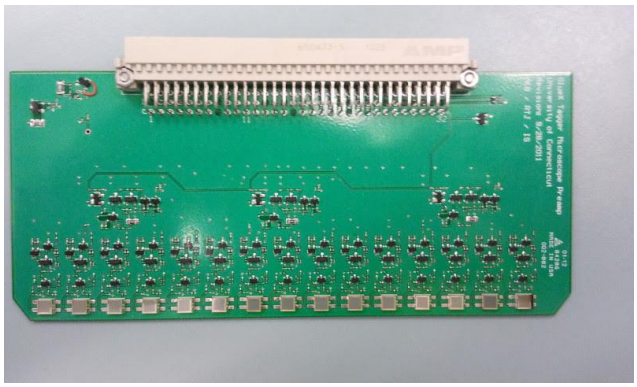

(b) Preamplifier version 2 after SiPMs

Figure 3.8: Preamplifier version 2 (a) before and (b) after attaching SiPMs. This was produced and populated by Sierra Circuits. The SiPMs and Eurocard connector were soldered by the author.

Figure 3.9: Soldering station with optical microscope used for attaching small surface mount components to the electronics boards.

schematic and PCBs. As the physical design of the microscope progressed, I adjusted the board sizes to meet the specifications.

The first prototype preamplifier that I created can be seen in Fig. 3.8. After the initial set of updates, I contacted multiple companies for quotes on on producing a couple prototype boards. We chose Sierra Circuits which populated the components on the board except for the Eurocard connector and the SiPMs as these need to be attached with precision and care. The setup used for attaching SiPMs and Eurocards can be seen in Fig. 3.9. A hot air machine was used to aid in soldering the SiPMs, and the smaller surface mount components required

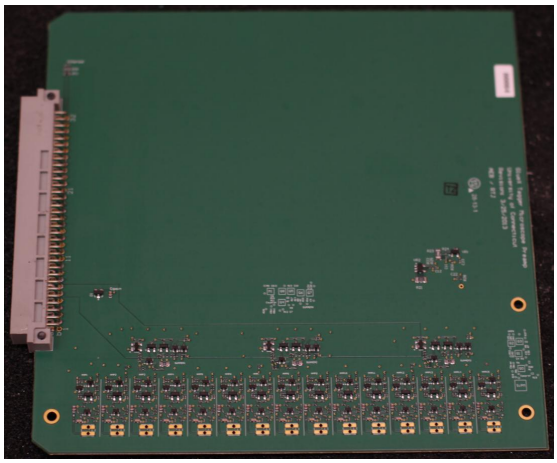

(a) Final production preamplifier board

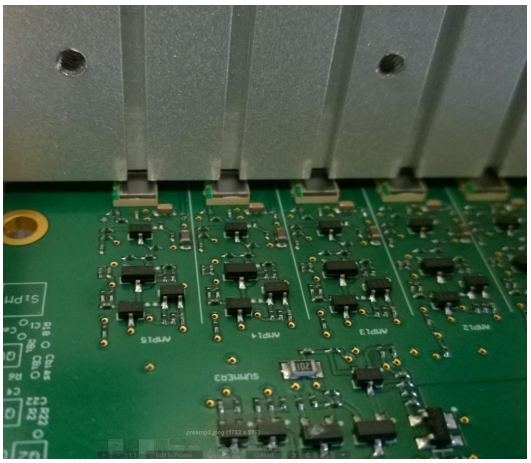

(b) The preamplifier in the metal chimney

Figure 3.10: (a) The final production preamplifier. The size was increased to meet physical design requirements and also to increase the effective area of the ground plane, which serves as both a shield from electronic noise and a heat sink. (b) shows a close up view of how the fibers line up with the SiPMs. The fibers are placed in the metal chimney grooves and stop 1 mm above the SiPM surface. A plate is attached to hold the fibers in place.

the use of an optical microscope. This second prototype performed better than the first but still required additional tweaks. As the schematics changed, I would swap components out to test the performance.

Once satisfied with the performance of the preamplifier, the final production boards were produced (Fig. 3.10). JLab procured the boards on our behalf and delivered them to us before the SiPMs were attached to verify that everything was in working order. A basic test of the DC operating points was performed which led to the discovery that the manufacturer used incorrect parts, most notably a voltage regulator (Fig. 3.11). Other components were found to be incorrect as well and these were replaced. The boards were shipped back to JLab to have their SiPMs mounted before being returned to UConn for further testing. All boards were tested in a full setup to ensure both the AC and DC signals worked properly.

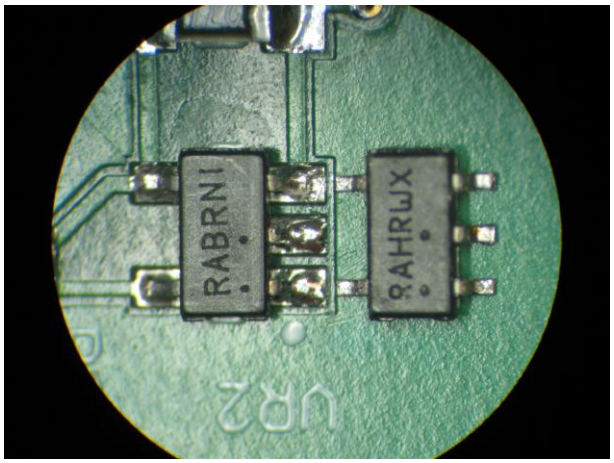

Figure 3.11: Discovered incorrect voltage regulator used on the board which did not match the Bill of Materials (BOM).

3.2.2 Control board

The purpose of the control board is to provide each SiPM with the proper voltage and to monitor various key voltages. It was found that the breakdown voltage for each SiPM is different, requiring that each of the 510 channels be individually adjustable. The gain and photo-detection efficiency of SiPMs also exhibit temperature dependence which can be compensated by online adjustment of their biases. In addition, the control board is able to switch the gain mode of the preamplifier between normal gain and high-gain operating modes.

Voltage monitoring of the electronics is important for evaluating the performance of the TAGM. Temperature monitoring is required as well since the SiPMs can be affected by temperature changes. There are three DC voltages that need to be monitored on the preamplifier: the supply voltage, and the base voltages for the input transistor on the amplifier and summing circuits. The supply voltage can be adjusted remotely, but the other two should remain within a strict range around a preset fixed point, otherwise a problem has occurred and the board needs to be repaired.

This board, like the others, sits in an area with high radiation levels. The monitoring must be done remotely from the counting house which requires some sort of communication

between the two locations. To achieve this, wired Ethernet communication was chosen since it is commonly used in experimental areas and is simple to integrate with existing infrastructure in the experimental hall. The communication design uses simple Ethernet packets addressed to each control board via the MAC address. To avoid cataloging the MAC address of each controller and cross-reference it with the energy bins it controls, a one-byte "geographical" address is hard-coded into the slot where the board is seated and is included in all communications. The monitoring software cross-references this to check the correspondence between the packet source address and the column/row number of the detector being queried.

Each SiPM requires approximately 70 V and so the control board has an integrated circuit which can handle multiple channels with this voltage level. It was decided that the Analog Devices AD5535 (and later the AD5535B) should be used. This is a 32-channel DAC ranging up to 200 V output which is more than sufficient for the SiPMs.

However, this device does not have a voltage readback. To address this deficiency, one channel is dedicated as a voltage-setting test line. It can be set to a specific value and then sampled by the ADC, described later, in the electronics health monitoring. Another line is dedicated to setting the amplifier gain. This leaves 30 channels available, which is just the number needed to drive 30 SiPMs, 6 columns of 5 each. This equates to two preamplifiers. Table 3.3 shows everything that the control board monitors.

For the health monitoring of the boards, the 16-channel Analog Devices AD7490 and Analog Devices AD7314 temperature sensor were selected. The latter measures the temperature of the control board while two channels of the ADC measure the voltage across a thermistor on the two connected preamplifier boards. Typical operating temperatures are 30-50 C, depending on the component.

The central controller for the board is a Field-Programmable Gate Array (FPGA) called the Xilinx Spartan 3A XC3S50A. This chip requests voltages and temperature readings,

Table 3.3: A table of all monitored values by the control board

Name	Description
+5 V	The +5 V power line
-5 V	The -5 V power line
+3.3 V	The +3.3 V power line
+1.2 V	The +1.2 V power line
Gainmode	The value associated with high or low gain in the preamplifier
Preamp 1 SumRef	Preamp 1's summing circuit reference voltage
Preamp 2 SumRef	Preamp 2's summing circuit reference voltage
DAChealth	A pre-determined value to monitor the health of the DAC
Chip Temperature	Temperature of the control board
DAC Temperature	Temperature of the DAC
Preamp 1 Temperature	Preamp 1's temperature
Preamp 2 Temperature	Preamp 2's temperature
Preamp bias voltages	All 30 SiPM bias voltages

drives the encoding of the DAC, and interfaces with the remote computer by reading and writing packets through the Ethernet Controller (EC).

At startup, the FPGA gates are programmed based on firmware loaded into non-volatile memory in another component. This decouples the programming and execution ICs. The FPGA is loaded using the Xilinx XCF01SVO20C EEPROM with the program itself synthesized on a computer written in Very-high-speed integrated circuits Hardware Description Language (VHDL). This language presents a model of the hardware as a parallel set of state machines and defines the behavior in a complete way.

The EC application notes advised a 20 MHz external digital clock, and the Intel Bus protocol between the EC and FPGA also required a timing structure with a clock of 20 MHz, which led to the selection of a FOX FXO-HC53 HCMOS 20 MHz clock IC to drive the board. The FPGA subdivided this to create a 5 MHz clock for the rest of the board components. The communication scheme between these components can be seen in Fig. 3.12.

Most of the control board design was finished when I arrived in the group. My task was to update the PCB traces and find replacements for various components that were no longer commercially available. This process also involved a significant amount of retracing

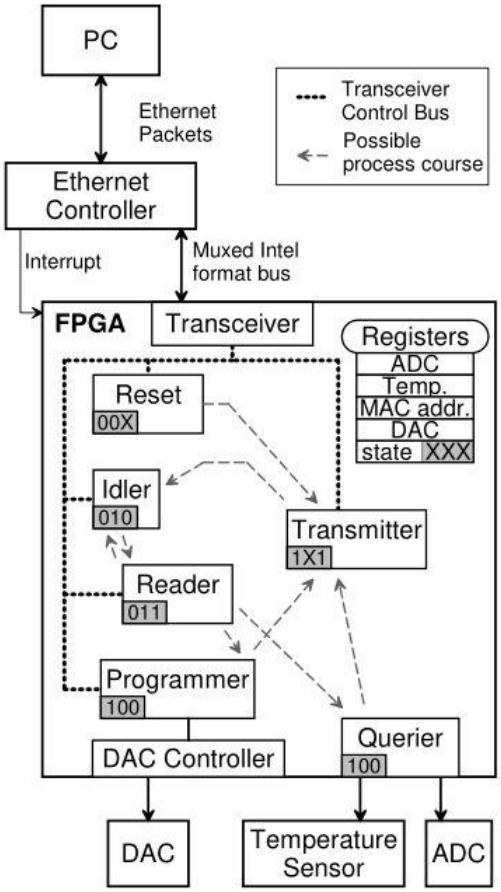

Figure 3.12: This diagram illustrates how the communication on the internal FPGA-transceiver control bus is orchestrated with a state register. The register codes serve as "chip enable" bits to prevent multiple drivers writing on the bus. Control is passed between modules by setting this code after completion to create the proper chain of events to enable Ethernet communication with the remote computer.

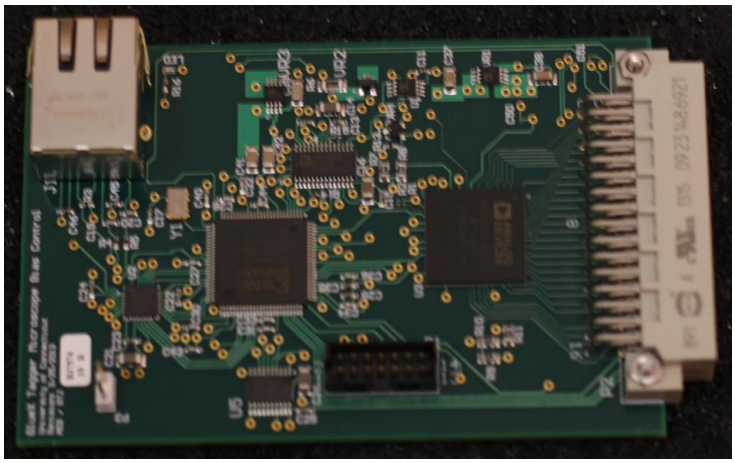

Figure 3.13: Final production control board. The Ethernet jack can be seen in the top left. The large black square in the middle is the FPGA while the large square on the right is the DAC.

connections between various components and generally cleaning up the layout. A final production control board can be seen in Fig. 3.13. Part of the performance test of the control board involved updating the FPGA firmware and successfully loading it onto the device. A mock preamplifier board was made to test that the desired SiPM biases were being applied correctly. All control boards were tested before being delivered to Jefferson Lab.

For use at Jefferson Lab, communication with the control board from the counting house is done using software written by Dr. Richard Jones called TAGMutilities. The commands that can be performed are: probeVbias, setVbias, readVbias, resetVbias, and TAGMremotectrl. In order to communicate with the TAGM in the hall, the frontend cards and the controlling computer must exist on the same Ethernet virtual local-area network (VLAN). A specific port on a specific server in the Hall D counting room was configured for this VLAN, and all communication between the control software and the TAGM control boards took place through this intermediate server. The executable TAGMremotectrl is run by this server and listens to a specified port for packets destined for the TAGM. This server then passes the packets on through the designated Ethernet port to the TAGM.

When turning on the power supplies, the command probeVbias is executed to check that all control boards have turned on. The FPGAs respond with their geographical address as well as their MAC address confirming that they are on and responding to commands.

The SiPM and monitored voltages can be read by the command readVbias. This requires specifying a particular control board which is then queried for the information before returning a print out of the various values. This is useful in debugging issues with the boards and allows the user to check that the proper bias voltages have been set.

Setting the bias voltages is done by setVbias which has many options to allow many different detector configurations. This command requires a configuration file which provides information on each SiPM/fiber regarding its threshold voltage as well as its gain and photon yield. The values in this configuration file are determined based on experimental data and will be explained in the next chapter.

3.2.3 Backplane

The backplane is the board which routes signals between the preamplifier and the control board. It also acts as a light-shield for the SiPMs located in the compartment behind it. The power cable is connected to these boards which distributes the power to the preamplifier and control boards. The backplane is also instrumented with LEMO connectors which attach to the readout cables.

My work involved expanding the size of the board to match the physical design specifications of the housing structure as well as creating the power cables. I redesigned the PCB from scratch due to a change in layout necessary for the final production. The final production backplane can be seen in Fig. 3.14, and Fig. 3.15 shows how the three electronics boards connect together.

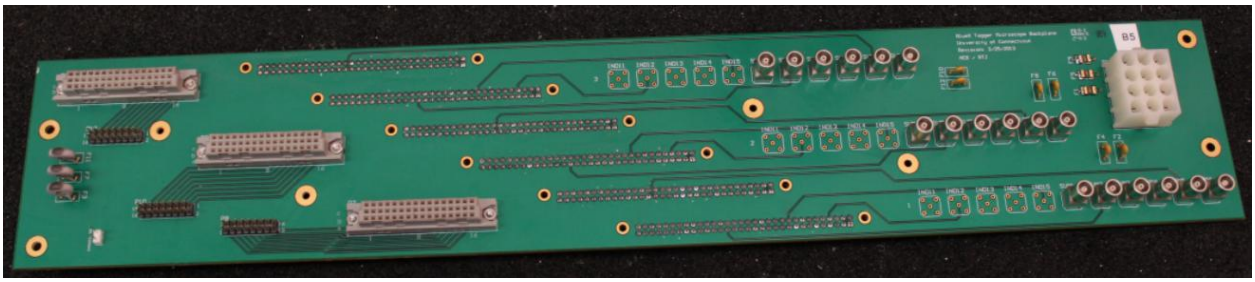

Figure 3.14: Final production backplane. Three gray connectors on the left are Eurocards which hold the control boards. The set of 3 black pins to their left with traces connected to the Eurocard and the geographical address jumpers. The six rows of pins are the underside of the preamplifier Eurocard connectors. The round silver pieces are the LEMO connectors which are connected with cables. The right white plastic piece is the housing for the power cable.

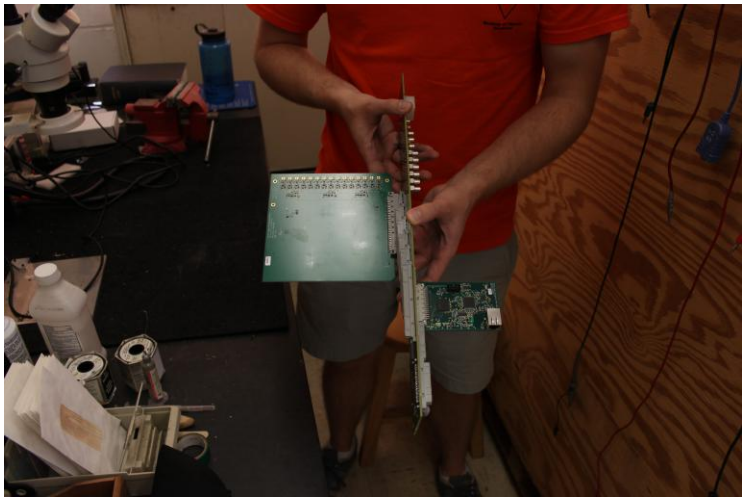

Figure 3.15: All electronics boards attached together

3.3 Fiber Bundles and Enclosure

The design and construction of the fibers, as well as the physical enclosure of the tagger microscope, are the work of fellow graduate student, James McIntyre. I made contributions to the construction of the fiber bundles and provided input on the enclosure based on the circuit board requirements. A large portion of the labor was conducted by laboratory technicians and undergraduate workers, primarily Ann Marie Carroll and Liana Hotte. Other undergraduate workers are listed in the acknowledgments section.

In this section, I will discuss the design and construction of the fiber bundles and the enclosure.

3.3.1 Design

As mentioned in 3.1, the desired size of scintillators are 2 x 2 x 20 mm^3 based on the width of the electron plane and the expected rate. The length was determined based on an optimization of the light-yield and cross-talk between counters due to electron-multiple scattering. Commercially available waveguides, Saint-Gobain BCF-98, were chosen to match the square scintillators. These were to have a double layer of cladding to prevent light loss. Each waveguide was cut to 166.6 cm.

Because of the size of the fibers, a set of 102 columns each of 5 fibers were created. This spans the energy range 8.1 to 9.2 GeV which is broad enough to contain the entire coherent peak as well as the flat region just beyond the peak to verify that the peak is well positioned.

The face of the fibers are placed along the focal plane of the electrons (Fig. 2.9). As the fibers progress along this plane, the angle between the focal plane and the incoming electron changes. This requires the orientation of the bundles to change progressively and is known as the β angle.

To keep the fibers along the focal plane, each set of 3 columns are offset from each other, as illustrated in Fig. 3.16. The β angle is accounted for by mounting 6 columns on one

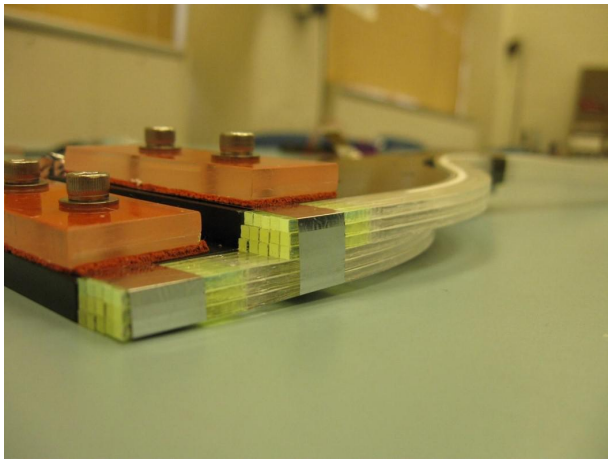

Figure 3.16: S-bend mounting block with fiber bundle. Every three columns must be shifted in order to stay along the focal plane. Each mounting block holds six columns of fibers. A shim is placed between each block to adjust for the β angle.

S-bend block and shimming each successive block so that the angle is correct. This led to creating fiber bundles of 30 fibers: 5 rows of 6 columns. This corresponds to 2 preamplifier boards.

The fibers are mounted as square blocks on the scintillator end, but the light guides fan out at the other end to line up with the SiPMs. A metal chimney was created with grooves to hold the fibers in place 1 mm above the SiPMs. This gap keeps the light cone from the fibers contained completely within the active area of the SiPMs, 3 x 3 mm^2. The fibers are held in the chimneys by a cover plate that is bolted down with a rubber gasket to protect the fibers 3.10b.

The path of the electrons dictated the shape of the fibers. Electrons interacting with the scintillator continue through and cause additional scattering and so the "S-bend" concept was created to bring the fibers out of the electron plane. Another concern was that the curvature of the fibers might cause them to arc upward into the plane of the electrons when they bend downward into the compartment containing the SiPMs. To help protect against this, a metal bar was placed along the fiber bundles to hold them down below the plane.

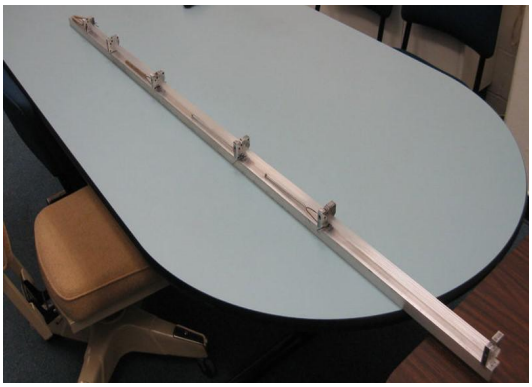

(a) Rail and collars for straightening fibers

(b) PVC pipe for straightening fibers

Figure 3.17: Fiber straightening setup. The fibers were held together by the collars in (a) and were placed inside the PVC pipe seen in (b). The tube was then filled with water and heated.

3.3.2 Fiber Construction

The construction of the fiber bundles proceeded as follows. The first step in the process was to make a rough cut of both the scintillators and waveguides. These fibers were then kept in a light-tight box to protect them from damage. When enough waveguides were cut, a bundle was bound together in collars, as seen in Fig. 3.17a, before being submerged into water in a PVC tube, as shown in Fig. 3.17b. The water was heated to 160° F to relax the fibers into a new, straight shape.

After the fibers had been straightened, they were taken to the machine shop where fellow graduate student, Brendan Pratt, end milled the fibers to the proper length (Fig. 3.18). Each bundle of 30 fibers was held in a mount and machined using a double-fluted end mill operating at 1400 rpm. This method reduced the cracking of the exterior cladding and produced a final finish on the fiber face which required minimal polishing. The waveguides remained in their collars during the process. The final length was 166.6 cm.

With the waveguides at their proper length, the ends needed to be polished to smooth the surface before fusing with the scintillators. The fusing setup can be seen in Fig. 3.19a. An intense light source heated the waveguides and scintillators within a small glass ferrule.

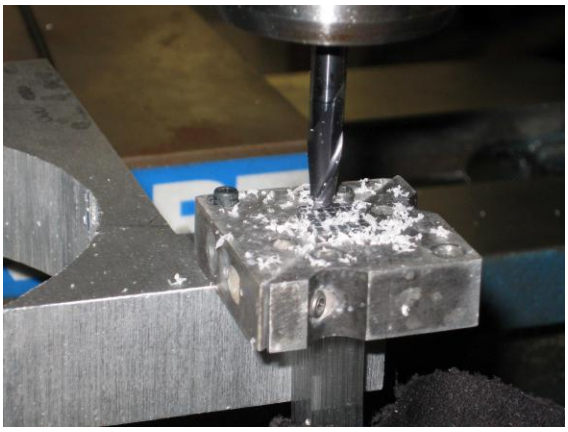

(a) End milling of the fibers

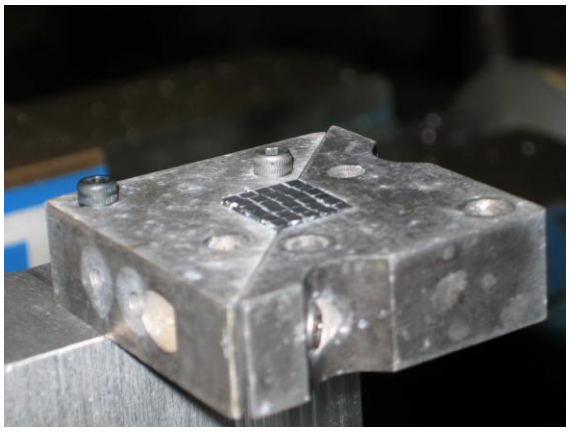

(b) Result of fiber end milling.

Figure 3.18: The fibers were brought to the physics department machine shop to be end milled. The process can be seen in (a) while the results can be seen in (b).

As the two pieces were being heated, both ends were gently pushed together. The result can be seen in Fig. 3.19b. After this step, the fibers were ready to be bent.

3.3.3 Initial Fiber Bending

The first method of bending the fibers into their proper shape involved multiple steps of heating the fibers in water. The first step was to straighten the fibers, taking out the natural arc that they acquired from the spool upon which they were shipped. A bundle of 30 fibers was made and placed in multiple collars to hold the fibers. These were then submerged into a PVC pipe filled with water. The water was heated and the fibers were allowed to relax into a new, straight, natural form.

To produce the proper S-bend and final arc, a metal jig was made (Fig. 3.20a). The scintillator ends of the fibers were placed into a metal mount (Fig. 3.20b)which had an additional piece that would push the fibers into place when bolted. The other end of the fibers were fanned out and placed in metal grooves corresponding to the spread required to line up with the electronics (Fig. 3.20c).

A large tank was constructed which would hold the bending unit and was filled with water. The tank was covered and everything was heated up to 160° F. At this point, the

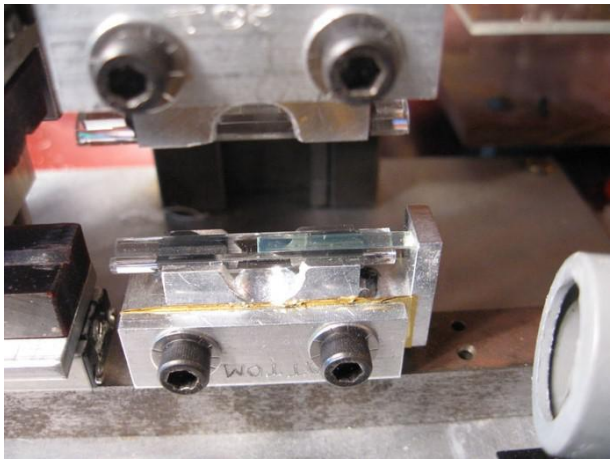

(a) Fusing setup

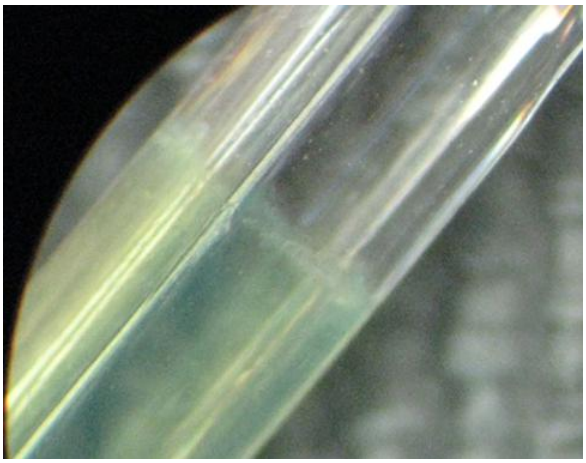

(b) Close up of scintillator-fiber joint

Figure 3.19: (a) The setup for fusing scintillators and fibers together. The scintillator and fiber are placed within a glass ferule and are heated by a lamp. As they are heated, pressure is applied to push the two pieces together. The results of the fusing can be seen in (b).

fibers were quickly removed and the fanned portion of the fibers were bent and bolted down to the guide rails before being re-submerged into the water to cool down. Fig. 3.21 shows multiple views of the fibers in the bending unit.

It was discovered after creating the first batch of 20 bundles (17 production + 3 spares), that the scintillation light output did not match expectations, which will be discussed in further detail in the section 3.4. Upon closer inspection, Ann Marie found that the company provided single-clad fibers instead of double-clad, see Fig.3.22[5]. At this point, less than half of the bundles had been painted. The thought was that the paint was changing the index of refraction and caused the light to escape rather than to internally reflect. Paint was removed from a few of the bundles and tested again. These fibers had even worse performance than before.

It was understood that the fibers had been handled too much and that the process of bending introduced defects which caused their performance to deteriorate. The initial set of fibers were delivered and installed as is with the idea that a new set of replacement bundles would be made. The installation of the intial set of fibers will be discussed in 4.

[5]I would like to thank members of the University of Connecticut's Institute for Material Science (IMS) for taking these measurements.

(a) S-bend bending unit

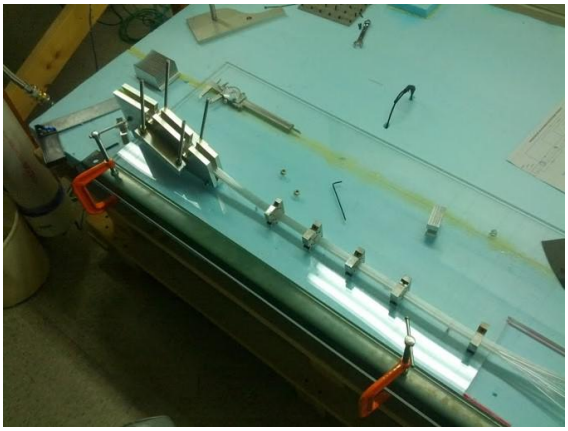

(b) Initial S-bend portion of bending unit

(c) Initial fiber bending unit

Figure 3.20: Bending unit, pre-bend. (a) shows the setup for the S-bend part of the fibers. They are placed within the metal jig with the fibers secured in the collars. In (b), the ends of the fibers are placed in metal grooves located on two separate plates.

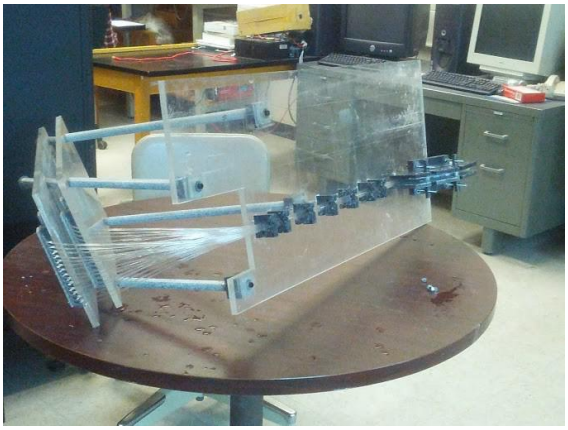

Figure 3.21: Initial bending unit, post-bend.

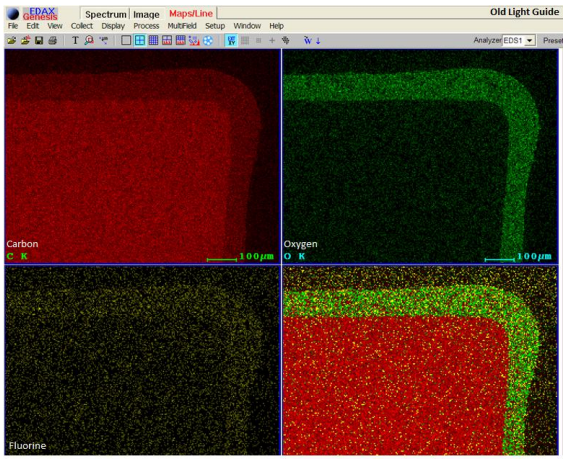

(a) EDX measurement of old fibers

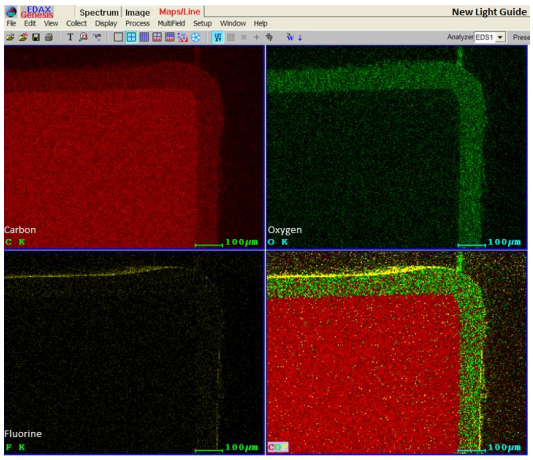

(b) EDX measurement of new fibers

Figure 3.22: Proof of double cladding. (a) Old fibers, no yellow band which indicates a lack of fluor-acrylic. (b) New fibers, yellow band from the second layer containing fluor-acrylic.

3.3.4 Final Fiber Bending

After observing the performance of the initial set of fibers, James McIntyre developed an entirely new procedure for shaping the fiber bundles. A detailed description of this work will be given in his thesis. The main fabrication goal was to produce fibers with minimal heating-cooling cycles and manual handling.

One adjustment was to remove the step of initially straightening the fibers. Because the waveguides have a natural curvature from the spool, it was determined that this would be sufficient for the 135 ^{o}F bend into the lower enclosure. The metal bar would still be used to hold the light-guide fibers down out of the electron plane.

Another adjustment was to no longer use water. It was determined that the water introduced mineral deposits that deteriorated the cladding and made it separate from the core. Instead, the crucial S-bend would be created using hot air. An insulated enclosure that could hold the full fiber bundles was created, that contained a heating pad and fans to circulate hot air throughout the tank.

The fibers were collared and sealed within the enclosure, and the air temperature inside the box was slowly raised to about 75 ^{o}C. A new metal block surrounded the S-bend region

which had bolts that stuck through the enclosure. Once the desired temperature was reached, the bolts were tightened down, squeezing the two halves of the bending unit together and bending the fibers into the proper shape. All of this was done without ever opening the lid, as it was suspected that the shock of the temperature difference between the water and the room air caused crazing of the fibers.

This method produced fibers meeting the design specifications for photon-yield. The installation of these fibers is discussed in Ch. 4.

3.4 Quality Assurance

Before delivering the microscope to Jefferson Lab, proper quality assurance (QA) tests were needed to verify that the performance meets the design specifications. These tests were performed by myself, Ann Marie, Liana Hotte, and the undergraduates. Unfortunately, the first batch of fibers were produced before the QA setup was finalized, too late to allow for substantial changes to the fabrication procedures that had degraded the performance of the fibers. This section will explain our testing box, the data acquisition system (DAQ), and the results of these tests.

3.4.1 Dark Box

A means of testing the produced fiber bundles was required and so a dark box was constructed by James McIntyre. The design can be seen in Fig. 3.23a and the final construction in Fig. 3.23b. For simplicity, only a single fiber bundle could be tested at a time. A bundle was placed inside along the wooden slope with the scintillator end mounted near the left side of the enclosure in Fig. 3.23b. The other end of the bundle comes up over the top of the sloping support and then descends vertically down into the chimneys holding two preamplifier boards. The inside of the dark box was painted black in order to reduce light reflections. Additionally, a dense foam was placed around the openings, which when compressed by the

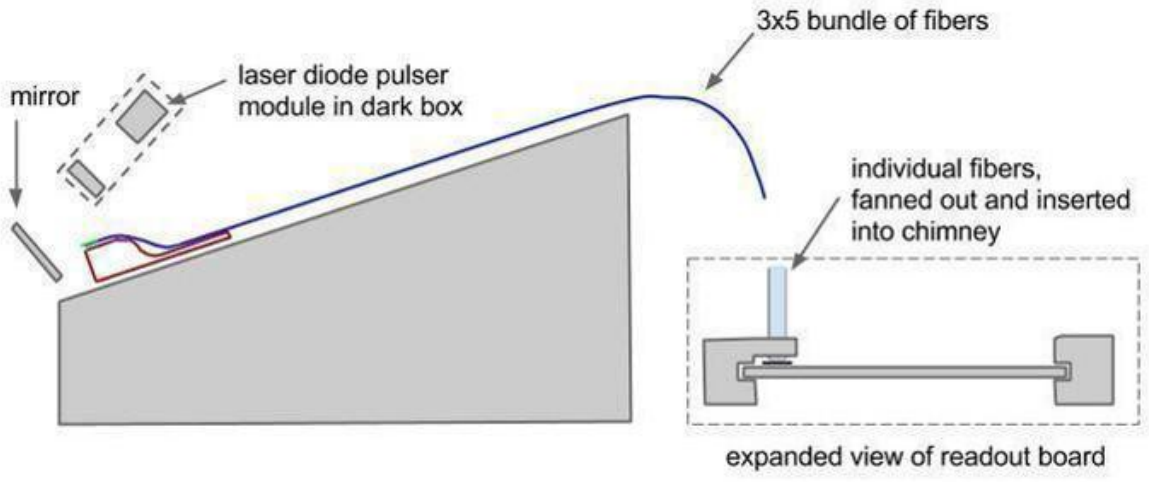

(a) Testing dark box diagram

(b) Opened dark box

Figure 3.23: (a) A diagram depicting the QA testing setup using a light-sealed box with a laser diode as a signal source for the scintillators. (b) The physical dark box used for QA testing. The scintillators are placed in the middle above the gray box. The fibers travel up the wood and curve down on the right side into the chimneys housing two preamplifiers (not seen in image).

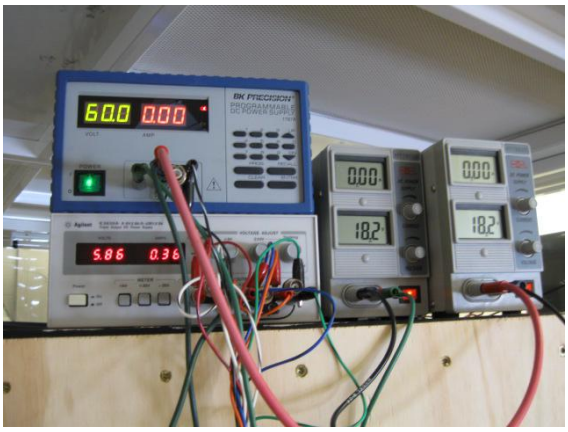

(a) Dark box power supplies

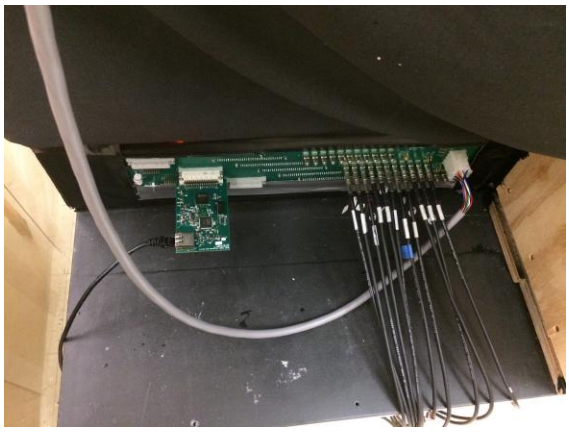

(b) Dark box electronics

Figure 3.24: (a) Power supplies necessary for the various control board and preamplifier voltages. (b) The backplane and control board are mounted into the back of the dark box.

latches, sealed the box and made it light-tight. The light-tightness of the dark box was tested by placing a digital camera inside with a 60 s exposure time.

A collection of benchtop power supplies was assembled to conduct the dark box light yield testing (Fig. 3.24a). These were placed on top of the dark box and were connected to the backplane immediately below them, as seen in Fig. 3.24b. The readouts from the backplane were brought underneath the dark box and connected into the fADC in the data acquisition system. An Ethernet cable connected a single control board to a standard network switch, which allowed for communication with the control board from any machine in the lab. For these studies, it was useful to run a remote script which would bias each SiPM individually in order to extract their individual pulse spectra.

In order to produce signals in the electronics, I built a small circuit (Fig. 3.25a) which produces a repeating, fast signal to be used to power a laser diode. This laser diode was used to mimic the electron beam and was mounted inside of the dark box, as seen in Fig. 3.25b. A diffuser was placed in front of the laser diode in order to disperse the light uniformly over the scintillator faces. An inner curtain separated the SiPMs from the laser diode to prevent background light from mixing with the fiber signals.

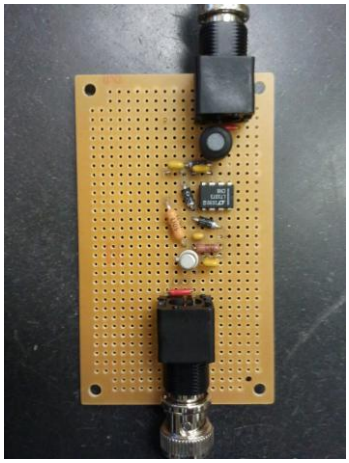

(a) Pulser circuit for dark box QA

(b) Laser diode for dark box QA

Figure 3.25: (a) A circuit created to produce a repeating, fast signal used to power a laser diode. (b) The laser diode mounted in the dark box to act as a source for the fibers and SiPMs. The tips of the scintillating fibers can be seen at the bottom of the image.

Table 3.4: UConn VME crate modules

Board	Slot	Description
CPU	1	Linux host for data collection
TI	2	Trigger Interface
fADC250	5	Flash Analog-To-Digital Converter
SDC	9	Signal Distribution Card
LED	14	Leading Edge Discriminator
F1TDC	16	Time-To-Digital Converter

3.4.2 Data Acquisition

Jefferson Lab loaned us a Versa Module Europa (VME) crate so that we could test the microscope at UConn. The VME crate provides a VMEbus standard to connect modules via Eurocard connectors and distribute signals between each module. A list of the modules used can be found in table 3.4

Fig. 3.26a shows the DAQ setup used for fiber quality assurance testing. The CPU module is the one that provides interaction with the crate and allows for data collection. This module runs a limited version of Linux which includes JLab software called CEBAF Online Data Acquisition (CODA), seen in Fig. 3.26b, which provides an graphical user interface (GUI) for collecting data. The output signals from the TAGM are connected to the

fADC module and the signal from the laser diode is fed back through a photo-diode is used as a trigger input. The output from the discriminator is connected to the Trigger Interface (TI) which tells CODA that a trigger was observed. The TDC was not used for our testing. The Signal Distribution Card provides trigger and clock information to the fADC.

3.4.3 Photon Yield

An initial test of the setup involved measuring the optical cross-talk between channels. It is important that signals from the pulser or from other fibers are not producing signals in the wrong SiPMs. To test this, a single fiber was installed and all of the SiPMs were turned on. The results can be seen in Fig. 3.27. It is clear that only a single channel observed light from a fiber. All of the other channels produced signals that were consistent with electronic noise (pedestal). This proved that there was no measurable optical or electronic cross-talk between channels.

After the first batch of bundles was bent, the QA performance testing began. At this stage, some of the bundles had already been painted but there existed fibers from all stages of production. Fig. 3.28a shows the pulser light yield distribution from a fiber which was bent in the hot water tank, while Fig. 3.28b shows the signal from a fiber which was painted. The bent fiber signal corresponds to a yield of 50 pixels per pulse and the painted fiber corresponds to 15 pixels per pulse. This showed a large variation in fiber performance but only provided a relative estimate for the fiber performance.

It was determined that painting, as well as removing the paint, caused significant reduction in performance. However, it was also noted that not all of the unpainted fibers had the same yield. There was a large variation in performance across all fibers that remained even after the painted fibers were set aside. It was suspected that our bending process caused damage to the fibers. One likely source of damage was the removal of the fibers from the hot water in order to bend them. The water was kept at 160° F while the room was 68°

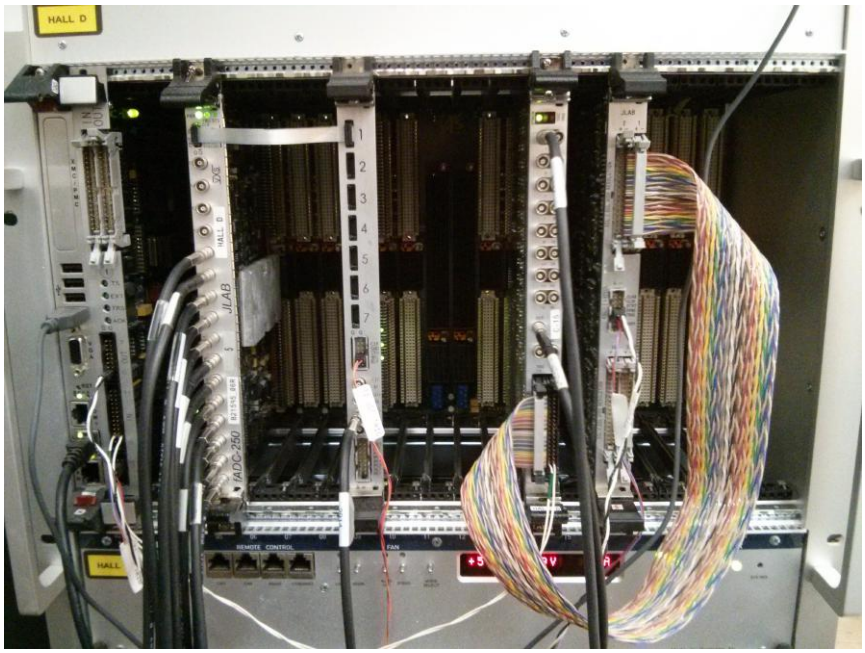

(a) DAQ used for QA tests at UConn

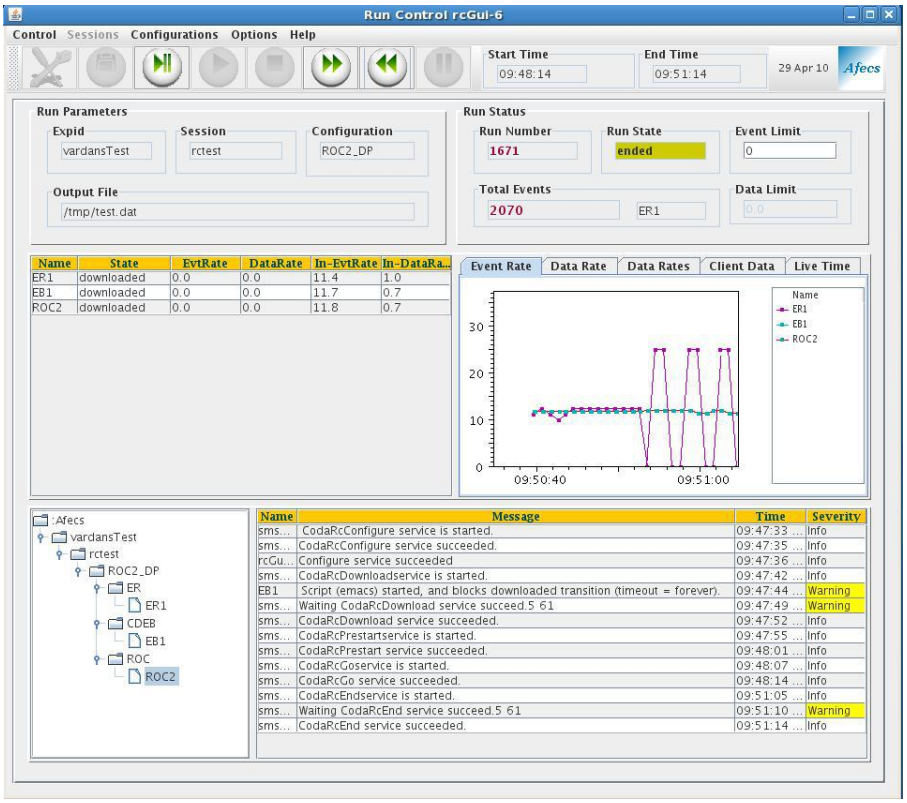

(b) Screenshot of CODA DAQ program

Figure 3.26: UConn data acquisition system and software

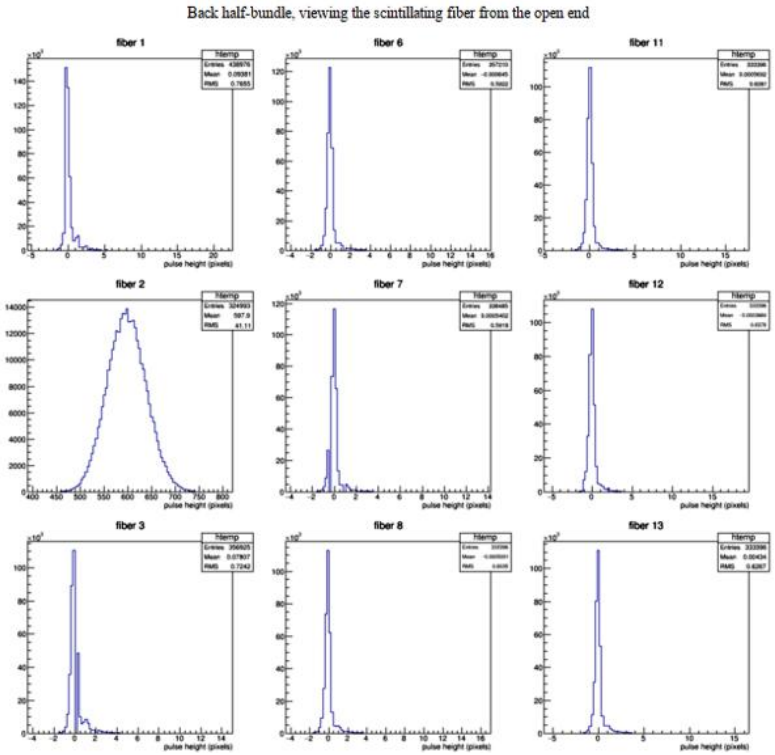

Figure 3.27: Optical cross-talk during QA tests, with a single fiber feeding SiPM 2, and all SiPMs biased. The x-axis is the pulse height in ADC counts. Only a single channel showed signal, all others contained electronic pedestal noise.

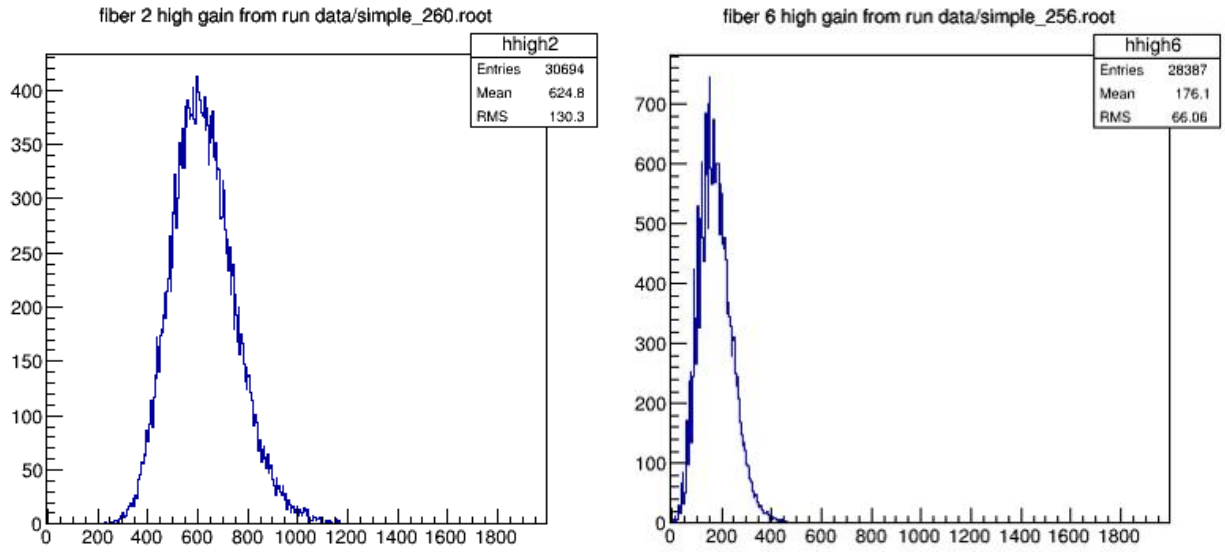

(a) Signal from a first batch bent fiber.

(b) Signal from a painted fiber.

Figure 3.28: Initial fiber yields. The x-axes are the pulse heights in ADC counts (a) The average pulse height from a bent fiber from the first set of fiber bundles. (b) The pulse spectrum for a painted fiber from the initial set of fiber bundles. This showed that painting the fibers caused a decrease in the photon yield.

F. The rapid cool-down was suspected of causing crazing in the fibers which reduced their performance.

The results of the new method of bending, where the fibers are kept in hot air with minimal interactions, proved to be much better. The spread in the light yields measured in the dark box for these new bundles was less than 10%, from which we concluded that we are now limited by the properties of the fibers themselves. Results from beam data will be shown in Ch. 4.

CHAPTER 4

Tagger Microscope Installation and Calibration

4.1 Installation

In the summer of 2014, I moved to Newport News, VA to become the local tagger microscope expert at Jefferson Lab. The microscope body was partly assembled at UConn, and the fibers were shipped separately. Upon arrival, the full detector was assembled.

It was understood that there was a large variation in light yield from the fiber bundles, which had been attributed to the initial fiber bending process. Because of this, the highest light yield bundles were placed at the upstream end where the polarization peak would be located. The remaining bundles were placed in descending order of overall light yield. The assembly of the TAGM can be seen in Fig. 4.1 and was a joint effort between Brendan Pratt, Jim McIntyre, and myself.

The assembly of the microscope took a couple days as we put the various pieces together. All of the metal brackets holding the preamplifiers in position needed to be installed and the upper enclosure rails needed to be set up. Installing a fiber bundle required matching the end of the fiber bundle to the proper SiPM location. This was verified by checking its position in the fiber bundle to confirm that the identification label was correct. The ends of the fibers in the chimney needed to be pushed past their proper location and were then guided into place so that all ends were at the same position and in line with the bottom edge of the chimney. This guaranteed the proper gap between the SiPM and fiber.

Once the fiber ends were in position, the S-bend was placed in the guide rails. The S-bend has two rods on the bottom that each go into a separate rail system which allows the block to be slid across the top. The upstream end has a reference edge which fixes the offset and β angle. Each successive S-bend block is shimmed by a small amount to keep the axes of the fibers parallel to the local electron rays along the focal plane.

Figure 4.1: Initial installation of the TAGM fibers. (left) I inserted the fiber ends into the metal chimneys and tightened the metal plate to secure them. (right) The bundles are installed and the shielding is in place.

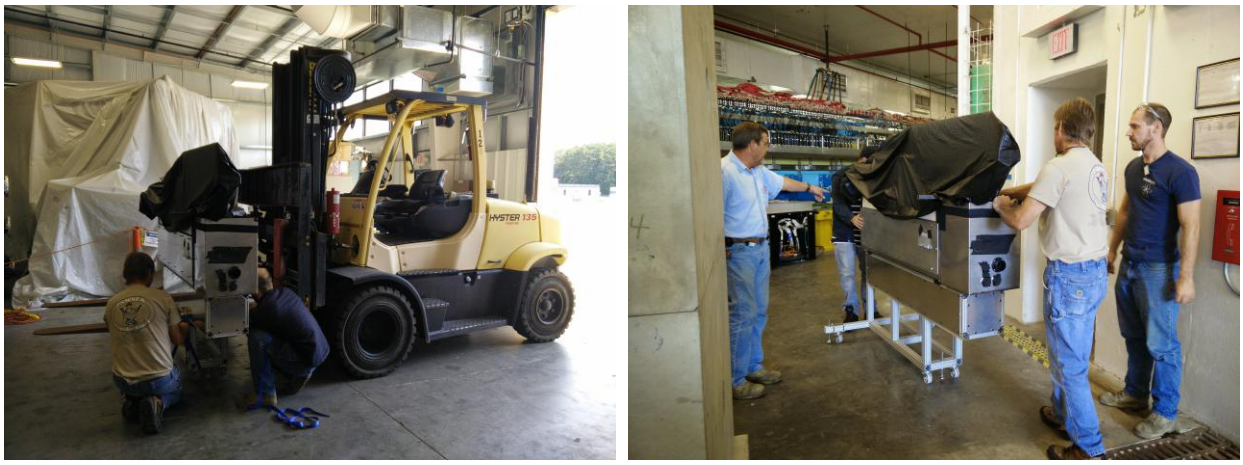

Figure 4.2: Moving the TAGM from the staging area to the tagger hall with the help of JLab staff.

After completing the assembly of the microscope, the detector was moved into the tagger hall with the help of the technical staff, as shown in Fig. 4.2. It was placed in roughly the correct location. The Survey and Alignment group came and added fiducial blocks to various locations on the TAGM to be used as alignment markers. These locations were placed at known positions which were correlated to the position of the fibers. This alignment put the microscope in a very good starting position but additional alignment adjustments finalized the positioning. The final positioning is accomplished with actuator motors underneath the plate that holds the fibers. The motors comprise a 3-point support for the fiber assembly which adjusts their height and two tilt angles to align the central row of fibers with the mid-plane of the tagger magnet gap. All aspects of the alignment are discussed in more detail in section 4.3.

With the microscope in place, all 120 (100 summed, 20 individual) readout cables, 6 power cables, 1 Ethernet cable, and 3 network switch power adapters were installed. Initially, only 120 cables were provided and so the last two columns were not instrumented. This was changed for the fall 2016 run which included the final two columns. In order to prevent light leakage, external cables were piped through plastic tubes which were bent and twisted to help prevent light from passing into the inner compartments. The path for the cables can be seen in Fig. 4.3. The upstream side of the microscope is a labyrinth compartment (Figs. 4.3a - 4.3b) which has connections for the cables as well as the alignment motor power cables. Once the cables were fed through the tubes (Fig. 4.4a), they were connected to their respective backplane or network switch, see Fig. 4.4b.

A shroud was used to cover the fibers and light seal the detector. It is Thor Labs BK5 black rubberized fabric. During the initial power tests, I discovered that this was not a light-tight shroud. However, adding a second layer was sufficient for our needs. Additionally, radiation shielding was added in multiple locations to protect the SiPMs from radiation damage, particularly from neutrons. Between each fan of 15 fibers, polyethylene blocks were

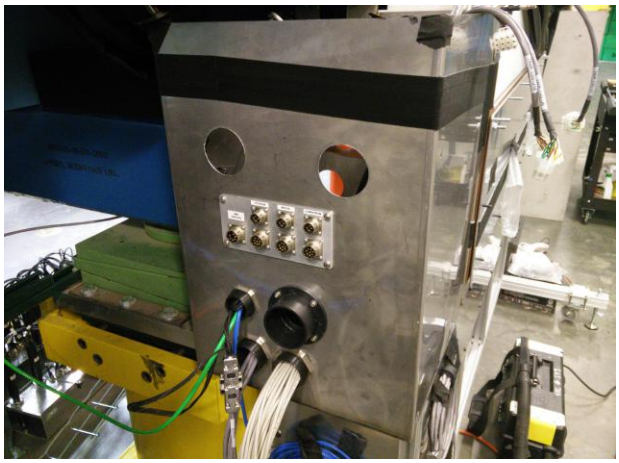

(a) Upstream view of the TAGM, pre-install

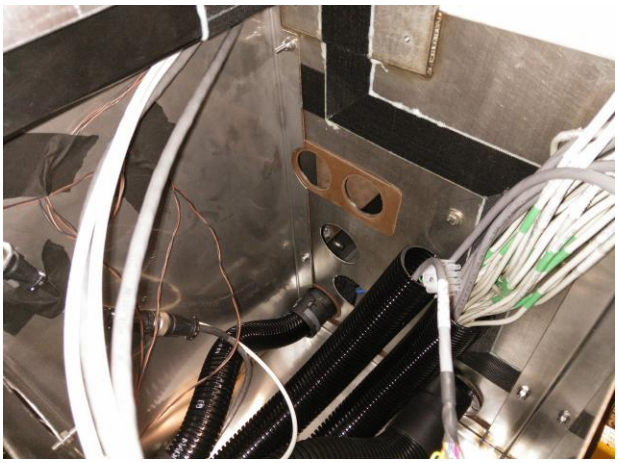

(b) View of upstream compartment, pre-install

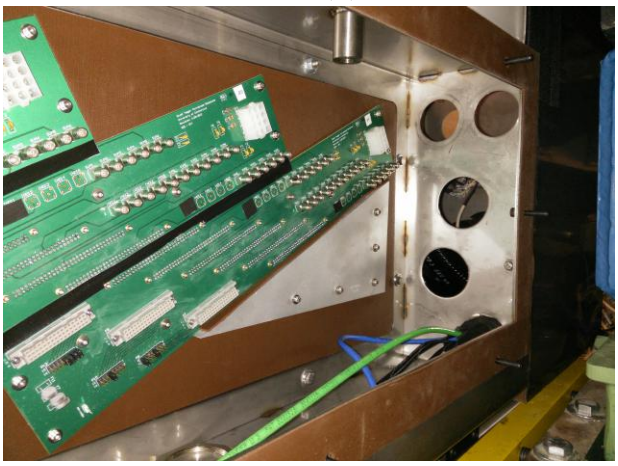

(c) View of backplanes, pre-install

Figure 4.3: A view of the microscope before the installation of cables. (a) The upstream compartment is the access point for the cables and motor controls for the TAGM. (b) Inside the upstream compartment, tubes containing the cables are bent to prevent light leakage, and the compartment is filled with plastic shielding. (c) The control board compartment has openings for the power and readout cables.

(a) View of upstream labyrinth, cables installed

(b) View of backplanes, cables installed

Figure 4.4: (a) The full set of cables have been fed through plastic tubes and bent to prevent light leakage. (b) The cables are connected to the backplanes and sit on a cable tray above the control boards.

placed (Fig. 4.5b). The front compartment was filled with small beads of polyethylene as were the surrounding bags (Fig. 4.5).

4.2 Software

Before describing the various calibrations, a basic overview of the software structure used by the GlueX experiment is presented. The majority of the code is located in a git repository called "sim-recon" accessible to members of the collaboration and is written mostly in C++. In this code are libraries which take hardware level objects, like "Df250PulsePedestal," and builds them into high level ones, like "DBeamPhoton." Additionally, this code provides a kinematic fitter when reconstructing the data as well as libraries necessary for physics analyses. At the base level, all of the objects are related to specific hardware components like the fADCs (both 125 and 250 MHz versions) and TDCs. These objects are detector agnostic and therefore must be parsed to provide detector specific objects. In the next subsections, the various TAGM specific, hardware-level objects used in the calibrations are described.

(a) Upstream compartment shielding

(b) Shielding blocks between fibers.

(c) Shielding bags around the TAGM

Figure 4.5: Shielding for the TAGM. (a) The upstream compartment is filled with small polyethylene beads to protect the electronics from upstream radiation. (b) A block of polyethylene shielding is placed between each set of 15 fibers. (c) Bags filled with polyethylene beads are stacked surrounding the TAGM at the height of the electronics to reduce radiation damage.

Table 4.1: DTAGMDigiHit object members.

Member	Description	Type
row	TAGM row 0-5, where 0 means summed output	int
column	TAGM column number	int
pulse_integral	The integral of the pulse	uint32_t
pulse_time	The time of the pulse	uint32_t
pedestal	Pedestal (baseline) value	uint32_t
QF	Quality factor of the data entry	uint32_t
nsamples_pedestal	The number of samples used in the pedestal	uint32_t
nsamples_integral	The number of samples used in the integral	uint32_t
pulse_peak	Pulse amplitude	uint32_t
datasource	Indicates version of the firmware	uint32_t

4.2.1 DTAGMDigiHit

Data from the TAGM fADC are used to create objects called DTAGMDigiHits. The "D" prefix indicates that the object is a Hall D specific object. The members of this class are listed in Table 4.1.

For the pulse_integral and pulse_peak, the baseline is included in the value and must be subtracted properly. The standard baseline for all GlueX detectors is a value of 100 fADC counts where the fADC ranges from 0 to 4095 counts. The member pedestal contains the actual value measured by the fADC for the baseline. For both the integral and pedestal members, the fADC uses a specific number of samples to determine the value, in this case nsamples_integral and nsamples_pedestal, respectively.

4.2.2 DTAGMTDCDigiHit

Data from the TAGM TDC are used to create objects called DTAGMTDCDigiHits. The members of this class are listed in Table 4.2.

For all other detectors, the usefulness of the TAGM comes from the timing and location of the hit. The TDC provides a better time resolution than the fADC but does not contain any pulse information. It is for that reason that the fADC is used to understand the signals from the TAGM and the TDC is matched to provide the best time information.

Table 4.2: DTAGMTDCDigiHit object members.

Member	Description	Type
row	TAGM row 0-5, where 0 means summed output	int
column	TAGM column number	int
time	The time of the threshold crossing	uint32_t

Table 4.3: DTAGMHit object members.

Member	Description	Type
E	Energy associated with the column	double
t	Final time associated with the hit	double
row	TAGM row 0-5, where 0 means summed output	int
column	TAGM column number	int
integral	The integral of the pulse, pedestal subtracted	double
pulse_peak	Pulse amplitude, pedestal subtracted	double
time_tdc	The time from the TDC	double
time_fadc	The time from the fADC	double
npix_fadc	Pulse integral converted to pixels	double
has_TDC	Check if the hit has TDC information	bool
has_fADC	Check if the hit has fADC information	bool

4.2.3 DTAGMHit

Data from the DTAGMDigiHit and DTAGMTDCDigiHit objects are used to create DTAGMHit objects. The members of this class are listed in Table 4.3.

DTAGMHit objects are created so long as there is either fADC or TDC information. The fADC information is checked first and it is here that the pedestal is subtracted from both the integral and from the amplitude. The raw time from the fADC is converted from counts into nanoseconds using a conversion specific to the fADC 250 MHz module. If no TDC information is present, the time t is the fADC time. The energy E indicates the mean tagged photon energy associated with the tagger channel, derived from the column associated with the hit and the energy of the electrons from the accelerator. This is explained further in section 4.2.4.

If the TDC is present in the data, its information is merged with the fADC hit information, or a new hit is created if the fADC is not present. The member time_tdc is the raw

TDC time converted into nanoseconds but prior to any timewalk corrections. The final time t, when a TDC is present, is the calibrated TDC time with the timewalk corrected applied. This correction is explained further in section 4.4.

4.2.4 Calibration Database

A MySQL database is used to store the various constants necessary for calibrating the various detectors. It also provides a history of previous constants in case revision of the constants is required. When working on calibrations, it is useful to create an SQLite version of the database to test new constants before submitting them to the MySQL database.

4.3 Alignment

As mentioned in Ch. 3, the microscope electronics are capable of reading out the individual signals from each SiPM but only four columns have been fully instrumented this way. These columns are 9, 27, 81 and 99, where column 1 is the upstream-most and highest photon energy bin. The ability to read out these fibers individually allows for active monitoring of the alignment along the electron plane. By placing two readouts at either end, a sample over the entire microscope is obtained and is sufficient, given that the electrons intersect the focal plane along a straight line.

The most basic alignment initially comes from the Survey and Alignment group when installing the detector. There are five fiducial blocks attached across the microscope which provide reference points for the fibers. Fig. 4.6 details where these fiducials are placed. The fiducials are placed on the rail system that supports the fibers. The entire rail system is above the motors which allows for small adjustments to be made without having to move the entire detector. Additionally, the location of the fibers relative to the blocks has been determined with sub-millimeter precision so that Survey and Alignment are able to report the position of the fibers. Using a laser surveying system, they detect each of these reference

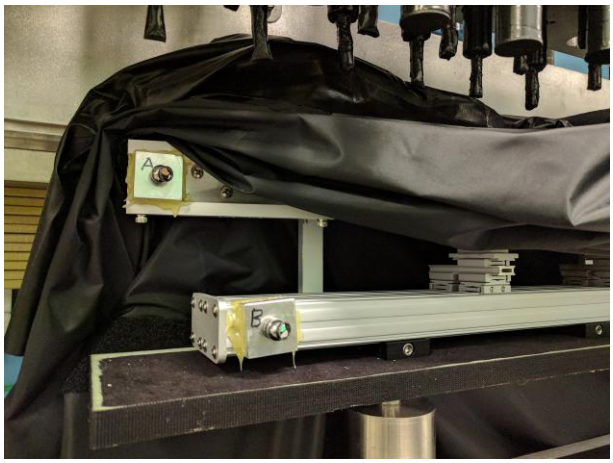

(a) Fiducials A and B with alignment ball

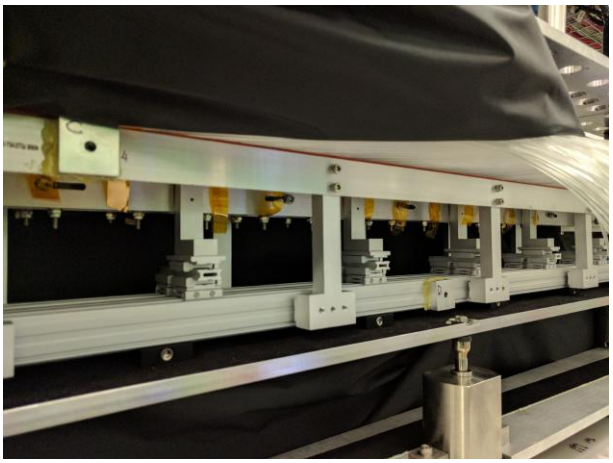

(b) Fiducials C and D in the center of the TAGM

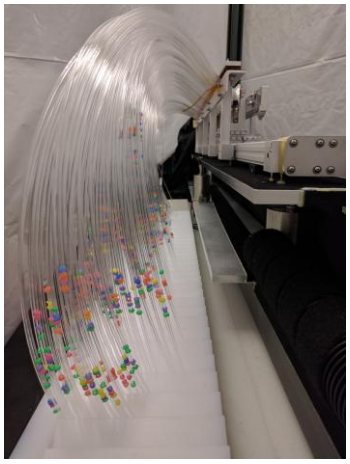

(c) Fiducial E on downstream end

Figure 4.6: (a) The fiducials A and B on the upstream end of the TAGM with marker balls for the survey laser. These are located at the end of the top and bottom rail. (b) Fiducials C and D are located in the central region. C is located along the top rail on the left, and D is located on the lower rail above the motor. (c) The last fiducial, E, is located at the downstream end at the very end of the guide rails.

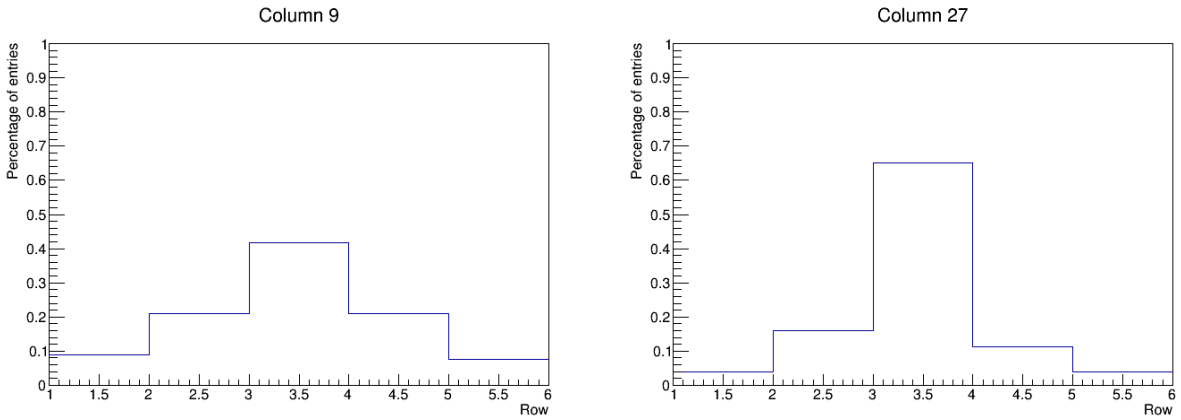

(a) Column 9 initial alignment

(b) Column 27 initial alignment

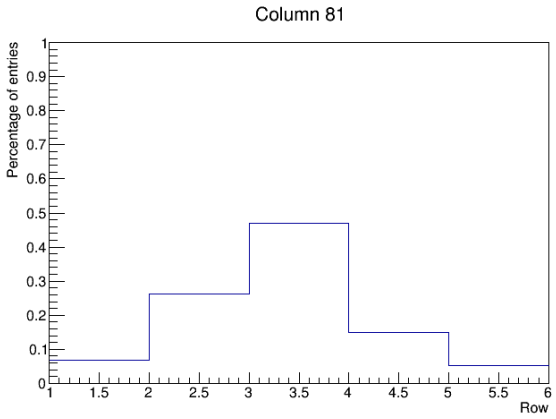

(c) Column 81 initial alignment

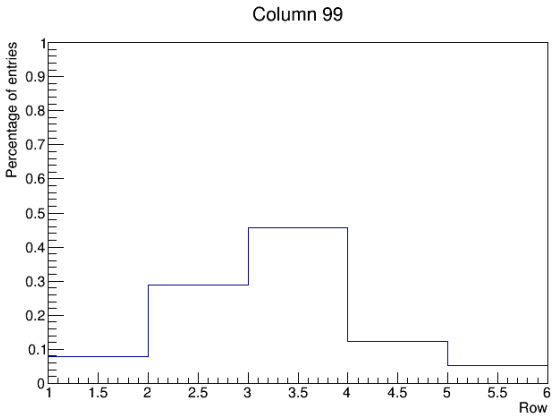

(d) Column 99 initial alignment

Figure 4.7: Initial vertical alignment of the TAGM. The y-axis shows the percentage of hits seen by a given row. All hits seen by the TAGM are included.

fiducials and determine their coordinates within the coordinate system of the hall. This provides a rough alignment of the fibers along the electron plane. Depending on how the beam is steered, the fibers may or may not be aligned properly.

Once the TAGM was sealed and beam was delivered, the next step in the alignment was performed. To measure the vertical alignment of the fibers, the number of photons detected for each fiber was examined. This was done using either scaler rates from the discriminator or from looking at the occupancy plots for the entire run. Because this measurement does not depend on the pulse height, the performance of individual fibers is not important. Fig. 4.7 illustrates the distribution across all the rows for each set of individual readout columns. Ideally, the distribution is centered about the central row with no events in the edge rows.

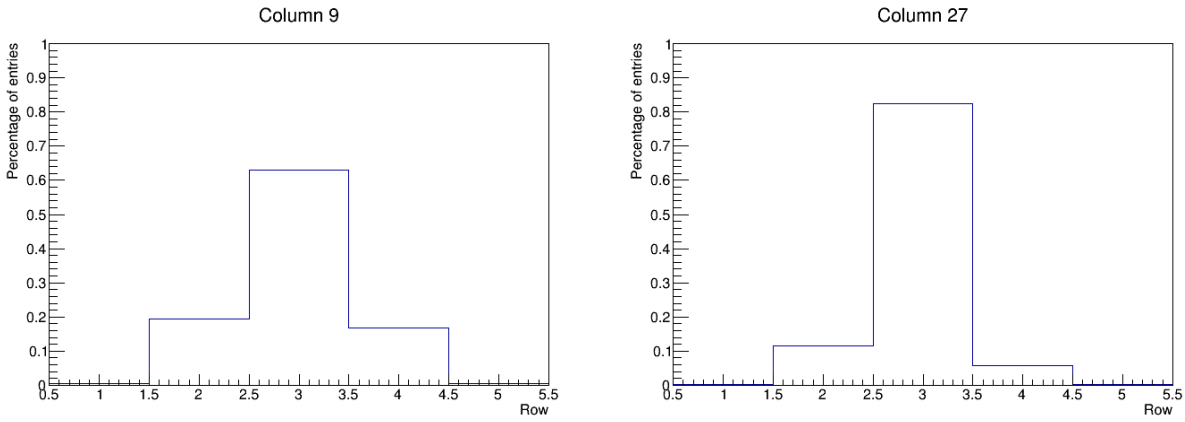

(a) Column 9 coincidence alignment

(b) Column 27 coincidence alignment

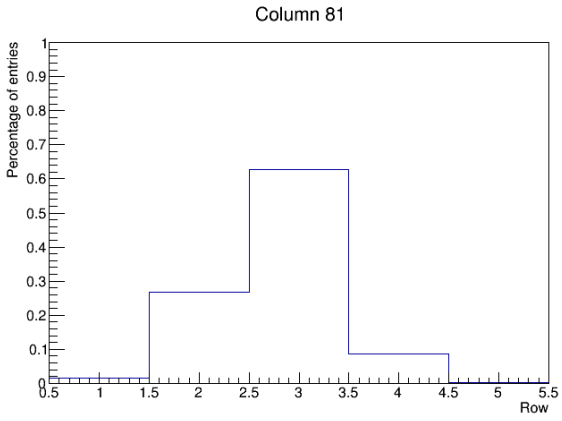

(c) Column 81 coincidence alignment

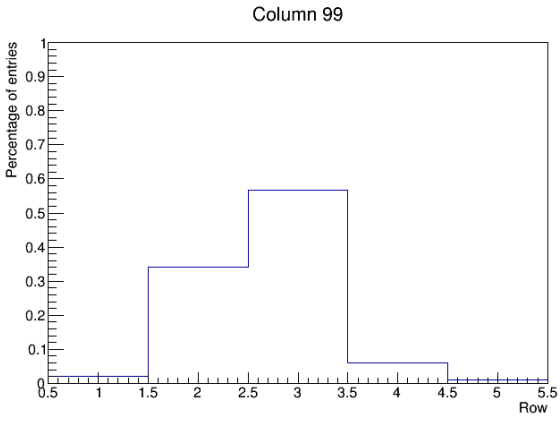

(d) Column 99 coincidence alignment

Figure 4.8: The vertical TAGM alignment in coincidence with the hall detectors. The y-axis shows the percentage of hits seen by a given row. The beam is well centered upstream but slowly drifts downward by the end of the microscope for this run.

In this run's configuration, it is clear from the figure that the central row is well aligned on the upstream end (columns 9 and 27) but at the downstream end, the electron plane appears to be drifting into the second row.

The next step in checking the alignment involved a fully calibrated experiment. The timing of the microscope was aligned with the GlueX detectors so that a coincidence peak was seen in the time difference between detectors. Only the hits that appear in coincidence were included in the alignment plots in order to exclude any hit that did not produce a photon which entered the hall. The result is shown in Fig. 4.8. As expected, the outer most rows have virtually no hits in coincidence with the detectors inside the hall. It is also be

seen that the central row contains the most hits, although, at the downstream end, the beam drifted into the second row (one row closer to the floor).

The alignment can change any time the accelerator reconfigures the optics and should therefore be routinely checked. An online monitoring of this alignment can be made by using the discriminator scalers, however, this would contain all hits seen by the TAGM and would serve as a check on the alignment with the pre-collimated beam, not the post-collimated beam which is only accessed by counting coincidences with a detector downstream of the collimator.

4.4 Timing & Timewalk Corrections

Before the microscope can be used to determine the energy of the photon, it must first have its timing calibrated. In section 3.1, it was explained that the signal from the microscope is split in a passive splitter, with one half of the signal going to a flash analog-to-digital converter (fADC) and the other half to a time-to-digital converter (TDC). The general procedure for the timing calibrations is to align the fADC and TDC times, align each of these to the accelerator RF signal, and match those times with the Start Counter (SC). Here, aligning means that the difference between the two detector times should be set to 0, though in general, it could be any arbitrary number. By setting these differences to 0, it is easy to locate the coincidence peak between the two detectors. This process is iterative and has been automated through the GlueX software and accompanying Python scripts.

In order to understand the timing calibrations, the concept of a timewalk should be explained first. This is a well-understood effect of leading edge discriminators (LEDs), which are the type of discriminator used with the microscope to provide an input for the TDC. As the name implies, the leading-edge discriminator transmits an output logic signal as soon as the leading edge of the input signal crosses a threshold. Because signals of varying amplitudes have the same rise time, it takes a different amount of time for the pulse to reach

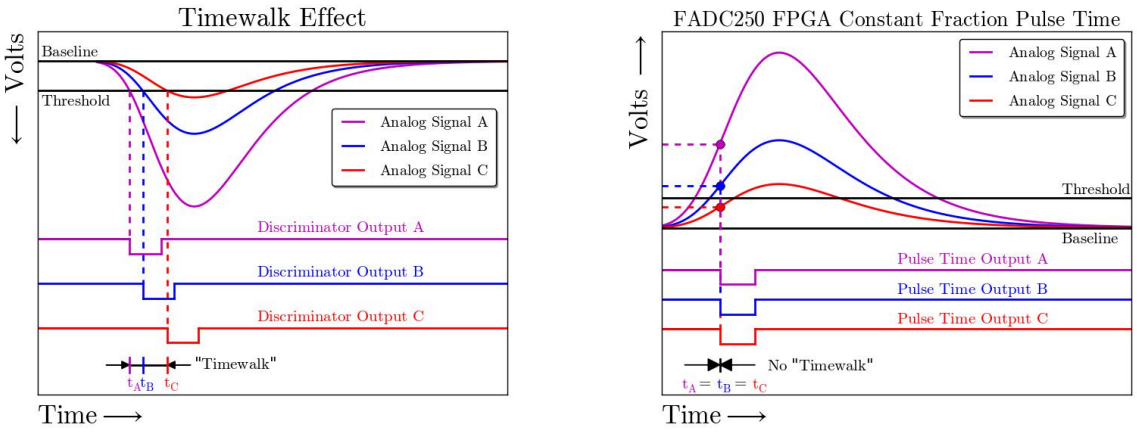

(a) Leading edge discriminator

(b) Constant fraction discriminator

Figure 4.9: (a) The leading edge varies based on pulse height causing a shift in time, called a timewalk. (b) The FPGA on the fADC acts as a constant fraction discriminator. This keeps the pulse time consistent regardless of the pulse height.

the threshold and report the pulse time. A representation of this can be seen in Fig. 4.9a. Signal A is much larger than signal C with their corresponding logic signals significantly different from each other in time despite the pulse starting at the same time. This shift is called a timewalk because the time "walks" as the pulse height varies.

This effect is virtually non-existent in constant fraction discriminators (CFDs) which generate an output logic signal when a particular percentage of the input pulse has been reached [30], as seen in Fig. 4.9b. These devices are costly, but fortunately, timewalks can be corrected for through offline analysis.

A logical place to start the TAGM timing calibrations is by aligning the fADC reported time with the RF signal from the accelerator that is synchronous with the arrival time of each beam pulse. The reason to start here is that the FPGA of the fADC emulates a CFD and removes virtually any shift in time due to the pulse height. This aligns the fADC time to some multiple of the beam period in comparison with the other detectors. The result of this calibration can be seen in Fig. 4.10.

In the same pass through the data, the uncorrected TDC time can be brought into alignment with the fADC time. This is a rough, initial calibration of the TDC time as it

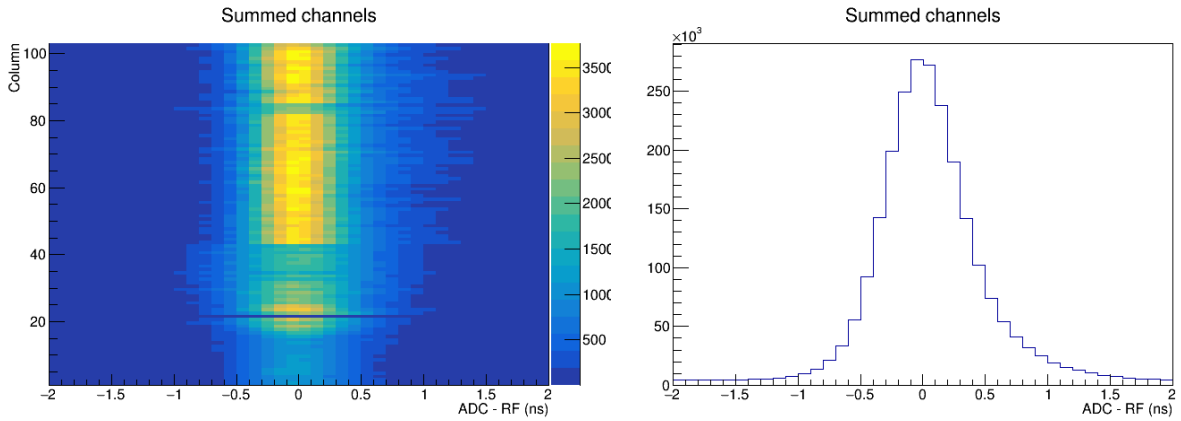

(a) fADC time and RF Δt for all channels (b) fADC time and RF Δt for a single channel

Figure 4.10: The result of the initial calibration of the fADC time against the RF for all of the summed output channels.

is still affected by the timewalk. Once this step is finished, the calibration constants in the CCDB are updated and another pass through the data is required.

At this point, the timewalk effect needs to be taken into account. To provide the best timing alignment, the RF should be used because its resolution is 60 ps, far better than any other reference source in the experiment. One difficulty with using the RF is that it appears every beam bunch. By directly referencing the TDC time with the nearest RF time, multiple distributions appear due to the large timewalk effect. To avoid this, the RF time closest to the associated fADC time is used. This provides a single RF time as a reference for the TDC time.

To correct for the timewalk effect, a histogram of the time difference as a function of pulse height is collected for each channel. An example of this can be seen in Fig. 4.11a. The timewalk distribution is clearly nonlinear and requires a polynomial to fit the data. The functional form of the fit is shown in Eq. 4.1,

$$t_{tw} = c_0 + c_1 \left(\frac{1}{x + c_3} \right)^{c_2} \tag{4.1}$$

where x is the pulse height from the fADC and the parameters c_i are the free parameters of the fit. This form was determined empirically and was based on the form found in Ref. [31]. The time difference is shown in Fig. 4.11b which shows an asymmetric distribution due to

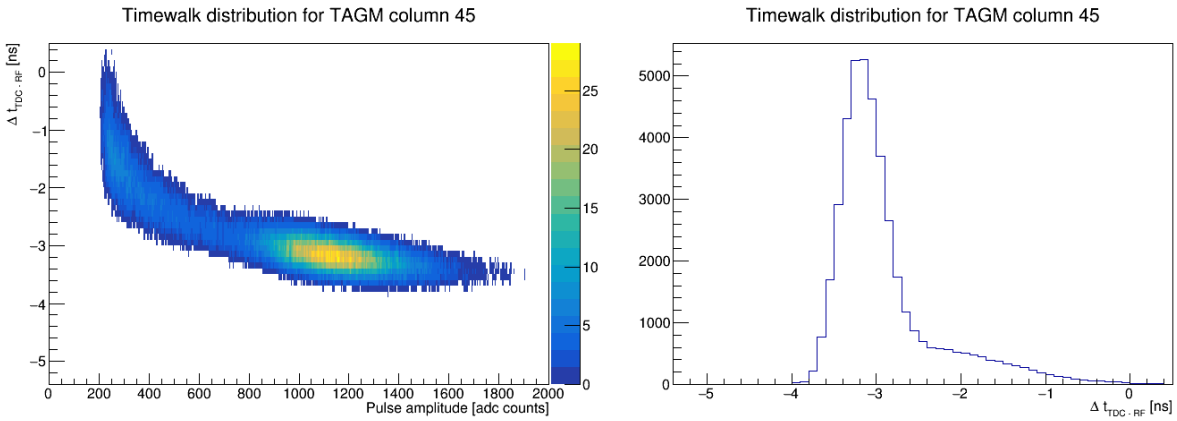

(a) Timewalk effect in a single channel (b) Timewalk effect on the timing distribution

Figure 4.11: (a) The time difference between the raw TDC time and the RF as a function of pulse height. Low amplitude pulses are shifted by a few nanoseconds. (b) Projection of timewalk spectrum onto the time axis. The distribution is asymmetric as a result of the timewalk effect. Using a Gaussian distribution to fit the spectrum, $\sigma = 263\ ps$.

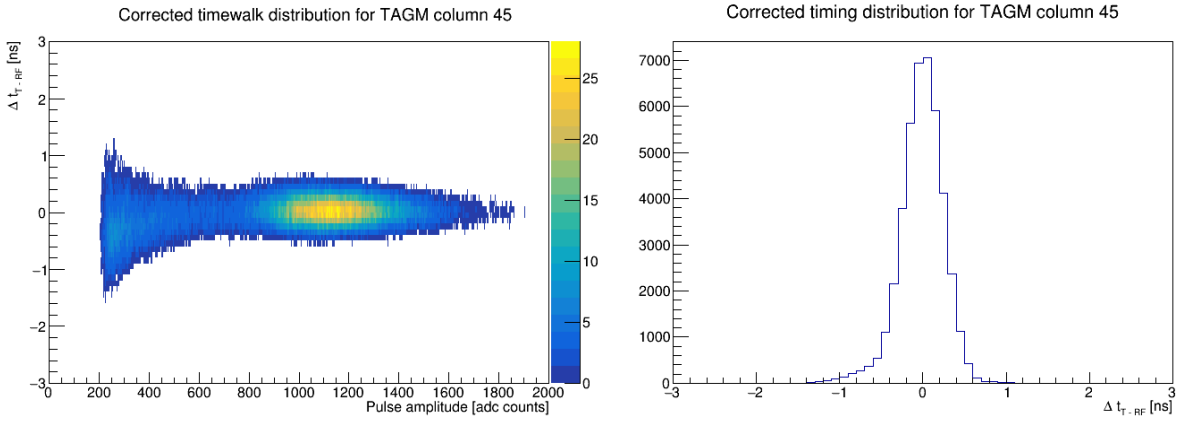

(a) Corrected timewalk spectrum (b) Corrected timing distribution

Figure 4.12: (a) The result of applying timewalk corrections. The timing is centered about 0 for all pulse heights. (b) The timing distribution is well centered and symmetric. A Gaussian fit yields $\sigma = 183\ ps$.

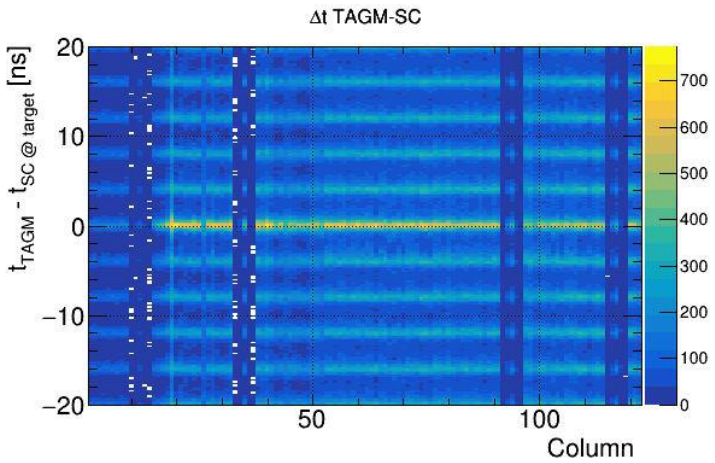

Figure 4.13: The time difference between the TAGM and the SC for all channels. A coincidence peak can be seen at $t = 0$. The vertical breaks correspond to the set of 4 columns with individual readout.

the timewalk effect and worsens the timing resolution of the channel, in this case a resolution of 263 ps. Additionally, the mean of this fit is used as a reference time, t_0, when correcting for the timewalk. Once all of the parameters have been measured, the TDC can be corrected using the formula 4.2,

$$t_{corr} = t_{raw} - c_1 \left(\frac{1}{x + c_3} \right)^{c_2} - (c_0 - t_0) \tag{4.2}$$

where t_{corr} is the new, corrected TDC time, t_{raw} is the original TDC time, x is the fADC pulse height, c_i are the fit parameters, and t_0 is the reference time found from the fit to the timing distribution. Once the corrections are applied, the dependence on the pulse height is removed and a narrower timing distribution is achieved, as illustrated in Fig. 4.12.

After the timewalk corrections are applied, another pass over the data is used to ensure that the corrected TDC times are in line with the fADC times, and in turn, the RF time. The timing resolution for the whole detector is shown in Fig. 2.10. The microscope is compared with the SC time which acts as a reference for all of the GlueX detectors. At this stage of calibration, the microscope is some multiple of the beam period off from the SC time. A separate procedure is used to determine the time offsets for all detectors in reference to the SC time. Once this is complete, the TAGM time can be used to tag photons (see Fig. 4.13).

4.5 Bias Voltage Optimization

Due to the variation in manufacturing SiPMs, each one has its own breakdown threshold voltage which is the point where it will begin to produce a signal. Hamamatsu provided recommended bias voltages for each of the SiPMs purchased for the microscope. Initially, it was these recommended values that were used. The idea was to start with these voltages and see what the performance was. It was quickly understood that new voltages were required to get the best performance from the microscope.

The motivation to adjust the biases came partly from the performance of the low-yield fibers. It was questioned whether the fibers produced an insufficient amount of photons, or if the SiPMs were not sufficiently biased. The first method for adjusting the bias voltages was to set the gain to the same level for all SiPMs. Each SiPM had a unique bias voltage but the signal gain in units of collected charge per pixel was uniform throughout the whole detector.

The procedure involved taking special TAGM runs. In order to measure the gain from each SiPM, only one row of SiPMs were turned on at a time. This caused the summed output to only contain one signal and therefore become an individual readout through the summing circuit. This method required that there be no beam and for the preamplifier be set to high gain mode. The dark pulse spectrum from each SiPM was measured, where the dark pulse is the spontaneous avalanche of a SiPM pixel. In high gain mode, this is used to measure the spectrum of single-pixels in units of fADC counts. Each SiPM had its single-pixel peak measured for three different bias voltages. For each SiPM, the single-pixel peak was plotted as a function of voltage in order to measure the gain and to determine the correct breakdown voltage. Once the SiPM is sufficiently beyond breakdown, the gain can be modeled linearly. This meant that the x-intercept corresponded to the breakdown voltage and the slope adc/V could be used to predict the output charge per pixel of the SiPM. Separate measurements at UConn using a charge-to-digital converter (QDC) found that 1 pC of charge collected by

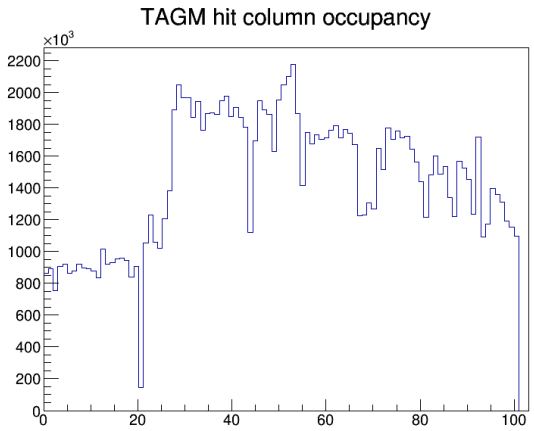

Figure 4.14: TAGM occupancy with the SiPMs gain balanced. The x-axis is the column number. The coherent edge can be seen clearly but the overall occupancy is ragged.

the preamplifier in high-gain mode equated to 100 adc. This was used to convert the slope of adc/V into $pF/pixel$.

To take advantage of this calibration, the control and monitoring tools mentioned in Sec. 3.2, TAGMutilities, were updated. The setVbias command reads in a configuration file containing the SiPM location information as well as its threshold and gain values in order to determine the proper bias voltage. A user executing setVbias specifies the gain in pC using the option "-g" where the optimal gain has been determined to be a value of 0.45 pC. The voltage for each channel is then calculated as

$$V = V_{threshold} + \frac{g}{C_{pixel}}, \tag{4.3}$$

where $V_{threshold}$ is the breakdown voltage measured for that SiPM, g is the specified gain in pC, and C_{pixel} is the measured capacitance per pixel in pF for that SiPM. Once these calibration constants were measured, the preamplifiers were switched back to low-gain mode for production running at a fixed g value chosen in common for all 510 channels.

The advantage of this method was that it made all of the channels have the same gain, however, it neglected the variation in output due to varying photon yield from the fibers. This caused non-uniform pulse heights throughout the detector and the low-yield fibers continued to cause issues in the analyses. One negative side effect was that within a single

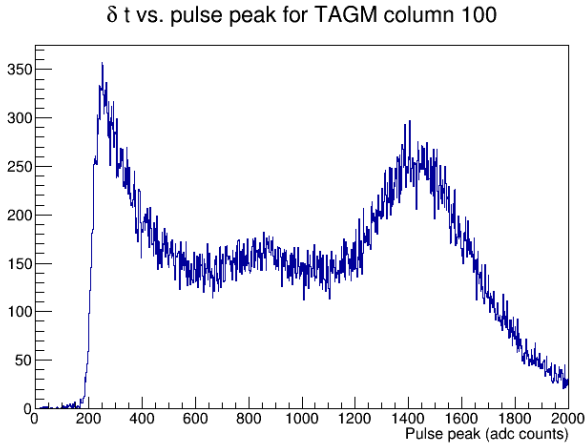

Figure 4.15: Summed output with multiple signal peaks. The y-axis is the yield and the x-axis is the pulse height in ADC counts.

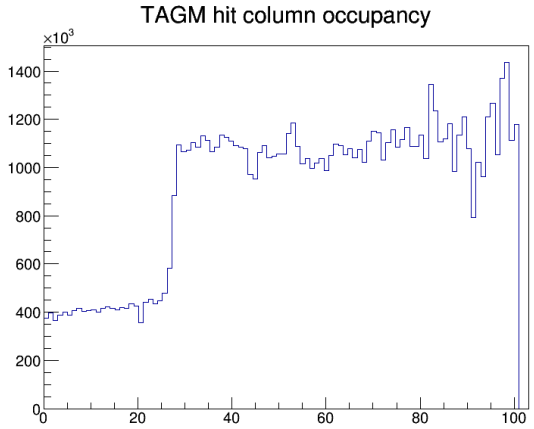

Figure 4.16: TAGM occupancy with the SiPMs biased such that all pulse spectra have a common average pulse height. The x-axis is the column number.

summed output, multiple peaks were seen due to varying photon yields, as seen in Fig. 4.15. A look at the TAGM occupancy plot with this setting also demonstrated the need for a better method (Fig. 4.14). At the time, only a single threshold value could be set for the fADC and discriminators, so the threshold was brought down low to accept the low-yield columns but it allowed a lot of background in the high-yield channels.

The next iteration was to set the bias voltages such that all channels had the same pulse height distribution. With this configuration, a single threshold would be needed for the entire detector. The new method required taking beam data at the same three bias voltages

used for the dark rate measurements. From this, like with the initial gain balancing method, a linear fit was used to determine the photon yield per pixel. TAGMutilities was updated again to include a new yield value for each channel of the TAGM. An additional argument "-p" was added to setVbias which specified the peak pC for axial high-energy electron hits. The calculation of the voltage was as follows

$$V = V_{threshold} + \sqrt{\frac{p}{C_{pixel} \cdot y}}, \tag{4.4}$$

where $V_{threshold}$ is the breakdown voltage, p is the peak charge in pC, C_{pixel} is the capacitance per pixel in pF, and y is the desired yield in pixels/hit/V. To prevent low values of p for some channels from over-biasing the SiPM using Eq. 4.4, a check is made against the calculated voltage from Eq. 4.3 which acts as a maximum allowed voltage. A p value of 15 was chosen which decreased the bias voltage on the good fibers significantly. To recover from the overall low amplitude pulses, it was decided to run in high gain to create a larger gap between the baseline and the average pulse height. This provided more range in determining the proper threshold. The results of this method are shown in Fig. 4.16.

Upon further inspection of this method, it was noticed that low-yield fibers could reduce the performance of the entire microscope. Because the pulse height restriction, the high-yield fibers required a bias voltage that was barely over breakdown. This caused a worsening of the timing resolution by a factor of 50%.

Once the new fibers were installed, a new plan was created for the bias voltages. The average pulse height for each fiber in a column was made to be uniform but the average pulse height between columns was variable. Since the fibers within a column were all produced together, they were found to have similar yields. This created a uniform distribution within a column but required readout thresholds set individually for each column. In addition, low-yield fibers did not reduce the performance of the entire detector. The process of determining the properties of the SiPMs and fibers remained the same but the setVbias script was modified to support the new method. By adding the parameter "-l" and keeping the option "-g", the script calculates the proper bias voltages for each channel under the revised

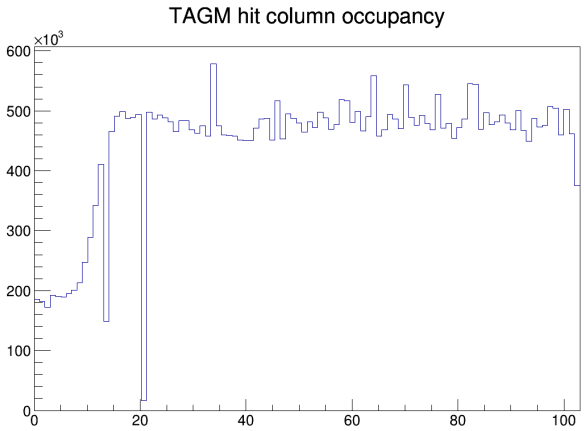

Figure 4.17: TAGM occupancy with the final SiPM optimization. The x-axis is the column number. The coherent peak is clearly seen near column 20. The dips in column 14 and 20 correspond to mixtures of low- and high-yield fibers.

column-matched biasing scheme. This method is the new standard and the results can be seen in Fig. 4.17.

4.6 Energy Calibration

During the spring 2015 run period, an accident with the accelerator's power grid caused the accelerator to temporarily be shut down. A truck collided with some low-hanging power line for one of two power feeds to the laboratory while the second was down undergoing maintenance. This unplanned interruption damaged some components of the accelerator, and after power was restored, the accelerator could only provide a 6 GeV beam. In order for Hall D to run, multiple magnets needed to be adjusted to account for the new energy. One particular magnet was the Pair Spectrometer (PS) dipole magnet which is the focus of this subsection.

The PS detects electron-positron pairs which are produced when the beam photons interact with a thin converter after the collimator. A dipole magnet steers the e^+, e^- pairs into their respective detectors on the left and right side of the beamline. The field of the magnet is adjusted to match the beam energy of the accelerator electrons. With the reduced

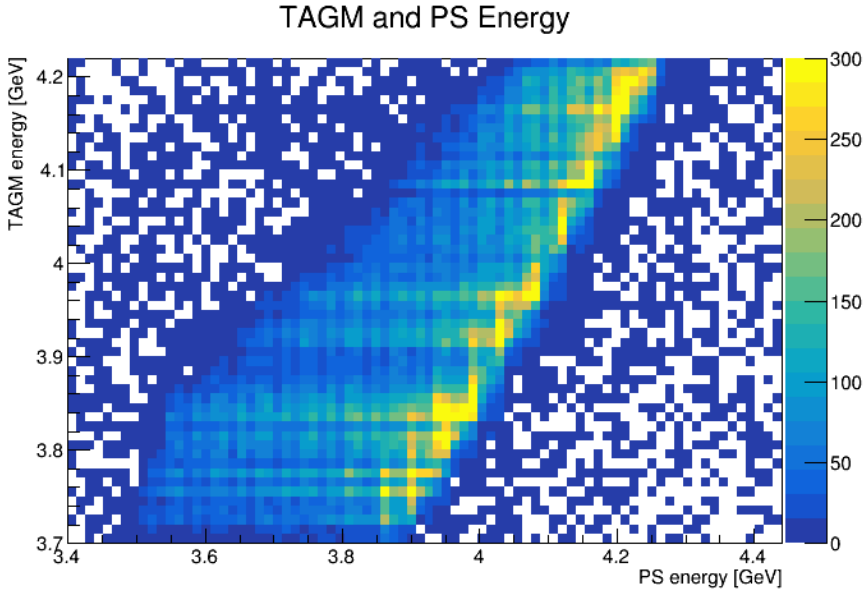

(a) PS and tagger correlated energies, uncorrected

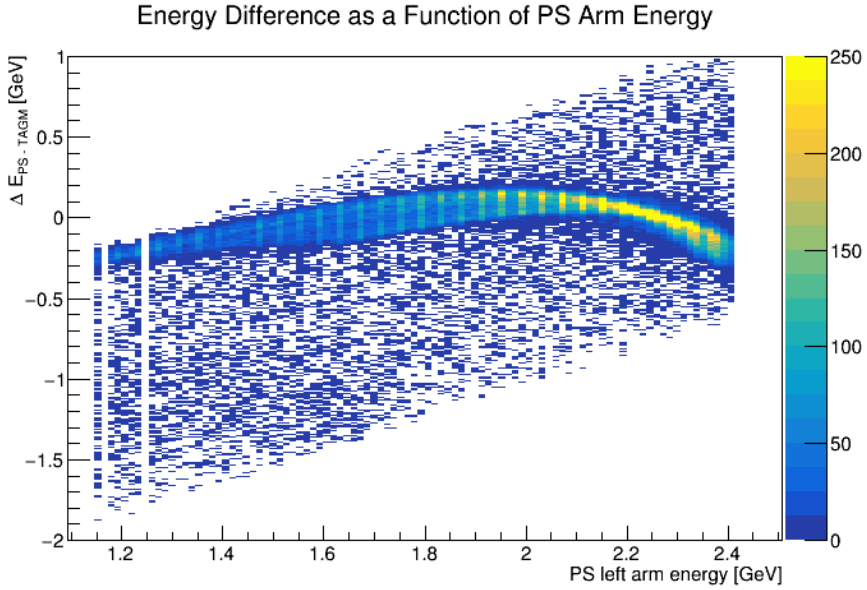

(b) ΔE as a function of left PS arm energy

Figure 4.18: (a) TAGM energy as a function of PS energy. Long horizontal tails towards lower PS energies indicate a wide distribution for a given PS energy. (b) The energy difference between the tagger and PS as a function of left PS arm energy. The bend at higher energies should not occur.

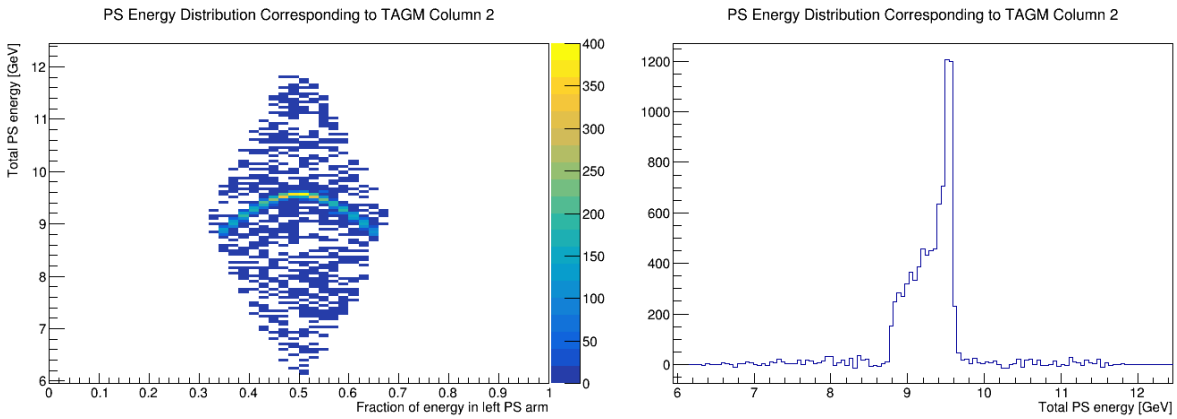

(a) Total PS energy as a function of left arm energy

(b) Uncorrected PS energy corresponding to TAGM column 2

Figure 4.19: (a) The total PS energy as a function of energy in the left PS arm corresponding to TAGM column 2. A maximum total energy occurs when the energy is split evenly between the two arms. (b) The reported PS energy associated with TAGM column 2. This produces a large spread in energies and causes issues when forming coincidences.

electron beam energy, the field of the magnet was also reduced. However, the mapping of the counters and their respective energies were not altered.

When measuring the performance of the TAGM, it is useful to correlate with the PS in both time and energy of detected hits. An incorrect energy map makes it difficult to analyze data. I worked on fixing this issue until a new energy map was created. Fig. 4.18 shows the energy match between the PS and the tagger before any corrections were made. In Fig. 4.18a, the TAGM energy is shown as a function of PS energy with long horizontal tails towards lower PS energies. This indicated that there was a wide range of energies correlated to a single TAGM energy. Fig. 4.18b shows the energy difference of the tagger and PS as a function of energy in the left PS arm. The curvature towards higher energies should not exist if the PS energy scale is calibrated properly.

One way to investigate the problem is to look at the total PS energy (the sum of the left and right counters) as a function of the fraction of energy in the left arm, as illustrated in Fig. 4.19. The relationship appears to be parabolic when it should be a flat distribution. As the energy of the pairs became asymmetric, the total PS energy became lower. This

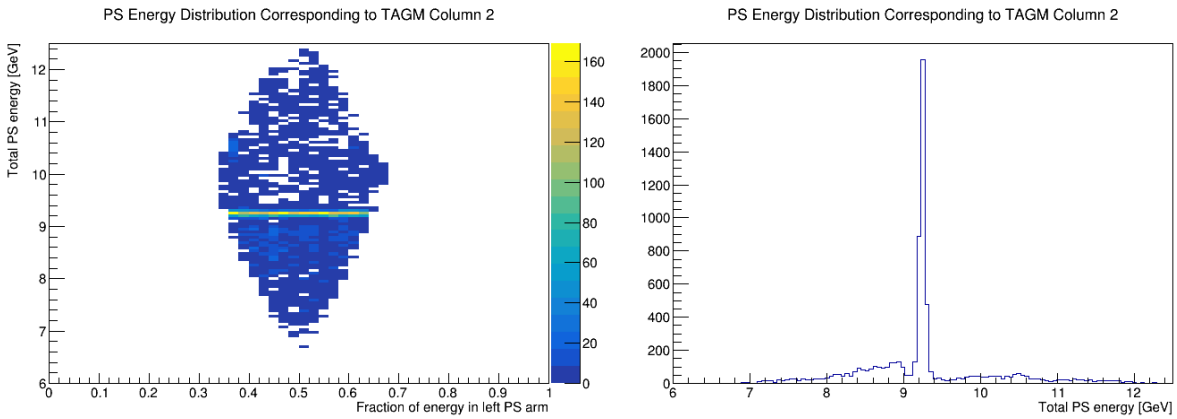

(a) Corrected total PS energy as a function of left arm energy

(b) Corrected PS energy corresponding to TAGM column 2

Figure 4.20: (a) The total PS energy as a function of energy in the left PS arm corresponding to TAGM column 2. The total energy is now independent on the arm energy asymmetry. (b) The reported PS energy associated with TAGM column 2. The correction provides a narrow band of energies in coincidence with TAGM column 2.

made it difficult to correlate hits in the tagger with the PS based on energy difference. This distribution was fit with a parabola which provided a good fit and was used to correct for the PS energies. The fit parameters were then used in the software by calculating the total PS energy and dividing it by the fit function with respect to the left arm's energy. The result of the correction can be seen in Fig. 4.20.

In later run periods, when the accelerator delivered 12 GeV electrons, it was noticed that this dependence still existed. The problem was not a missing energy map but rather an incorrect calculation of counter energy. The initial set of PS counter energies were based on the equation 4.5

$$x = -\frac{249 \text{ mm}}{3250 \text{ GeV}} E + 478.5 \text{ mm}, \tag{4.5}$$

where the energy of counter 1 is 2.995 GeV, counters 1-105 are 26 MeV wide (2 mm), and counters 106-145 are 13 MeV wide (1 mm), for a current of 991.4 A and a field of 1.78 T. This was an incorrect distribution of counter energy as the position of the counter from the beamline should be linear in (1/E), as seen in equation 4.6

$$x = \frac{1637.32 \text{ mm} \cdot \text{GeV}}{E} - 242.25 \text{ mm}. \tag{4.6}$$

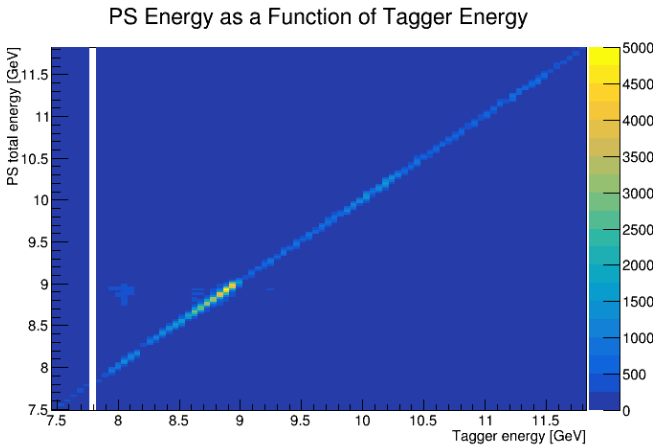

Figure 4.21: Corrected PS energy as a function of tagger energy.

To match with the counters, only two specific counter values need to be known from simulation. Once the counter energies were updated, the correlation between the PS and tagger was as expected, as seen in Fig. 4.21.

4.7 Hit Clustering

In addition to the alignment, multiple recorded hits due to a single electron needed to be taken into account. Where the alignment procedure made sure that the proper row was centered on the electron plane, the clustering procedure took into account electrons which did not travel axially into the microscope fibers. This meant that an electron produced a signal in one fiber and then entered another fiber to produce a second signal. Based on the geometry and direction of incoming electrons, it was expected that the electrons only produce secondary signals in the neighboring fibers immediately downstream.

For a given event, many TAGM channels register hits from both signal and background events. However, to determine if these should be considered a cluster, one needs to look at the time difference between hits and to check if they are from neighboring channels. In the GlueX software, all DTAGMHit objects for an event are sorted based on their column. Each hit was compared with all of the remaining hits in the event, comparing the time and column

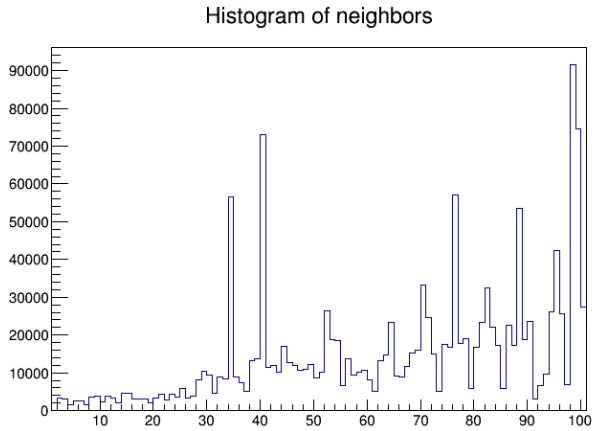

Figure 4.22: Occupancy plot of neighboring hits. The x-axis is the column number. The larger peaks correspond to the 4^{th} column in a fiber bundle of 6. This is the first column of the recessed set of 3.

between hits. If a neighboring column contained a hit within 5 ns, the hits were considered a cluster and the upstream-most hit's information was used. These hits were included in a list of used objects to prevent future iterations of the loop from considering them. This process occurs during the creation of DTAGMHit objects.

A occupancy plot of the columns that are considered to be neighbors can be seen in Fig. 4.22. This figure shows a pattern of peaks, especially above column 30 where the coherent edge is located. Recall that the photon energy decreases as the column number increases. A closer look at which columns have the peaks shows that these are always the fourth column in a bundle of six. This corresponds to the first recessed column on the S-bend block. Because these columns are held tightly against the neighboring fibers, and because they are recessed by inches, it is much easier for an electron to pass through the third column and enter the fourth column. The first column of each S-bend are not neighbors as often because there is a shim between each block to account for the change in β angle which provides a little extra gap between columns.

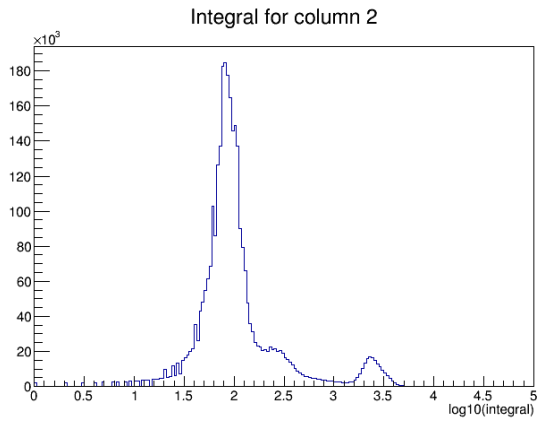

(a) Pulse integral distribution before cuts.

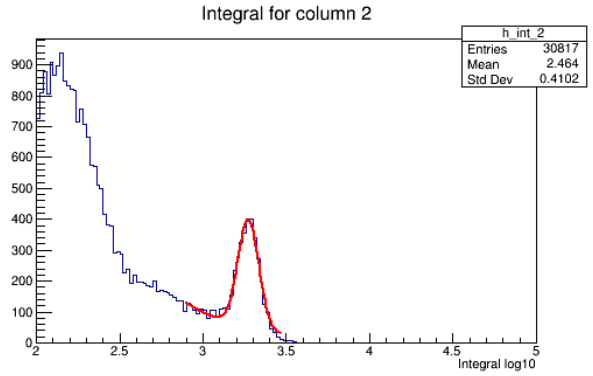

(b) A fit to the pulse integral and background

Figure 4.23: Pulse integral distributions for a particular TAGM column. (a) The pulse integral distribution before applying cuts where the x-axis is the $\log_{10}$ of the pulse integral in ADC counts. The low amplitude background peak can be seen at 2, and the usable signal creates a peak near 3.4. (b) A fit to the distribution using an exponential and a Gaussian more accurately measures the pulse integral. A cut of 5σ below the Gaussian mean was used for the software cut.

4.8 Pulse Integral Cuts

For a tagging spectrometer, it is important to keep a relatively low readout threshold to keep the tagging detection efficiency high. This efficiency is calculated by taking the ratio of the number of photons seen by the PS and coincident with the TAGM to the number of photons seen by the Pair Spectrometer in total (Eq. 4.7).

$$e = \frac{N_{\gamma,PS+TAGM}}{N_{\gamma,PS}} \tag{4.7}$$

By using a low threshold, background is introduced which needs to be considered. At the time that this calibration was performed, individual channel thresholds were not available and required the choice of a single threshold that must work for all channels.

One solution was to clean up the events in offline software by making a software threshold cut. This was done by making a cut on the pulse integral when creating the DTAGMHit objects. Fig. 4.23a shows a typical pulse integral distribution where the x-axis is the $\log_{10}$ of the pulse integral in ADC counts. Low amplitude background generates the large peak at 2 and the usable signal creates a peak near 3.4. This distribution was fit with an exponential

and a Gaussian to provide a more accurate measure of the mean pulse integral, as illustrated in Fig. 4.23b. Typically, the software threshold cut was placed 5σ below the Gaussian mean, though depending on the desired purity, this was adjusted. Once it became possible to set individual thresholds on each channel, this method was used to determine an effective threshold for each fADC and discriminator channel.

CHAPTER 5

ϕ-meson Analysis

5.1 Introduction

GlueX began taking commissioning data in fall 2014. During this time, calibrations were performed so that in the spring, further commissioning as well as production data could be taken, where commissioning data are for particular calibration measurements and production data are those which are expected to be analyzed for physics results. Unfortunately, due to problems with the accelerator and later the solenoid quenching, only about 3 hours worth of data were taken in spring 2015. It was not until spring 2016 that the detectors were sufficiently calibrated and a large portion of the run was dedicated to collecting production data.

The run contained 26 billion physics triggers where the trigger requires that the energy sum be: $E_{FCAL} + 4 \cdot E_{BCAL} > 0.5\ GeV$. This was divided up into three categories: PARA, PERP and AMO, where PARA and PERP refer to the direction of the photon's linear polarization with respect to the experimental floor, and AMO referring to the use of an amorphous (aluminum) radiator instead of a diamond crystal. PARA and PERP had roughly equal triggers, about 11 billion each, and AMO had about 4 billion triggers. The portion of the run analyzed in this chapter is from run 11366 to 11555 which uses a 3.4 mm collimator diameter, a beam current of 160 nA for PARA runs, with a beam period of 4 ns. The number of PARA events analyzed in this region are 2.5 billion.

Using this data set, I studied the reaction $\gamma p \to \phi p$, where $\phi \to K^+K^-$. The $\phi(1020)$ meson is particularly interesting because of its $s\bar{s}$ content which suppresses light-quark exchange due to the Okubo-Zweig-Iizuka (OZI) rule. It is expected to be produced primarily by Pomeron exchange and is therefore a useful tool in understanding Pomeron exchange in the t-channel [32]. In the Regge pole model, Pomeron exchange is assumed to dominate diffractive production amplitudes at high energies which leads to a cross section that is

roughly constant as a function of Mandelstam s. However, at 9 GeV, this is not strictly a diffractive process and deviations from this are expected. Additionally, this analysis served as a high-level calibration of the GlueX detector. Before the experiment can search for exotic hybrid mesons, it must first successfully measure well-known mesons. This analysis helped in understanding the detector acceptances and the sensitivity of detecting states with strange quark content.

In order to understand the production of the ϕ, the decay angular distribution was analyzed. This was performed by measuring its spin-density matrix elements (SDME). This chapter provides a background on SDMEs as well as details the analysis of both experimental and simulated data. Lastly, the results are discussed and compared with previous experimental results.

5.2 Spin-density Matrix Elements Theory

Consider the photoproduction of a vector meson,

$$\gamma N \to V N, \tag{5.1}$$

where the photon is polarized, the target nucleon is unpolarized, and the recoil nucleon polarization is not observed. It would be useful to know what information the decay distributions can provide on the production amplitudes. This section provides a way to write the decay distributions in terms of spin-density matrices of the vector meson, and explains what information can be extracted from these values following reference [33].

For an incident photon with four-momentum k and outgoing vector meson with four-momentum q, the following coordinate system can be made of their three-momentum vectors, $\mathbf{k}$ and $\mathbf{q}$

$$\mathbf{Z} = \frac{\mathbf{k}}{|\mathbf{k}|}, \qquad \mathbf{Y} = \frac{\mathbf{k} \times \mathbf{q}}{|\mathbf{k} \times \mathbf{q}|}, \qquad \mathbf{X} = \frac{(\mathbf{k} \times \mathbf{q}) \times \mathbf{k}}{|(\mathbf{k} \times \mathbf{q}) \times \mathbf{k}|}.$$

The polarization states of the photon and vector meson can be written in terms of their spin space density matrices $\rho(\gamma)$ and $\rho(V)$ which are related to the production amplitudes T

$$\rho(V) = T\rho(\gamma)T^{\dagger}. \tag{5.2}$$

This can be written in the center of mass helicity representation [34] as

$$\rho(V)_{\lambda_V\lambda'_V} = \frac{1}{n}\sum_{\lambda_{N'}\lambda_\gamma\lambda_N\lambda'_\gamma} T_{\lambda_V\lambda_{N'},\lambda_\gamma\lambda_N}\rho(\gamma)_{\lambda_\gamma\lambda'_\gamma}T^*_{\lambda'_V\lambda_{N'},\lambda'_\gamma\lambda_N}, \tag{5.3}$$

where λ's denote the helicities of the particles from reaction 5.1 and n is a normalization factor

$$n = \frac{1}{2}\sum_{\lambda_V\lambda_{N'},\lambda_\gamma\lambda_N} |T_{\lambda_V\lambda_{N'},\lambda_\gamma\lambda N}|^2 \tag{5.4}$$

This normalization can be chosen such that the production cross section for unpolarized photons is

$$\left(\frac{d\sigma}{d\Omega}\right)^{unpol} = \left(\frac{2\pi}{k}\right)^2\frac{n}{2} \tag{5.5}$$

For the remainder of the derivation, the helicity frame is used. The z direction is set opposite to the direction of the outgoing nucleon in the V rest frame, or in other words, equal to the direction of flight of the vector meson in the overall center of mass frame. The y direction is chosen to be normal to the production plane which is defined by the cross product $\mathbf{k}\times\mathbf{q}$. The x direction is simply $\mathbf{x} = \mathbf{y}\times\mathbf{z}$. The decay angles θ, ϕ are the polar and azimuthal angles determined by the direction of one of the decay products of the vector meson in a two-body decay, which for convenience is denoted as the unit vector π. For my analysis, the K^+ provides the reference for the decay angles (see Fig. 5.1).

$$\cos\theta = \pi\cdot\mathbf{z}, \qquad \cos\phi = \frac{\mathbf{y}\cdot(\mathbf{z}\times\pi)}{|\mathbf{z}\times\pi|}, \qquad \sin\phi = -\frac{\mathbf{x}\cdot(\mathbf{z}\times\pi)}{|\mathbf{z}\times\pi|} \tag{5.6}$$

The Gottfried-Jackson and Adair systems are used in later model predictions and only differ slightly from the helicity system. The only difference is the choice of z-axis. In the Gottfried-Jackson frame, the direction of flight of the incoming photon in the V rest frame

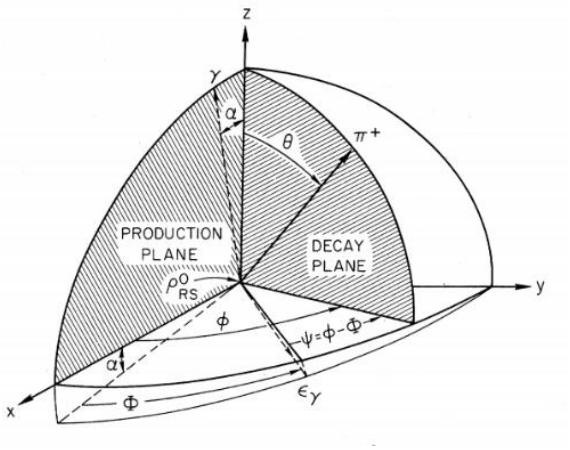

Figure 5.1: Angles used in the study of ϕ decay. The angle α is zero in the Gottfried-Jackson system.

is the z direction, whereas in the Adair system, the z direction is in the direction of the incoming photon in the center of mass frame.

The decay angular distribution in the rest frame of the vector meson is

$$\frac{dN}{d\cos\theta d\phi} = W(\cos\theta,\phi) = M\rho(V)M^\dagger = \sum_{\lambda_V\lambda'_V} \langle\theta,\phi|M|\lambda_V\rangle\rho(V)_{\lambda_V\lambda'_V}\langle\lambda'_V|M^\dagger|\theta,\phi\rangle \tag{5.7}$$

where M is the decay amplitude and

$$\langle\theta,\phi|M|\lambda_V\rangle = C\sqrt{\frac{3}{4\pi}}D^{1^*}_{\lambda_V 0}(\phi,\theta,-\phi). \tag{5.8}$$

This is for vector mesons decaying into spinless particles only, and $|C|^2$ is proportional to the decay width of the vector meson [35]. C and λ_V are independent due to rotational invariance. However, since a normalized decay angular distribution is being considered, C is one. The Wigner rotation functions D are given by

$$\begin{aligned} D^1_{10}(\phi,\theta,-\phi) &= -\frac{1}{\sqrt{2}}\sin\theta e^{-i\phi}, \\ D^1_{00}(\phi,\theta,-\phi) &= \cos\theta, \\ D^1_{-10}(\phi,\theta,-\phi) &= \frac{1}{\sqrt{2}}\sin\theta e^{i\phi}. \end{aligned} \tag{5.9}$$

Using Eq. 5.8, the distribution Eq. 5.7 can be written as

$$W(\cos\theta,\phi) = \frac{3}{4\pi}\sum_{\lambda_V\lambda'_V} D^1_{\lambda_V 0}(\phi,\theta,-\phi)^*\rho(V)_{\lambda_V\lambda'_V}D^1_{\lambda'_V 0}(\phi,\theta,-\phi). \tag{5.10}$$

Because $\rho(V)$ is hermitian ($\rho(V)_{\lambda_V\lambda'_V} = \rho^*(V)_{\lambda'_V\lambda_V}$), Eq. 5.10 can be re-written as

$$W(\cos\theta,\phi,\rho(V)) = \frac{3}{4\pi}\Big(\frac{1}{2}(\rho_{11}+\rho_{-1-1})\sin^2\theta + \rho_{00}\cos^2\theta + \frac{1}{\sqrt{2}}(-\operatorname{Re}\rho_{10}+\operatorname{Re}\rho_{-10})\sin 2\theta\cos\phi + \frac{1}{\sqrt{2}}(\operatorname{Im}\rho_{10}+\operatorname{Im}\rho_{-10})\sin 2\theta\sin\phi + -\operatorname{Re}\rho_{1-1}\sin^2\theta\cos 2\phi + \operatorname{Im}\rho_{1-1}\sin^2\theta\sin 2\phi\Big),$$

which can be simplified by using symmetries of $\rho(V)$ based on the properties of $\rho(\gamma)$ and T.

The density matrix $\rho^{pure}(\gamma)$ of a pure photon state can be constructed from the photon wave function $|\gamma\rangle$ in the helicity basis

$$|\gamma\rangle = a_+\Big|\lambda_\gamma = +1\Big\rangle + a_-\Big|\lambda_\gamma = -1\Big\rangle \tag{5.11}$$

where

$$\Big||\lambda_\gamma = \pm 1\rangle\Big|^2 = 1, \qquad |a_+|^2 + |a_-|^2 = 1.$$

This results in

$$\rho^{pure}(\gamma) = |\gamma\rangle\langle\gamma| = \begin{bmatrix} |a_+|^2 & a_+a_-^* \\ a_-a_+^* & |a_-|^2 \end{bmatrix} \tag{5.12}$$

In the case of linearly polarized photons, Eq. 5.11 is

$$|\gamma\rangle = -\frac{1}{\sqrt{2}}(e^{-i\Phi}|\lambda_\gamma = +1\rangle - e^{i\Phi}|\lambda_\gamma = -1\rangle) \tag{5.13}$$

where Φ is the angle between the polarization vector of the photon, $\epsilon = (\cos\Phi, \sin\Phi, 0)$, and the production plane (x-z plane). This leads to a density matrix of

$$\rho^{pure}(\gamma) = \frac{1}{2}\begin{bmatrix} 1 & -e^{2i\Phi} \\ e^{2i\Phi} & 1 \end{bmatrix} \tag{5.14}$$

This can be generalized to the case of partially polarized photons and can be written as a linear combination of the matrices I, σ_i (i = 1, 2, 3), which forms a complete set in the space of 2×2 hermitian matrices

$$\rho(\gamma) = \frac{1}{2}I + \frac{1}{2}\mathbf{P}_\gamma \cdot \sigma \tag{5.15}$$

where I is the unit matrix and σ_i are the Pauli matrices. The degree of polarization is the magnitude of $\mathbf{P}_\gamma$. For linearly polarized photons

$$\mathbf{P}_\gamma = P_\gamma(-\cos 2\Phi, -\sin 2\Phi, 0) \tag{5.16}$$

with $0 \leq P_\gamma \leq 1$.

Coming back to the production amplitudes, parity conservation gives the relation

$$T(\Theta^*)_{-\lambda_V-\lambda_{N'},-\lambda_\gamma-\lambda_N} = (-1)^{(\lambda_V-\lambda_{N'})-(\lambda_\gamma-\lambda_N)} T(\Theta^*)_{\lambda_V\lambda_{N'},\lambda_\gamma\lambda_N} \tag{5.17}$$

where Θ^* is the center of mass production angle. If in the t-channel only natural ($P = (-1)^J$) or only unnatural parity ($P = -(-1)^J$) exchanges contribute, then the additional symmetry exists to leading order in the energy

$$\begin{aligned} T(\Theta^*)_{-\lambda_V-\lambda_{N'},-\lambda_\gamma-\lambda_N} &= \pm(-1)^{\lambda_V-\lambda_\gamma} T(\Theta^*)_{\lambda_V\lambda_{N'},\lambda_\gamma\lambda_N} \\ &= \mp(-1)^{\lambda_V} T(\Theta^*)_{\lambda V\lambda_{N'},\lambda\gamma\lambda_N} \end{aligned} \tag{5.18}$$

where the upper (lower) sign is for natural (unnatural) parity exchanges.

The production amplitude can be broken up into natural and unnatural parts as

$$T = T^N + T^U \tag{5.19}$$

Making use of Eq. 5.17, T^N and T^U can be projected out

$$T^N_U(\Theta^*)_{\lambda_V\lambda_{N'},\lambda_\gamma\lambda_N} = \frac{1}{2}(T(\Theta^*)_{\lambda_V\lambda_{N'},\lambda_\gamma\lambda_N} \mp (-1)^{\lambda_V} T(\Theta^*)_{-\lambda_V\lambda_{N'},-\lambda_\gamma\lambda_N}) \tag{5.20}$$

The density matrix $\rho(V)$ can now explicitly show the dependence on the polarization vector $\mathbf{P}_\gamma$. From Eqs. 5.2 and 5.16

$$\rho(V) = \rho^0 + \sum_{i=1}^{3} P^\alpha_\gamma \rho^\alpha \tag{5.21}$$

where

$$(\rho^0, \rho^\alpha) = T(\frac{1}{2}I, \frac{1}{2}\sigma^\alpha)T^\dagger, \qquad \alpha = 1, 2, 3. \tag{5.22}$$

The ρ^α matrices are

$$\rho^0_{\lambda_V\lambda_{V'}} = \frac{1}{2n}\sum_{\lambda_\gamma\lambda_{N'}\lambda_N} T_{\lambda_V\lambda_{N'},\lambda_\gamma\lambda_N} T^*_{\lambda'_V\lambda_{N'},\lambda_\gamma\lambda_N} \tag{5.23a}$$

$$\rho^1_{\lambda_V\lambda_{V'}} = \frac{1}{2n}\sum_{\lambda_\gamma\lambda_{N'}\lambda_N} T_{\lambda_V\lambda_{N'},-\lambda_\gamma\lambda_N} T^*_{\lambda'_V\lambda_{N'},\lambda_\gamma\lambda_N} \tag{5.23b}$$

$$\rho^2_{\lambda_V\lambda_{V'}} = \frac{i}{2n}\sum_{\lambda_\gamma\lambda_{N'}\lambda_N} \lambda_\gamma T_{\lambda_V\lambda_{N'},-\lambda_\gamma\lambda_N} T^*_{\lambda'_V\lambda_{N'},\lambda_\gamma\lambda_N} \tag{5.23c}$$

$$\rho^3_{\lambda_V\lambda_{V'}} = \frac{1}{2n}\sum_{\lambda_\gamma\lambda_{N'}\lambda_N} \lambda_\gamma T_{\lambda_V\lambda_{N'},\lambda_\gamma\lambda_N} T^*_{\lambda'_V\lambda_{N'},\lambda_\gamma\lambda_N} \tag{5.23d}$$

The number of independent matrix elements is reduced due to parity conservation from Eq. 5.17

$$\rho^\alpha_{\lambda\lambda'} = (-1)^{\lambda-\lambda'}\rho^\alpha_{-\lambda-\lambda'}, \qquad \alpha = 0, 1, \tag{5.24}$$

$$\rho^\alpha_{\lambda\lambda'} = -(-1)^{\lambda-\lambda'}\rho^\alpha_{-\lambda-\lambda'}, \qquad \alpha = 2, 3, \tag{5.25}$$

It follows from these equations and the hermiticity of the ρ^α that ρ^0_{1-1}, ρ^1_{1-1} are real and ρ^2_{1-1}, ρ^3_{1-1} are purely imaginary. Because the decay distribution W is linear in $\rho(V)$, it can be decomposed similarly

$$W(\cos\theta, \phi, \rho) = W^0(\cos\theta, \phi) + \sum_{\alpha=1}^{3} P^\alpha_\gamma W^\alpha(\cos\theta, \phi) \tag{5.26}$$

The symmetries of Eq. 5.24 and 5.25, W^α can be written as

$$\begin{aligned}
W^0(\cos\theta,\phi) &= \frac{3}{4\pi}\Big(\frac{1}{2}(1-\rho^0_{00}) + \frac{1}{2}(3\rho^0_{00}-1)\cos^2\theta - \sqrt{2}\,\mathrm{Re}\,\rho^0_{10}\sin 2\theta\cos\phi - \rho^0_{1-1}\sin^2\theta\cos 2\phi\Big),\\
W^1(\cos\theta,\phi) &= \frac{3}{4\pi}\Big(\rho^1_{11}\sin^2\theta + \rho^1_{00}\cos^2\theta - \sqrt{2}\,\mathrm{Re}\,\rho^1_{10}\sin 2\theta\cos\phi - \rho^1_{1-1}\sin^2\theta\cos 2\phi\Big),\\
W^2(\cos\theta,\phi) &= \frac{3}{4\pi}\Big(\sqrt{2}\,\mathrm{Im}\,\rho^2_{10}\sin 2\theta\sin\phi + \mathrm{Im}\,\rho^2_{1-1}\sin^2\theta\sin 2\phi\Big),\\
W^3(\cos\theta,\phi) &= \frac{3}{4\pi}\Big(\sqrt{2}\,\mathrm{Im}\,\rho^3_{10}\sin 2\theta\sin\phi + \mathrm{Im}\,\rho^3_{1-1}\sin^2\theta\sin 2\phi\Big),
\end{aligned} \tag{5.27}$$

For the case of linear polarization

$$W(\cos\theta,\phi,\Phi) = W^0(\cos\theta,\phi) - P_\gamma\cos 2\Phi W^1(\cos\theta,\phi) - P_\gamma\sin 2\Phi W^2(\cos\theta,\phi). \tag{5.28}$$

The Eqs. 5.24 and 5.25 hold for any coordinate system that is reached from the helicity frame by a rotation R about the normal to the production plane.

There are restrictions on the values of the density matrices which must be taken into account while fitting experimental data. The limits are governed by the inequalities

$$|\rho^{\alpha}_{\lambda\lambda'}|^2 \leq \rho^{0}_{\lambda\lambda}\rho^{0}_{\lambda'\lambda'} \qquad \alpha = 0, 1, 2, 3, \tag{5.29}$$

$$\det \rho(V) = \prod_{i=1}^{3} \mu_i \geq 0, \tag{5.30}$$

$$Tr\rho(V) = \sum_{i=1}^{3} \mu_i \geq 0, \tag{5.31}$$

$$\sum_{i} \det R(V)_{ii} = \mu_1\mu_2 + \mu_1\mu_3 + \mu_2\mu_3 \geq 0, \tag{5.32}$$

where μ_i, $i = 1, 2, 3$, are the eigenvalues of $\rho(V)$, and $R(V)_{ii}$ denotes the adjoint of $\rho(V)_{ik}$. These lead to the conditions

$$\rho(V)_{\lambda\lambda} \geq 0. \tag{5.33}$$

Eq. 5.29 comes from applying the Schwarz inequality to the bilinear expression in the helicity amplitudes for the ρ^{α}. Eqs. 5.30 - 5.32 are the necessary and sufficient conditions for positive definiteness.

By making use of hermiticity and parity conservation, the density matrices ρ^0, ρ^1, ρ^2, ρ^3 are then

$$\rho^0 = \begin{bmatrix} \frac{1}{2}(1-\rho^0_{00}) & \mathrm{Re}\,\rho^0_{10} + i\,\mathrm{Im}\,\rho^0_{10} & \mathrm{Re}\,\rho^0_{1-1} \\ & \rho^0_{00} & -(\mathrm{Re}\,\rho^0_{10} - i\,\mathrm{Im}\,\rho^0_{10}) \\ & & \frac{1}{2}(1-\rho^0_{00}), \end{bmatrix}$$

$$\rho^1 = \begin{bmatrix} \rho^1_{11} & \mathrm{Re}\,\rho^1_{10} + i\,\mathrm{Im}\,\rho^0_{10} & \mathrm{Re}\,\rho^1_{1-1} \\ & \rho^1_{00} & -(\mathrm{Re}\,\rho^1_{10} - i\,\mathrm{Im}\,\rho^1_{10}) \\ & & \rho^1_{11}, \end{bmatrix}$$

$$\rho^2 = \begin{bmatrix} \rho^2_{11} & \mathrm{Re}\,\rho^2_{10} + i\,\mathrm{Im}\,\rho^2_{10} & i\,\mathrm{Im}\,\rho^2_{1-1} \\ & 0 & (\mathrm{Re}\,\rho^2_{10} - i\,\mathrm{Im}\,\rho^2_{10}) \\ & & -\rho^2_{11}, \end{bmatrix} \tag{5.34}$$

$$\rho^3 = \begin{bmatrix} \rho^3_{11} & \mathrm{Re}\,\rho^3_{10} + i\,\mathrm{Im}\,\rho^3_{10} & i\,\mathrm{Im}\,\rho^3_{1-1} \\ & 0 & (\mathrm{Re}\,\rho^3_{10} - i\,\mathrm{Im}\,\rho^3_{10}) \\ & & -\rho^3_{11}, \end{bmatrix}$$

where the lower half of the matrices are completed by the hermitian conjugates.

Insight into the contributions of natural and unnatural parity exchange in the t-channel to $\mathrm{Re}\,\rho^0$ and $\mathrm{Re}\,\rho^1$ can be provided by experiments with linearly polarized photons in the reaction 5.1. At sufficiently high energies, the density matrix elements ρ^α can be written as a sum of the natural and unnatural contributions, for example ρ^0

$$\rho^0 = \rho^{0(N)} + \rho^{0(U)}, \qquad \rho^{0\binom{N}{U}}_{\lambda\lambda'} = \frac{1}{2n} \sum_{\lambda_\gamma \lambda_N \lambda_{N'}} T^{\binom{N}{U}}_{\lambda\lambda_{N'},\lambda_\gamma\lambda_N} T^{\binom{N}{U}*}_{\lambda'\lambda_{N'},\lambda_\gamma\lambda_N} \tag{5.35}$$

This leads to the equations

$$\rho^0 = \rho^{0(N)} + \rho^{0(U)}, \qquad \rho^{0\binom{N}{U}}_{\lambda\lambda'} = \frac{1}{2}(\rho^0_{\lambda\lambda'} \mp (-1)^\lambda \rho^1_{-\lambda\lambda'}), \tag{5.36}$$

$$\rho^1 = \rho^{1(N)} + \rho^{1(U)}, \qquad \rho^{1\binom{N}{U}}_{\lambda\lambda'} = \frac{1}{2}(\rho^1_{\lambda\lambda'} \mp (-1)^\lambda \rho^0_{-\lambda\lambda'}), \tag{5.37}$$

$$\rho^2 = \rho^{2(N)} + \rho^{2(U)}, \qquad \rho^{2\binom{N}{U}}_{\lambda\lambda'} = \frac{1}{2}(\rho^2_{\lambda\lambda'} \mp i(-1)^\lambda \rho^3_{-\lambda\lambda'}), \tag{5.38}$$

$$\rho^3 = \rho^{3(N)} + \rho^{3(U)}, \qquad \rho^{3\binom{N}{U}}_{\lambda\lambda'} = \frac{1}{2}(\rho^3_{\lambda\lambda'} \pm i(-1)^\lambda \rho^2_{-\lambda\lambda'}), \tag{5.39}$$

which hold in all coordinate systems that can be reached by a rotation about the normal of the production plane from the helicity frame. The parity asymmetry P_σ in the σ^N and σ^U of the total cross section is given by

$$P_\sigma = \frac{\sigma^N - \sigma^U}{\sigma^N + \sigma^U} = 2\rho^1_{1-1} - \rho^1_{00} \tag{5.40}$$

and the quantity Σ by

$$\Sigma = \frac{\sigma_\parallel - \sigma_\perp}{\sigma_\parallel + \sigma_\perp} = \frac{\rho^1_{11} + \rho^1_{1-1}}{\rho^0_{11} + \rho^0_{1-1}}. \tag{5.41}$$

The helicity conservation model (HCM) predicts vector-meson photoproduction to occur via diffraction. This model predicts that the ρ matrices are independent of photon energy and production angle and that ρ^0 and ρ^3 are diagonal while ρ^1 and ρ^2 are anti-diagonal. The appropriate reference system for analyzing the vector meson decay is the helicity frame for HCM. Assuming only natural parity exchange, the density matrices are then

$$\begin{aligned}
\rho^0 &= \begin{bmatrix} \frac{1}{2} & 0 & 0 \\ 0 & 0 & 0 \\ 0 & 0 & \frac{1}{2} \end{bmatrix}, \qquad \rho^1 = \begin{bmatrix} 0 & 0 & \frac{1}{2} \\ 0 & 0 & 0 \\ \frac{1}{2} & 0 & 0 \end{bmatrix}, \\
\rho^2 &= \begin{bmatrix} 0 & 0 & -\frac{i}{2} \\ 0 & 0 & 0 \\ \frac{i}{2} & 0 & 0 \end{bmatrix}, \qquad \rho^3 = \begin{bmatrix} \frac{1}{2} & 0 & 0 \\ 0 & 0 & 0 \\ 0 & 0 & -\frac{1}{2} \end{bmatrix}.
\end{aligned} \tag{5.42}$$

5.3 Event Selection

The selection of $\gamma p \to \phi p$ was performed using the standard GlueX analysis software framework [36] which uses a JANA plugin to create TTrees containing the desired particle combinations. The TTrees were then analyzed using the DSelector framework [37] which makes further cuts and produces another set of TTrees. The requirements in the JANA plugin are used to reduce the data size while remaining loose so as to not lose any potential signal

events. The DSelector is then used to make tighter cuts. The cuts described in this section are used on both experimental data and Monte Carlo (MC) simulation.

The plugin requires that there be one tagged beam photon, two reconstructed positively charged tracks, and one reconstructed negatively charged track, which together create a single combination and match the desired decay. An additional 4 "good" tracks were allowed to be present in the event, where "good" means that the tracks were well formed and likely not a statistical fluctuation. The additional tracks were kept because a given event might have background tracks in addition to the signal and should be looped over. Using all unique combinations of the reconstructed particles led to the possibility of multiple hypotheses for a single event. Double counting is prevented by keeping track of the particles used in a combination and preventing their use in additional combinations.

A kinematic fit was also included in the plugin which fits the reconstructed tracks to a common vertex as well as constrain the decaying particle mass based on the four-momenta of the final state particles. Additionally, the kinematic fit was required to converge in order to save the combo to the output TTree.

Further requirements of the plugin included keeping only events within the timing window $|t_{event} - t_{RF}| \leq 6.5\boldsymbol{\tau}$, where $\boldsymbol{\tau}$ is the beam period of 4.008 ns for the set of data analyzed and the RF time comes from the accelerator clock corresponding to the beam period. This wide range was used for accidental subtraction in the DSelector which is explained in a later paragraph.

For each candidate p, K^+, and K^-, a timing cut was made for each detector. The track vertex time was determined by correcting for the track flight time from its track vertex to each respective detector assuming the proper mass hypothesis. The time difference between this vertex time and the RF beam bunch provided an excellent determination of the particle identification (PID). Further insight was obtained by comparing this time difference as a function of particle momentum, which can be seen in Fig. 5.2 for the proton, Fig. 5.3 for

Table 5.1: Initial PID Δt cut summary

Candidate	Detector System	Cut [ns]
Proton	BCAL	$\pm$2.5
Proton	FCAL	$\pm$3.0
Proton	TOF	$\pm$2.5
K^+	BCAL	$\pm$2.5
K^+	FCAL	$\pm$2.5
K^+	TOF	$\pm$0.75
K^-	BCAL	$\pm$2.5
K^-	FCAL	$\pm$2.5
K^-	TOF	$\pm$0.75

the K^+, and Fig. 5.4 for the K^- candidates. The table 5.1 summarizes the timing cuts in the initial plugin.

A missing four-momentum was formed by Eq. 5.43

$$P_{miss} = P_i - P_f = (P_\gamma + P_p) - (P_{K^+} + P_{K^-} + P_{p'}), \tag{5.43}$$

where conservation of energy and momentum require $P_{miss} = (0, 0, 0, 0)$. However, this was not the case due to detector uncertainty in determining the particle four-momenta. Instead, it was required that this quantity be sufficiently close to zero. For the initial cuts, the missing mass squared of the combination was within -0.06 to 0.06 $(GeV/c^2)^2$ and can be seen in Fig. 5.5.

Fig. 5.6 shows the invariant mass of the two kaon candidates as a function of the kinematic fit confidence level. It shows a ϕ peak at 1.02 GeV as well as a wide peak at 1.2 GeV. This higher mass peak is the result of pions misidentified as kaons which happen to form a ρ meson. This effect was reduced by cutting on the confidence level of the kinematic fitter.

All of these requirements were used as initial cuts to reduce the amount of data needed to be analyzed. These cuts provided a way to immediately remove obvious background and allowed for further analysis to be performed on a more compact data set.

Within the DSelector, tighter cuts were made to fine-tune the signal to background ratio. Based on the Fig. 5.6, a cut on the kinematic fit confidence level of 10^{-4} removed a significant portion of misidentified ρ events while keeping the ϕ signal. A missing mass squared cut of

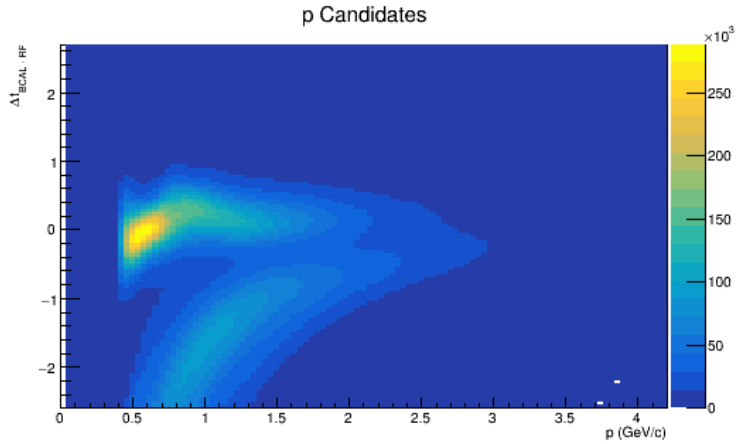

(a) Proton Δt in BCAL

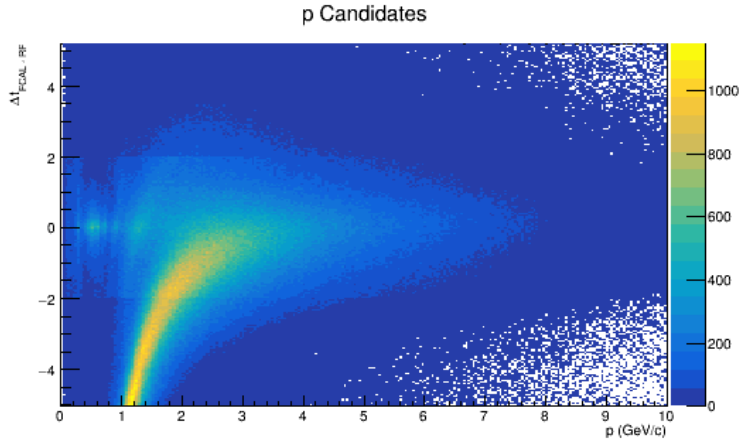

(b) Proton Δt in FCAL

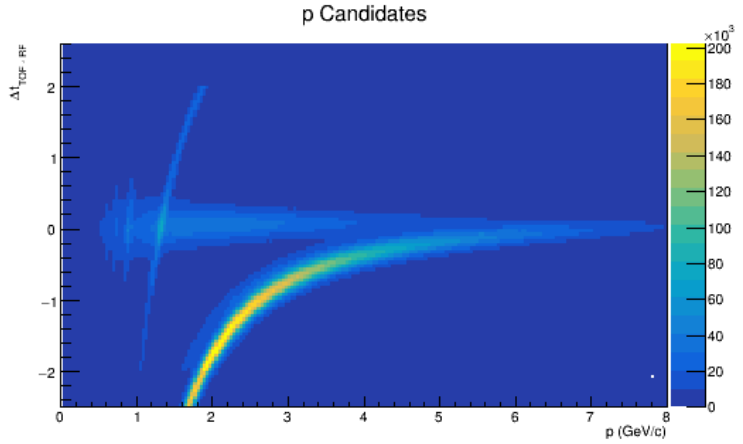

(c) Proton Δt in TOF

Figure 5.2: Proton Δt cuts in the BCAL, FCAL, and TOF. (a) In the BCAL, the cut keeps $t \leq |2.5|$, (b) in the FCAL, the cut keeps $t \leq |3.0|$, and (c) in the TOF, the cut keeps $t \leq |2.5|$. The stray curve at 1 GeV is caused by selecting the wrong RF bucket for the track.

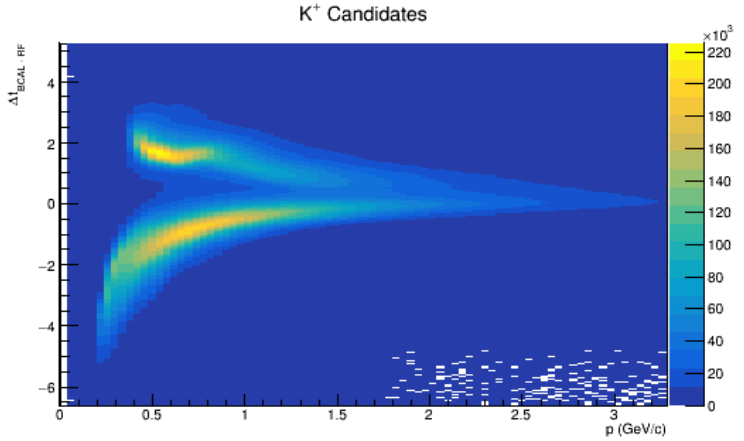

(a) K^+ Δt in BCAL

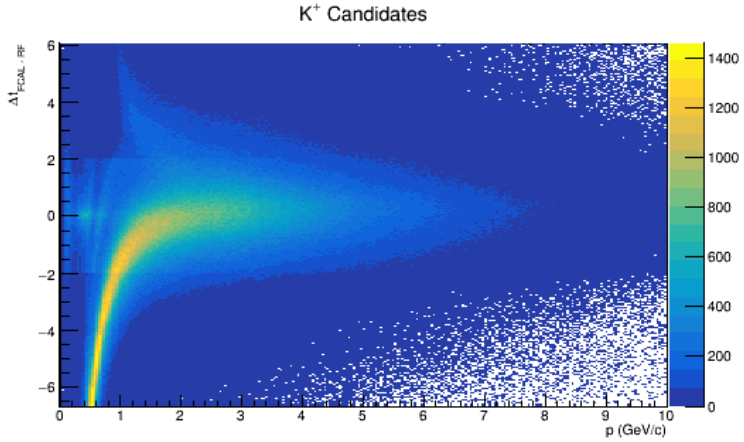

(b) K^+ Δt in FCAL

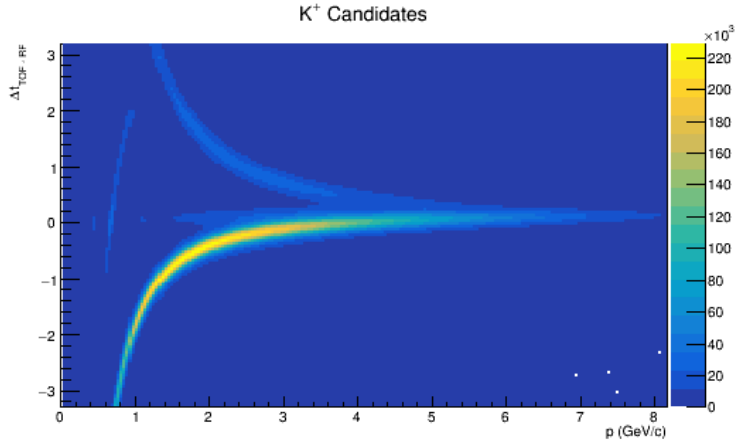

(c) K^+ Δt in TOF

Figure 5.3: K^+ Δt cuts in the BCAL, FCAL, and TOF. (a) In the BCAL, the cut keeps $t \leq |2.5|$, (b) in the FCAL, the cut keeps $t \leq |2.5|$, and (c) in the TOF, the cut keeps $t \leq |0.75|$.

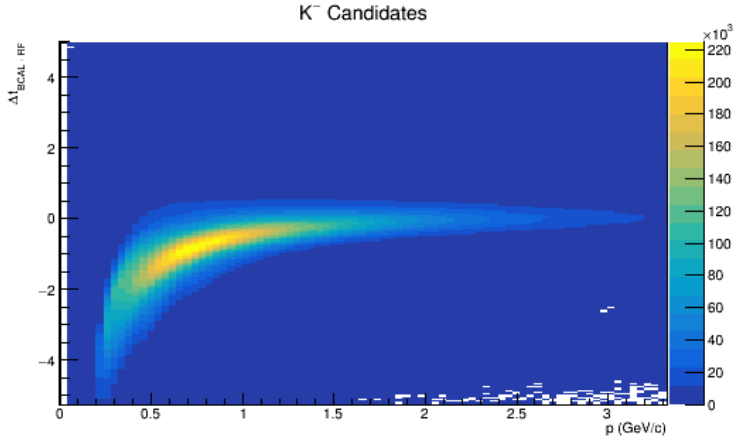

(a) K^- Δt in BCAL

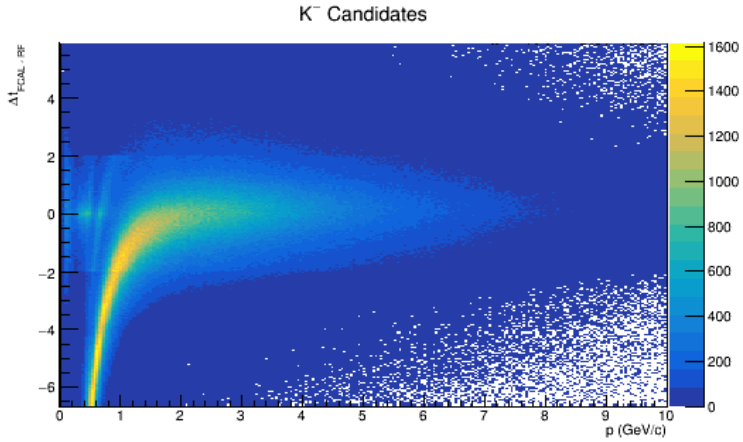

(b) K^- Δt in FCAL

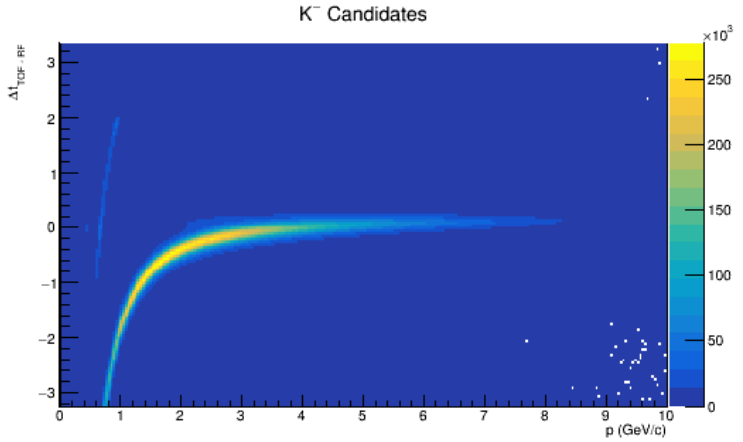

(c) K^- Δt in TOF

Figure 5.4: K^- Δt cuts in the BCAL, FCAL, and TOF. (a) In the BCAL, the cut keeps $t \leq |2.5|$, (b) in the FCAL, the cut keeps $t \leq |2.5|$, and (c) in the TOF, the cut keeps $t \leq |0.75|$.

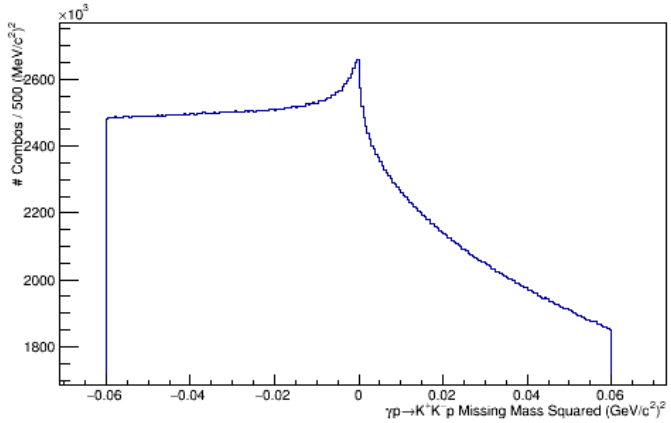

Figure 5.5: Initial missing mass squared cut from -0.06 to 0.06 $(GeV/c^2)^2$.

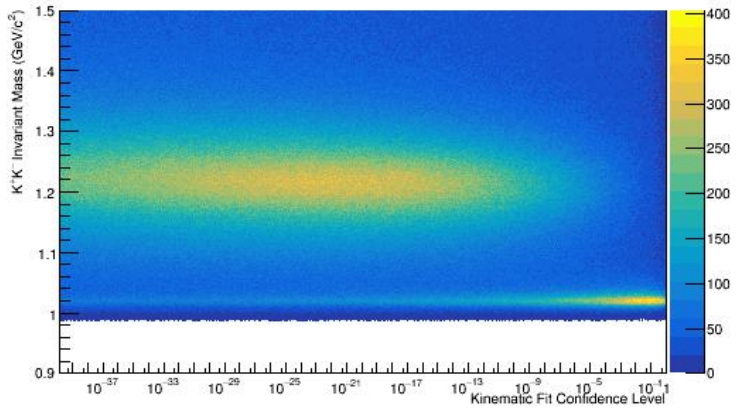

Figure 5.6: Invariant mass as a function of kinematic fit confidence level. The ρ background diminishes with higher confidence level.

Table 5.2: PID Δt cut summary from the DSelector

Candidate	Detector System	Cut [ns]
Proton	BCAL	$\pm$1.0
Proton	FCAL	$\pm$2.0
Proton	TOF	$\pm$1.0
K^+	BCAL	$\pm$0.5
K^+	FCAL	$\pm$1.0
K^+	TOF	$\pm$0.4
K^-	BCAL	$\pm$0.5
K^-	FCAL	$\pm$1.0
K^-	TOF	$\pm$0.4

-0.01 to 0.01 $(GeV/c^2)^2$ was included. Similarly, the Δt cuts on the particle identification (PID) used by the DSelector can be seen in Figs. 5.2-5.4 and are summarized in table 5.2. Additionally, cuts were made to restrict the tracks to those which originated from the target volume. This required keeping tracks that originated between 51 to 76 cm and were radially within 1 cm of the beam axis. These cuts avoided the target walls and windows.

It was expected that the recoil proton was detected by the CDC and so a cut on the energy deposition per unit length, dE/dx, was made. The energy deposition as a function of momentum can be seen in Fig. 5.7 before and after the cut. According to the Bethe-Bloch equation, $dE/dx \propto M/\beta^2$, which implies that lower momentum protons deposit more energy per unit length than light particles at the same momentum. The horizontal band below a dE/dx of 2 keV/cm corresponds to particles other than protons. An effective way to differentiate between the protons and non-protons is to use an exponential cut of the form (Eq. 5.44)

$$\frac{dE}{dx} = 1.0 + e^{2.0p+2.0} \tag{5.44}$$

where the parameters were determined empirically.

The final preparations of the output TTrees for analysis of the SDMEs required a cut on the photon beam energy, $8.4 < \mathrm{E}_\gamma < 9.0$ GeV, the invariant mass, $1.005 < m_\phi < 1.040$ GeV/c^2, and a restriction on the Mandelstam t variable, $0.06 < |t| < 0.80$ $(GeV/c^2)^2$. The cut on $|t|$ was made to match the previous experiment in Ref. [38] so that a direct comparison

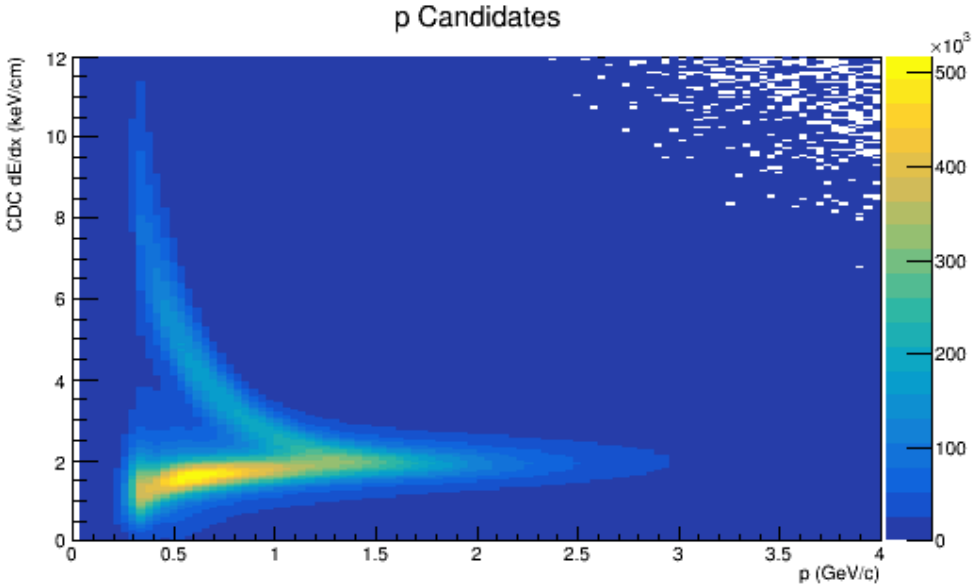

(a) dE/dx in the CDC before cuts

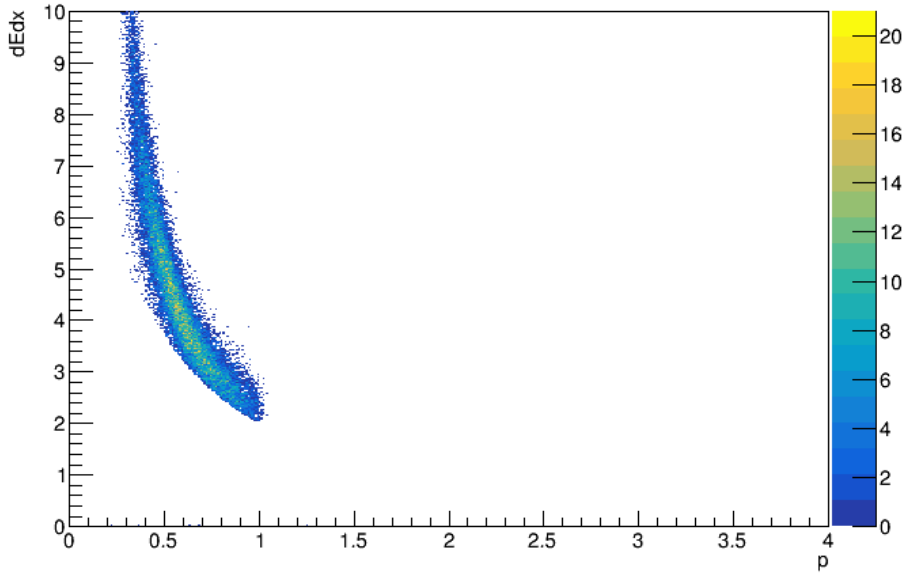

(b) dE/dx in the CDC after cuts

Figure 5.7: (a) Proton dE/dx in the CDC before any cuts were made. (b) A cut was made to reject the events beneath the curve formed by equation 5.44.

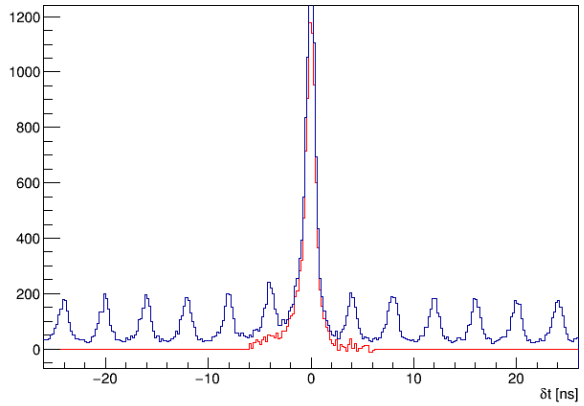

Figure 5.8: Accidental subtraction in data. The red line shows the signal after accidental subtraction. There is a non-zero amount of signal in the peaks neighboring the central peak.

could be made. The data were also binned in 0.24 $(GeV/c^2)^2$ increments of $|t|$ from 0.06 to 1.02 to examine how the SDMEs changed as a function of $|t|$.

In addition to these cuts, accidental subtraction was also performed in the DSelector code. Any event with a $|\Delta t| = |t_{event} - t_{RF}| < 1.5\boldsymbol{\tau}$ was given a weight of 1.0. All events in the range $1.5\boldsymbol{\tau} < |\Delta t| < 6.5\boldsymbol{\tau}$ received a weight of -0.3, where the weight is the ratio of signal and background widths. These weights were saved in the output TTree file.

A simple sideband approach was also implemented in the analysis. Because the ϕ is near threshold, a region of invariant mass from 1.06 to 1.20 was considered for a sideband region. The background was modeled with a first order polynomial which was used to estimate the background within the signal region.

5.4 Simulation/Monte Carlo

One way to test the cuts and analysis was to use Monte Carlo. This process involved generating events based on known physics and simulating the final state interactions with the detector. The remaining steps of hit reconstruction and analysis were the same as for experimental data.

Table 5.3: AmpTools classes

Class	Description
DataReader	read data and return a Kinematics object (list of 4-vectors)
DataWriter	input a Kinematics object and write data
Amplitude	take kinematics (4-vectors) as input and return a complex number
PlotGenerator	make plots from results

A convenient tool for this process is AmpTools, an amplitude analysis framework created at Indiana University [39]. This was designed to be used for amplitude analyses but is also successful in generating simulated data based on provided physics amplitudes. It consists of C++ classes, described in table 5.3, which are used in creating applications to perform amplitude analyses.

The physics problem in AmpTools is the expansion of an intensity in terms of amplitudes,

$$I(\Omega) = \sum_{\alpha} |\sum_{\beta} V_{\alpha\beta} A_{\alpha\beta}(\Omega)|^2, \tag{5.45}$$

where $I(\Omega)$ is the kinematics from the 4-vectors, the sum over α is an incoherent sum, the sum over β is a coherent sum, $V_{\alpha\beta}$ are the production amplitudes (complex fit parameters), and $A_{\alpha\beta}(\Omega)$ are the decay amplitudes from theory. The intensity is related to experimental observables through

$$\int I(\Omega)\eta(\Omega)d\Omega = N_{predicted}, \tag{5.46}$$

where $\eta(\Omega)$ is the detector acceptance. The computer science problem is to perform a maximum likelihood fit which is discussed in detail in section 5.6.

For the purposes of simulation, a model of the ϕ photoproduction intensity can be formed as

$$I(\Omega) = A_{norm} \cdot PS \cdot BW \cdot W(cos\theta, \phi, \Phi) \cdot e^{At}, \tag{5.47}$$

where A_{norm} is a normalization factor, PS is a phase-space factor, BW is a Breit-Wigner, $W(cos\theta, \phi, \Phi)$ is the angular dependence described in section 5.2, and e^{At} is the t-dependence. AmpTools classes have been made to handle all of these factors which we either modify or provide input values for in order to create our simulated events.

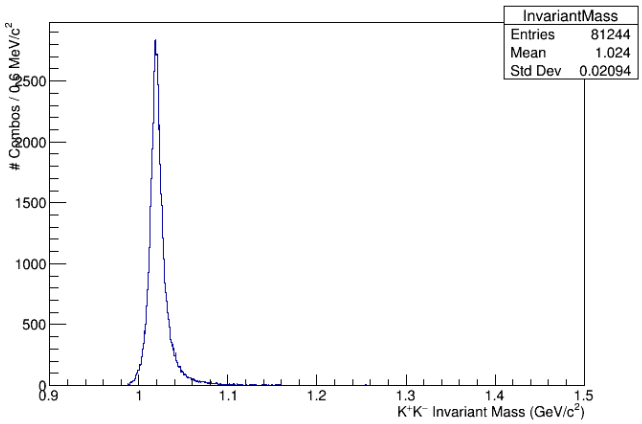

Figure 5.9: Simulated ϕ invariant mass with no background.

The Breit-Wigner factor is a class in AmpTools that requires the input of a mass in GeV, a width in GeV, the orbital angular momentum l, and the decay products of the resonance. For this simulation, a mass of 1.02 GeV with a width of 4 MeV, $l = 0$, and a K^+ and K^- for the daughters, was used.

For the W angular distribution, AmpTools provides a class that reads in specified spin-density matrix elements. This simulation assumed s-channel helicity conservation (SCHC) from linearly polarized photons so the input values were all 0 except for ρ^1_{1-1} and $\mathrm{Im}\rho^2_{1-1}$ which were set to 0.5 and -0.5, respectively.

With these inputs set, 1 million events were generated and distributed over the energy range 7.5 to 9.5 GeV. These 4-vectors were then passed through a modeled GlueX spectrometer based on GEANT3 called hdgeant [1]. This passed each generated particle in each event through the various detectors to simulate their response. In addition, the results were then smeared to model the detector resolutions and efficiencies in a program called mcsmear. The final product was a set of data that looks similar to the experimental data.

At this point, the simulated data was then reconstructed and analyzed in the same way as real data. The invariant mass spectrum can be seen in Fig. 5.9. It can be seen that the generated ϕ events are clean and do not contain any background. This distribution was fit

[1]GlueX has recently upgraded to GEANT4. This analysis will be run again using the new software and will be compared with the GEANT3 results.

using a Breit-Wigner function of the form (Eq. 5.48)

$$BW(x, x_0, \gamma) = \frac{A_0}{2\pi} \frac{\gamma}{(x - x_0)^2 + \gamma^2/4} \tag{5.48}$$

where A_0, x_0, and γ are the fit parameters. A is the overall scale factor, x_0 corresponds to the central mass of the ϕ, and γ represents the width. The resulting fit mass was found to be 1.020 $\pm$ 0.001 GeV with a width of 8.23 $\pm$ 0.73 MeV.

The angular distributions can be seen in Figs. 5.10a - 5.10b. The polar angle was expected to follow a $\sin^2\theta$ distribution while the azimuthal angle was expected to follow Eq. 5.49

$$Y \propto 1 \pm P_\gamma A \cos(2\Psi - 2\Psi_0) \tag{5.49}$$

where the sign depends on the orientation of the polarization vector, P_γ is the polarization, and A is the analyzing power. In this case, PARA corresponds to a positive sign. The quantity PA was found to be 0.43 $\pm$ 0.01.

The t-distribution can be seen in Fig. 5.11. It was expected to follow an exponential distribution e^{bt}, where b is called the t-slope. For this distribution, the t-slope was determined to be -5.74 $\pm$ 0.03 $(GeV/c^2)^{-1}$.

A similar "flat" simulation was created which generated only ϕ mesons with unweighted phase space angular distributions. This flat simulation was used in AmpTools to determine the acceptance.

5.5 Data

As explained in section 5.1, the data set analyzed came from the spring 2016 run period. Linearly polarized photons were essential in extracting the SDMEs and this analysis used only the PARA orientation. The direction of polarization did not affect the analysis, however, it can illuminate acceptance and other detector issues if the results do not agree.

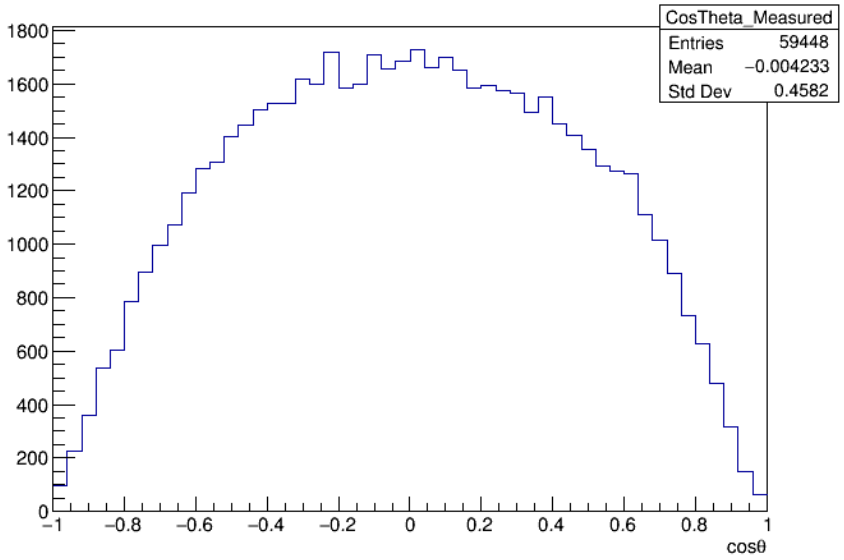

(a) Simulated $\cos(\theta_{helicity})$ distribution

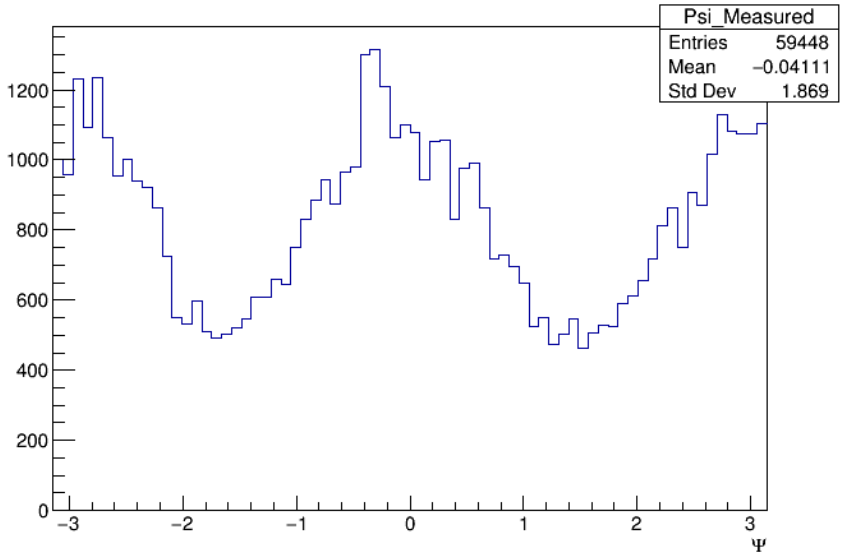

(b) Simulated $\Psi_{helicity}$ distribution

Figure 5.10: The (a) polar and (b) azimuthal angular distributions of the simulated data in the helicity frame. The sinusoidal relationship in (b) is related to the linear polarization of the photon.

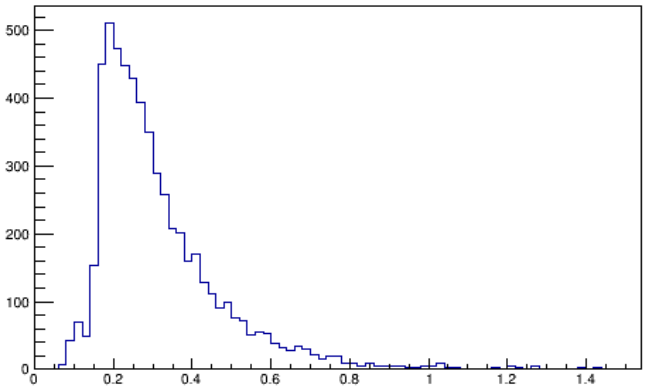

Figure 5.11: Simulated t-distribution with $|-t|$ $(GeV/c^2)^2$ on the x-axis and yield along the y-axis. This was generated using a t-slope of -6.

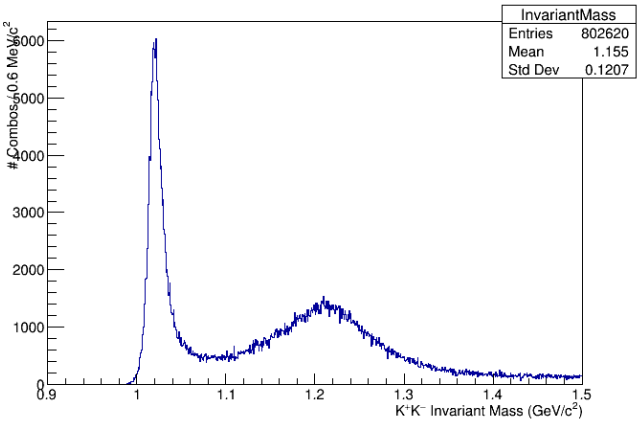

Figure 5.12: Invariant mass of the ϕ. The peak near 1.2 GeV/c^2 comes from ρ background of two pions being misidentified as kaons.

Fig. 5.12 shows the invariant mass distribution after a confidence level cut of 10^{-4} on the kinematic fit. A prominent peak at 1.2 GeV remained due to pions misidentified as kaons. Increasing the cut reduced both the ϕ and shifted ρ peaks. This distribution was fit using a Breit-Wigner function of the form (Eq. 5.48) and was found to have a mass of 1.020 GeV and a width of 8.33 MeV.

The angular distributions in Figs. 5.13a and 5.13b show the expected behavior of the ϕ. Because the ϕ has an angular momentum $l = 1$, the polar angle is expected to follow a $\sin^2\theta$ distribution, while the azimuthal angle is expected to follow Eq. 5.49. The quantity $P\Sigma$ was found to be 0.43.

The t-distribution can be seen in Fig. 5.14. It is expected to follow an exponential distribution e^{bt}, where b is called the t-slope. The t-distribution extracted from the data show a t-slope of -4.37 $\pm$ 0.18 GeV^{-2}. This value matches that of Ballam et al, who measured a t-slope of -4.6 $\pm$ 0.7 GeV^{-2}.

Both the data and simulation have had the appropriate cuts applied at this stage of the analysis and are now prepared for a maximum likelihood fit using AmpTools which is discussed in the next section.

5.6 Maximum Likelihood Fitting

The background was reduced from the ϕ sample using the cuts described in section 5.3 and the SDMEs were extracted. This has been performed using the AmpTools framework which requires three files containing simulated MC events:

1. A file containing the correct physics signal after event selection (data or MC)
2. A file without the physics signal being studied
3. The result of passing 2 through the same selection as 1.

These files contain only the 4-vectors for each of the particles in the reaction specified. The last two files were from the flat simulation and were used to determine the detector accep-

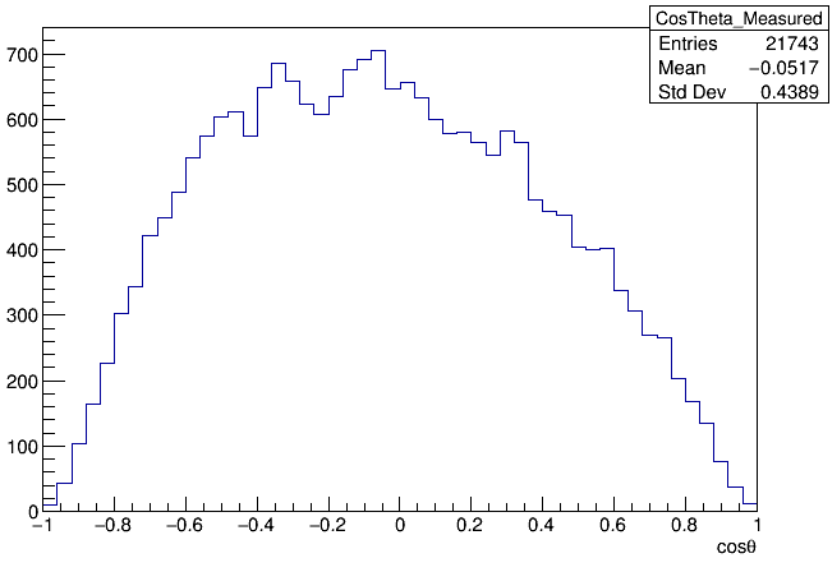

(a) Cos($\theta_{helicity}$) distribution

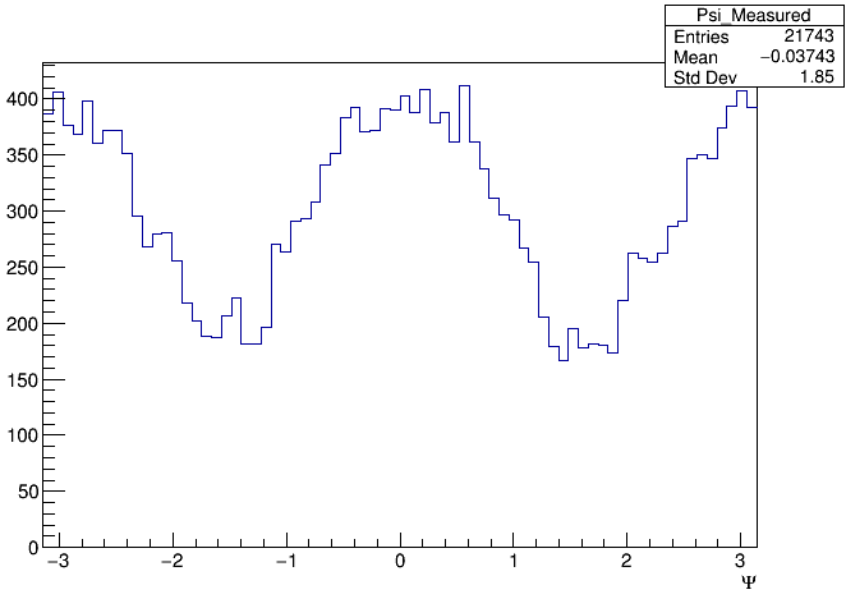

(b) $\Psi_{helicity}$ distribution

Figure 5.13: Angular distributions of ϕ meson in the helicity frame using spring 2016 data.

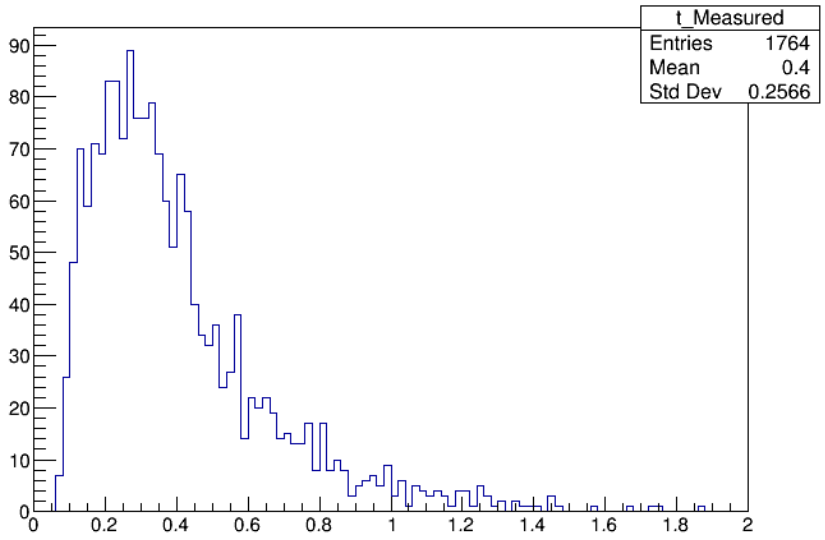

Figure 5.14: t-distribution for data run 11366

tance. AmpTools uses these files and performs an unbinned extended maximum likelihood fit, which is described in this section.

The "likelihood" is the combined probability for detecting all events observed and finding the detected number of events assuming a random arrival. This is then the product of individual event probabilities and the Poisson probability density function

$$\mathcal{L} = \frac{e^{-\mu}\mu^N}{N!}\prod_i^N P(\vec{x_i},\vec{\theta}) \tag{5.50}$$

where N is the observed number of events, μ is the expected number of events, and $P(\vec{x_i},\vec{\theta})$ is the probability density function of measuring kinematic variables x_i with parameters $\vec{\theta}$. The expected number of events can be written as the intensity weighted by the detector acceptance η and therefore be expressed as

$$\mu = \int \eta(\vec{x})I(\vec{x},\vec{\theta})d\vec{x} = \frac{\nu}{N_{gen}}\sum_i^{N_{gen}} \eta(\vec{x_i})I(\vec{x_i},\vec{\theta}) = \frac{1}{N_{gen}}\sum_i^{N_{acc}} I(\vec{x_i},\vec{\theta}), \tag{5.51}$$

where ν is the volume of phase space but since it adds a constant term in $\mathcal{L}$ it can be ignored. The simulated acceptance $\eta(\vec{x_i})$ is approximated by the Monte-Carlo method and has the value of either 1 or 0 depending on whether it was detected or not, respectively. Therefore,

the summation is over the accepted events, and N_{gen} is used as a normalization factor. The probability density function can now be written as

$$P(\vec{x_i};\vec{\theta}) = \frac{I(\vec{x_i};\vec{\theta})}{\mu} \tag{5.52}$$

The intensity can be expanded as a sum of interfering amplitudes

$$I(\vec{x_i};\vec{\theta}) = \Big|\sum_{\alpha}^{n} V_\alpha A_\alpha(\vec{x_i};\vec{\theta})\Big|^2 = \sum_{\alpha,\beta}^{n} V_\alpha V_\beta^* A_\alpha(\vec{x_i};\vec{\theta}) A_\beta^*(\vec{x_i};\vec{\theta}) \tag{5.53}$$

where $V_{\alpha,\beta}$ are the coefficients of the amplitudes A. From a computational standpoint, it is important to note the amplitude's dependence on the parameters $\vec{\theta}$. If the amplitude depends on the parameters as well as the kinematics, the amplitude will need to be recomputed. However, if it only depends on the kinematics, it only needs to be computed once while the coefficient V varies.

The goal is to maximize the likelihood but, computationally, it is equivalent and easier to work with the logarithm which turns the product into a sum. This yields

$$\begin{aligned}
\ln\mathcal{L} &= \ln\left[\frac{e^{-\mu}}{N!}\prod_{i}^{N} I(\vec{x_i};\vec{\theta})\right] = -\ln(N!) - \mu + \sum_{i}^{N}\ln I(\vec{x_i};\vec{\theta}) \\
&= C - \frac{1}{N_{gen}}\sum_{i}^{N_{acc}}\sum_{\alpha,\beta}^{n} V_\alpha V_\beta^* A_\alpha(\vec{x_i};\vec{\theta}) A_\beta^*(\vec{x_i};\vec{\theta}) + \sum_{i}^{N}\ln\left[\sum_{\alpha,\beta}^{n} V_\alpha V_\beta^* A_\alpha(\vec{x_i};\vec{\theta}) A_\beta^*(\vec{x_i};\vec{\theta})\right] \\
&= C - \sum_{\alpha,\beta}^{n} V_\alpha V_\beta^*\left[\frac{1}{N_{gen}}\sum_{i}^{N_{acc}} A_\alpha(\vec{x_i};\vec{\theta}) A_\beta^*(\vec{x_i};\vec{\theta})\right] + \sum_{i}^{N}\ln\left[\sum_{\alpha,\beta}^{n} V_\alpha V_\beta^* A_\alpha(\vec{x_i};\vec{\theta}) A_\beta^*(\vec{x_i};\vec{\theta})\right],
\end{aligned} \tag{5.54}$$

where C is a constant that is ignored when minimizing the likelihood. If the amplitudes A do not depend on $\vec{\theta}$, the amplitude products can be precomputed

AmpTools uses ROOT's MINUIT class for minimization and error analysis, and once it completes, a value and statistical error are provided for each amplitude. Additionally, the error matrix and correlation coefficients are provided which are useful in determining the quality of the fit result.

AmpTools was used to analyze the simulation, data, and the data split into four bins of $|t|$. These results are discussed in the next section.

Table 5.4: Spin-density Matrix Elements. The data and simulation columns are the results of my analyses while the Ballam column contains the reported values from a previous experiment at 9.3 GeV [38]. The errors for data and simulation are statistical.

Quantity	Data	Simulation	Ballam
ρ^0_{00}	0.079 ± 0.002	0.003 ± 0.006	0.00 ± 0.07
$\mathrm{Re}\,\rho^0_{10}$	-0.001 ± 0.001	0.007 ± 0.006	-0.01 ± 0.06
ρ^0_{1-1}	0.148 ± 0.002	0.102 ± 0.006	-0.14 ± 0.09
ρ^1_{11}	-0.232 ± 0.005	0.061 ± 0.006	-0.18 ± 0.13
ρ^1_{00}	-0.063 ± 0.005	0.008 ± 0.006	0.08 ± 0.12
$\mathrm{Re}\,\rho^1_{10}$	-0.004 ± 0.004	-0.001 ± 0.006	-0.20 ± 0.11
ρ^1_{1-1}	0.282 ± 0.007	0.464 ± 0.006	0.44 ± 0.15
$\mathrm{Im}\,\rho^2_{10}$	-0.01 ± 0.005	0.001 ± 0.006	-0.14 ± 0.09
$\mathrm{Im}\,\rho^2_{1-1}$	-0.371 ± 0.007	-0.477 ± 0.006	-0.73 ± 0.17
P_σ	0.628 ± 0.015	0.920 ± 0.013	0.80 ± 0.32
Σ	0.083 ± 0.178	0.874 ± 0.020	0.72 ± 0.60

5.7 Results Discussion

The results of the AmpTools maximum likelihood fit can be found in Table 5.4 for the full range of $|t|$. Included in the table are the results from a bubble-chamber experiment [38] at SLAC using a 9.3 GeV beam. The SLAC experiment used Compton back-scattering to produce the polarized photon. The quantities listed are in the helicity frame. The errors shown for the data and simulation columns are statistical only. Fig. 5.15 shows the SDMEs as a function of $|t|$ from the data.

The SDMEs provide insight on the various helicity flip intensities and interferences at the $\gamma\phi$ vertex. The ρ^0_{00} element corresponds to the helicity amplitudes

$$\rho^0_{00} = \frac{1}{n} \sum_{\lambda_{N'},\lambda_N} |T_{0\lambda_{N'},1\lambda_N}|^2 \tag{5.55}$$

where $\lambda_{N'}$ and λ_N correspond to the initial and final state nucleon helicities and n is a normalization factor. This quantity measures the intensity of the helicity flip of 1 unit at the $\gamma\phi$ vertex. The data are near zero indicating minimal single helicity flip. As $|t|$ increases, the single-flip contributions become non-negligible.

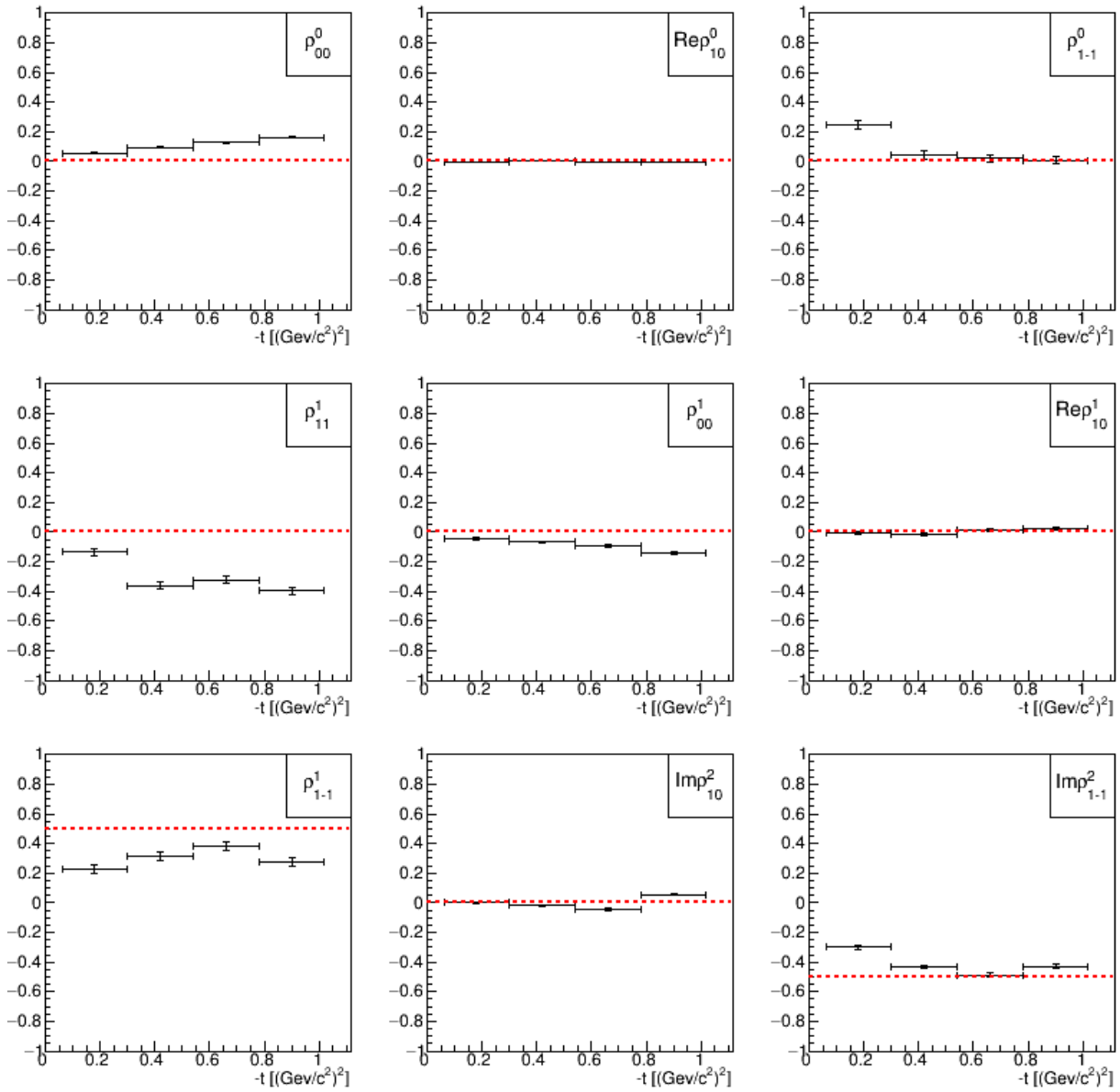

Figure 5.15: Spin-density matrix elements as a function of $|t|$. The dotted red line corresponds to the ideal case of s-channel helicity conservation.

The ρ^0_{1-1} element is a measure of the interference of non-flip and double-flip amplitudes and is defined as

$$\rho^0_{1-1} = \frac{1}{n} \mathrm{Re} \sum_{\lambda_{N'},\lambda_N} T_{1\lambda_{N'},1\lambda_N} T^*_{-1\lambda_{N'},1\lambda_N} \tag{5.56}$$

For $|t| > 0.3$, the interference is 0, however, the lowest bin shows a significant deviation from 0 which may indicate interference at low $|t|$.

The combination of $\mathrm{Re}\,\rho^0_{10} - \mathrm{Im}\,\rho^2_{10}$ measures the interference between non-flip and single-flip amplitudes,

$$\mathrm{Re}\,\rho^0_{10} - \mathrm{Im}\,\rho^2_{10} = \frac{1}{n} \mathrm{Re} \sum_{\lambda_{N'},\lambda_N} T_{1\lambda_{N'},1\lambda_N} T^*_{0\lambda_{N'},-1\lambda_N} \tag{5.57}$$

which is consistent with zero for all bins of $|t|$. Similar information can be obtained from $\mathrm{Re}\,\rho^0_{10}$ if the double-flip amplitudes are small,

$$\mathrm{Re}\,\rho^0_{10} = \frac{1}{2n} \mathrm{Re} \sum_{\lambda_{N'},\lambda_N} (T_{1\lambda_{N'},1\lambda_N} - T_{-1\lambda_{N'},1\lambda_N}) T^*_{0\lambda_{N'},1\lambda_N} \tag{5.58}$$

which are measured to be zero over all $|t|$.

Lastly, the combination,

$$\rho^1_{1-1} + \mathrm{Im}\,\rho^2_{1-1} = \frac{1}{n} \sum_{\lambda_{N'},\lambda_N} (|T^N_{1\lambda_{N'},-1\lambda_N}|^2 - |T^U_{1\lambda_{N'},-1\lambda_N}|^2) \tag{5.59}$$

where N and U correspond to natural and unnatural exchange, can be used to estimate the intensity of the helicity flip by two units at the vertex when either exchange dominates. For all $|t|$, this combination is approximately zero.

The parity asymmetry, P_σ (Eq. 5.40), is a measure of the naturality of the production mechanism and is expected to be 1 for a purely natural parity-exchange. Fig. 5.16 shows the parity asymmetry as a function of $|t|$. As can be seen with both the GlueX and the SLAC data, the asymmetry shows dominant natural parity exchange.

The beam asymmetry, Σ (Eq.5.41), is another asymmetry typically measured. The parallel and perpendicular subscripts are related to the angle between the photon polarization vector and the production plane, where parallel has an angle $\Phi = \pi/2$, while perpendicular corresponds to $\Phi = 0$ [40]. Fig. 5.17 shows how this asymmetry changes as a function of $|t|$.

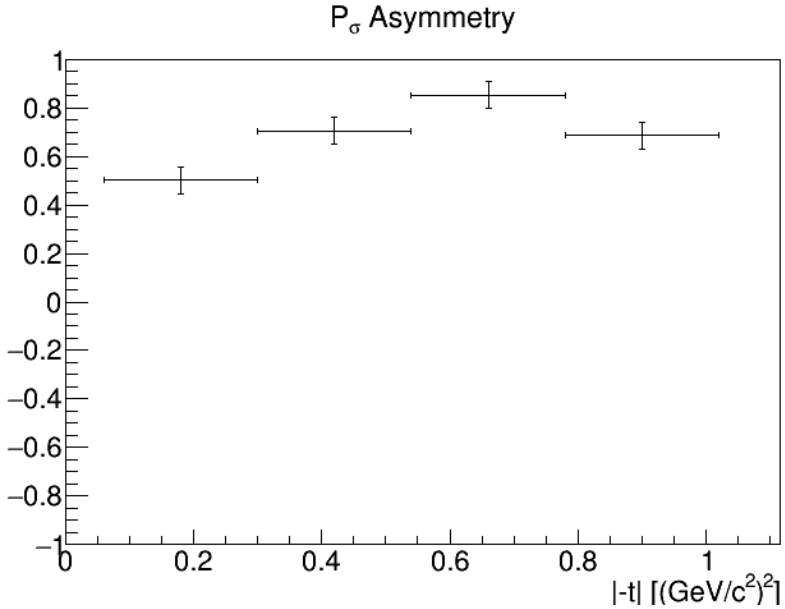

Figure 5.16: Parity asymmetry as a function of $|t|$. A value of 1 indicates a natural parity exchange while -1 indicates unnatural exchange. The data show a predominately natural exchange for the ϕ.

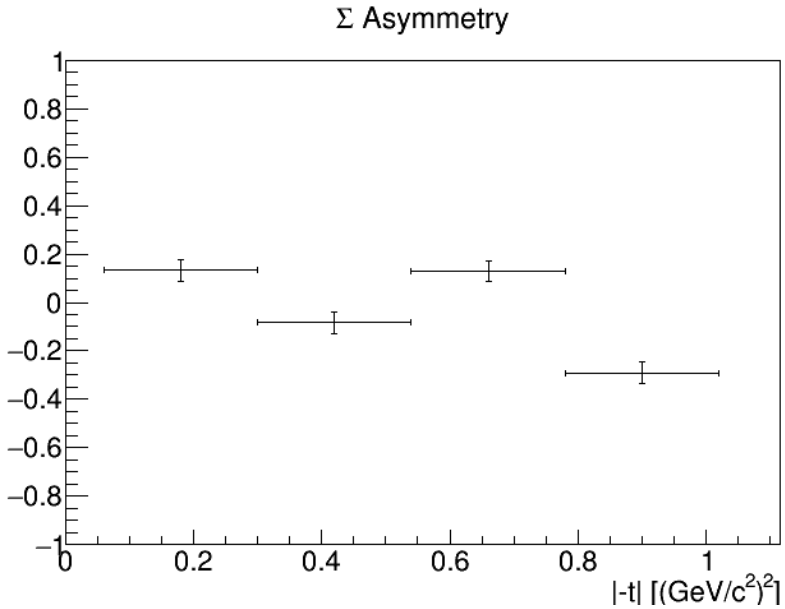

Figure 5.17: Beam asymmetry as a function of $|t|$. This indicates that there is approximately an equal ϕ production rate from photons polarized parallel and perpendicular to the production plane in the ϕ mass region.

In the GlueX data, this asymmetry is approximately zero for all $|t|$. The result from SLAC has a very large error on this parameter but they are consistent with the GlueX result.

As mentioned in section 5.2, for natural parity exchange in the t-channel, the value of 0.5 is expected for elements ρ^1_{1-1} and -Im ρ^2_{1-1}. It can be seen from the data that the ϕ is predominantly produced by natural parity exchange and is mostly s-channel helicity conserving. However, it is clear that other processes are contributing to these matrix elements which make this region of QCD more interesting.

The results above are the current state of the analysis, however, more work is intended for future publication. GlueX has only just begun and more detailed studies of the detector acceptance have yet to be performed. Improvements in the measurements and associated errors are expected and can be made by including an improved $sFit$ background estimation method as outlined in reference [41]. This method expands upon the technique used by groups such as LHCb. Further improvements will be made when the DIRC is installed in 2018 which will provide better π-K separation and reduce the amount of misidentified pions.

This analysis served as a high-level calibration for GlueX. The measurement of a well-known state, and observing quantities which have been precisely measured in the past, allowed the experimenters to understand the performance of the detector. By investigating the ϕ, GlueX measured the acceptance and sensitivity to $s\bar{s}$ states which is important for future exotic hybrid searches. Based on the results which have been presented here, it is clear that GlueX is able to measure the properties of the ϕ-meson with similar results to past experiments.

BIBLIOGRAPHY

[1] Claude Amsler and Frank E. Close. Evidence for a a scalar glueball. *Phys.Lett.*, B353:385–390, 1995.

[2] Claude Amsler and Frank E. Close. Is $f_\circ(1500)$ a scalar glueball? *Phys.Rev.*, D53:295–311, 1996.

[3] Frank E. Close and Andrew Kirk. Scalar glueball q anti-q mixing above 1-GeV and implications for lattice QCD. *Eur.Phys.J.*, C21:531–543, 2001.

[4] Colin J. Morningstar and Mike J. Peardon. Efficient glueball simulations on anisotropic lattices. *Phys.Rev.*, D56:4043–4061, 1997.

[5] G.S. Adams et al. Observation of a new J(PC) = 1-+ exotic state in the reaction $\pi^- p \to \pi^+\pi^-\pi^- p$ at 18-GeV/c. *Phys.Rev.Lett.*, 81:5760–5763, 1998.

[6] D. Alde et al. Evidence for a 1^{-+} Exotic Meson. *Phys.Lett.*, B205:397, 1988.

[7] Yu.D. Prokoshkin and S.A. Sadovsky. Analysis of D wave in $\pi^- p \to a_2(0)(1320)n$ reaction. *Phys.Atom.Nucl.*, 58:606–612, 1995.

[8] G.M. Beladidze et al. Study of $\pi^- n \to \eta\pi^- n$ and $\pi^- d \to \eta\prime\pi^- n$ reactions at 37-GeV/c. *Phys.Lett.*, B313:276–282, 1993.

[9] H. Aoyagi, S. Fukui, T. Hasegawa, N. Hayashi, N. Horikawa, et al. Study of the $\eta\pi^-$ system in the $\pi^- p$ reaction at 6.3-GeV/c. *Phys.Lett.*, B314:246–254, 1993.

[10] GlueX Collaboration. *Hall D GlueX Technical Design Report*, March 2014. Technical note GlueX-doc-2442 available at `http://argus.phys.uregina.ca/gluex/DocDB/0024/002442/001/tdr.pdf`.

[11] Curtis Meyer et al. The gluex experiment in hall-d. A proposal to the 36th Jefferson Lab Program Advisory Committee, GlueX-doc 1545-v7, 2010.

[12] Volker Crede et al. An initial study of mesons and baryons containing strange quarks with gluex. A proposal to the 40th Jefferson Lab Program Advisory Committee, GlueX-doc 2198-v10, 2013.

[13] John Smedley et al. Laser patterning of diamond. part i. characterization of surface morphology. *Journal of Applied Physics*, 105, 2009.

[14] Alexander Somov et al. Pair spectrometer hodoscope for hall d at jefferson lab. *Nuclear Instruments and Methods in Physics Research Section A*, 795:376–380, 2015.

[15] M. Dugger et al. Design and construction of a high-energy photon polarimeter. *Nuclear Instruments and Methods in Physics Research Section A*, 2017.

[16] Brianna Thorpe. A triplet polarimeter for use in the jefferson lab gluex experiment. Poster for APS 2015 meeting, 2015.

[17] Beni Zihlmann. *TOF detector description for CDR*, March 2008. Technical note available at `http://argus.phys.uregina.ca/gluex/DocDB/0009/000994/004/TOF_cdr.pdf`.

[18] Y. Van Haarlem et al. The gluex central drift chamber: Design and performance. *Nuclear Instruments and Methods in Physics Research Section A*, 622:142–156, 2010.

[19] L. Pentchev et al. Studies with cathode drift chambers for the gluex experiment at jefferson lab. *Nuclear Instruments and Methods in Physics Research Section A*, 845:281–284, 2017.

[20] GlueX Collaboration. *Hall D GlueX Technical Construction Report*, May 2015. Technical note GlueX-doc-2511-v4 available at `http://argus.phys.uregina.ca/gluex/DocDB/0025/002511/004/tcr.pdf`.

[21] B. D. Leverington et al. Performance of the prototype module of the gluex electromagnetic barrel calorimeter. *Nuclear Instruments and Methods in Physics Research Section A*, 596:327–337, 2008.

[22] K. Moriya et al. A measurement of the energy and timing resolution of the gluex forward calorimeter using an electron beam. *Nuclear Instruments and Methods in Physics Research Section A*, 726:60–66, 2013.

[23] Curtis Meyer. Performance of the gluex detector systems. Technical note GlueX-doc-2775-v10, 2015.

[24] The GlueX Collaboration. Summary of hall d subsystems. Technical note GlueX-doc-2376-v7, 2013.

[25] S. Denisov et al. Characteristics of the tof counters for gluex experiment. *Nuclear Instruments and Methods in Physics Research Section A*, 494:495–499, 2002.

[26] F. Barbosa et al. The gluex dirc detector. *Nuclear Instruments and Methods in Physics Research Section A*, 2017.

[27] Igor Senderovich. A polarized high-energy photon beam for production of exotic mesons. `http://zeus.phys.uconn.edu/wiki/images/Senderovichthesis.pdf`, 2012. A Dis-

sertation Submitted in Partial Fullfilment of the Requirements for the Degree of Doctor of Philosophy at the University of Connecticut.

[28] George J. Lolos Vitaly D. Kovaltchouk, Zisis Papandreou and Keith Wolbaum. *Readout system for a barrel calorimeter (GlueX project)*, 2003. GlueX doc no 69-v1 at http://argus.phys.uregina.ca/gluex/DocDB/0000/000069/001/SiPM-Report.pdf.

[29] H. K. Gummel and H. C. Poon. An integral charge control model of bipolar transistors. *Bell Syst. Tech. J.*, 49:827–852, 1970.

[30] William R. Leo. *Techniques for Nuclear and Particle Physics Experiments: A How-to Approach*, chapter Timing Methods and Systems, pages 325–326. Springer-Verlag, 1994.

[31] E.S. Smith. *Low-level calibration constants for BCAL*, December 2014. Technical note GlueX-doc-2618-v10, available at `http://argus.phys.uregina.ca/gluex/DocDB/0026/002618/010/bcal_constants.pdf`.

[32] P. G. O. Freund. Photoproduction of vector mesons as virtual vector meson-proton scattering. *Nuovo Cimento A*, 48:541–544, 1967.

[33] K. Schilling. On the Analysis of Vector-meson Production by Polarized Photons. *Nuc. Phys.*, B15:397–412, 1970.

[34] M. Jacob and G. C. Wick. On the General Theory of Collisions For Particles With Spin. *Ann. of Phys.*, 54:404, 1959.

[35] K. Gottfried and J. D. Jackson. On the Connection Between Production Mechanism and Decay of Resonances at High Energies. *Nuovo Cimento A*, 33:309–330, 1964.

[36] Paul Mattione. `https://halldweb.jlab.org/wiki/index.php/GlueX_Analysis_Software`.

[37] Paul Mattione. `https://halldweb.jlab.org/wiki/index.php/DSelector`.

[38] Joseph Ballam, G.B. Chadwick, Y. Eisenberg, E. Kogan, K.C. Moffeit, et al. Vector Meson Production by Polarized Photons at 2.8-GeV, 4.7-GeV, and 9.3-GeV. *Phys.Rev.*, D7:3150, 1973.

[39] Amptools. `https://sourceforge.net/projects/amptools`.

[40] Criegee. L et al. Rho production with polarized photons. *Phys. Lett.*, 28B:282–286, 1968.

[41] Richard T. Jones. sfit improved: Maximum likelihood fitting of unbinned data with weights. GlueX-doc 3182, 2016.